KU Leuven
Biomedical Sciences Group
Faculty of Medicine
Department of Imaging and Pathology

**KU LEUVEN**

DOCTORAL SCHOOL
BIOMEDICAL SCIENCES

# RIGID MOTION CORRECTION
# FOR HEAD CT IMAGING

Tao SUN

February 2018

# Acknowledgement

The author would like to acknowledge the following individuals who not only contributed to this thesis, but also helped me during my PhD.

I would like to first thank my promoter, Prof. Johan Nuyts. It is a great pleasure to work with him ever since the start of my PhD. He is always there to help, no matter when I got stuck with my project or when I seek for suggestions even on minor things. He has so much patience for his student and the willingness to share his insight at any time. His passion on research truly inspires me.

I am also very grateful to Prof. Roger Fulton from University of Sydney and Prof. Rolf Clackdoyle from University of Grénoble. Roger has been working together with Johan long before I came to Leuven. As soon as I started my PhD, we worked together on motion correction projects. I fully enjoy to work with him. He is more like a co-promoter to me rather than a collaborator. I worked together with Rolf on the very first project of my PhD. It is always great to have a mathematician like him, who always has different perspectives on seeing the problems. His is a rigorous researcher and I definitely learned many things from him.

I would like to thank all my jury members: Prof. Paul Suetens and Prof. Dirk Vandermeulen from ESAT, KU Leuven, Prof. Marc Kachelrieß from German Cancer Research Center (DKFZ) and Dr. Karl Stierstorfer from Siemens Healthcare. Thank you for following my work. Your criticism and feedback are extremely valuable. Special thanks to Dr. Stierstorfer for his interests in my PhD project. Whenever we need any information about the scanners, he is always willing to share that.

This thesis involves scans performed on several CT scanners in multiple institutions. For that, I would like to thank Dr. Ruben Pauwels and Prof. Reinhilde Jacobs from Oral and Maxillo-facial Surgery department in UZ Leuven; Walter Coudyzer from Radiology department in UZ Leuven; Krystal Moore from Nuclear Medicine department in Westmead Hospital in Sydney; Kwinten Porters and Jef van Loock from Nuclear Medicine department in UZ Leuven.

I would like to express my special thanks to Prof. Michel Defrise and Prof. Frédéric Noo. It was a pleasure to talk to you in many occasions. As experts in tomographic reconstruction, you are always willing to share the knowledge and the experience as scientific researchers. Your words are extremely helpful for a PhD student who just started his career.

I want to thank all my colleges: Matthew, Anna, Georg, Ahmad, Esmaeel, Masoud, Kathleen, Koen and others in the Medical Imaging Research Center. Especially for Matthew, he helped me with many things since I joined the group. Also many thanks to Francine from Nuclear Medicine department in UZ Leuven and Peter form Imaging and Pathology department in KU Leuven, for your assistance in the administrative works.

I thank all my friends I knew in Leuven. It was fun to spend time with you. At last I want to thank my parents for the understanding and support for my pursuing on a 4-year PhD abroad.

# Abstract

## Rigid motion correction for head CT imaging

The invention of X-ray computed tomography (CT) is considered as an important event in clinical medicine. CT provides an unprecedented way to visualize the internal human anatomy non-invasively. The reconstructed three-dimensional (3D) image from a scan facilitates many clinical applications, including diagnosis, treatment planning and surgery guidance, etc. In terms of design, current medical CT scanners can be categorized into two types: clinical multi-row CT and cone-beam CT, each has its own specific applications. As related hardware and software technologies are advancing, CT imaging is expected to continue playing an important role in clinical medicine.

Reconstruction is the process of recovering the 3D attenuation distribution of the scanned object from measured data. In order to ensure artifact-free reconstruction, the measured data must provide sufficient information. This associated condition is called data-sufficiency condition in CT imaging. The development of a new reconstruction algorithm for a specific CT geometry often involves such condition. There are two classes of reconstruction algorithms, analytical reconstruction algorithms and iterative reconstruction algorithms. An analytical algorithm applies an inverse acquisition model to the measured data, based on the derived mathematical relationship between measured data and scanned object. Filtered back projection (FBP) algorithm is an example of the analytical reconstruction algorithms and its variations are implemented in many commercial scanners. One advantage of FBP is that it is simple to be implemented and robust in many applications. However, when a scan is far away from the ideal condition (e.g. with large cone angle, low dose, metal implants, etc.), FBP-type algorithms may introduce artifacts into the reconstructed image, which may result in an image quality which is not suitable for further clinical applications.

Another type of reconstruction algorithms are the iterative reconstruction algorithms, which have been receiving lots of attention in research and clinical fields in recent years. In an iterative algorithm, computed projections are generated by applying a forward acquisition model on the current image estimate. When reconstructing an image, instead of applying a single step inversion like in a FBP-type algorithm, an iterative algorithm tries to approach the true representation of the object by imposing the data-consistency between the computed projections and measured data in a numerical way. By doing so, the image

update is improved at every iteration. The forward acquisition model used in the algorithm is better than an analytical inverse acquisition model, in terms of the ability to model the physical processes (noise, scattering, motion etc.) during a scan. On the other hand, iterative reconstruction often involves repetitive forward and backward projection operations. Nowadays the size of the CT data are huge due to the requirements of the large field-of-view (FOV) and the high resolution of a reconstructed image. Significant computational power is often needed when using an iterative algorithm to reconstruct a clinical CT image. As a result, acceleration of iterative reconstruction is of great interest to reduce the waiting time of radiologists and physicians.

A normal reconstruction process assumes that the scan conditions are ideal. However this often cannot be guaranteed in a real scan, which is subject to various perturbations. Incorrect handling of the deviation between the ideal and real condition often results in artifacts in a reconstructed image. A common cause of such a deviation in CT head imaging is patient motion. Many efforts have been made to prevent patient head movement during a CT-scan. For example, current state-of-art scanners can rotate very fast (down to 250 ms/rotation), and the fast image acquisition "freezes" most of the head movement. Also, many constraint devices, e.g. head supports, are used to prevent the patient from moving. Nevertheless, artifacts or resolution loss are still observed in many clinical images, especially in those non-collaborative patients (e.g. with mental diseases or children). Sometimes a repeat scan is required to obtain an artifact-free image, which inevitably increases the radiation dose to patients.

Motion correction is of general interest in CT imaging. Motion correction methods can be categorized into two groups. The first group requires the motion information, and consists of motion acquisition and motion compensation processes. Specifically, motion acquisition derives the motion information from reference images, surrogate signals or from the data themselves. Motion compensation compensates the motion during a reconstruction process. The second group is based on image-processing techniques, and corrects the motion without prior knowledge of the motion. Based on what prior information is available, one can choose the appropriate approach to perform the motion correction. For example, Kim et al. (2015b) acquired the rigid head motion during a scan using optical tracking techniques. The acquired motion then was compensated during an iterative reconstruction process.

In this thesis, we proposed an approach to reduce the rigid motion artifacts in CT scans without the usage of tracking. We focus on the helical head CT scans, where the movement of the head can be modelled as rigid motion. The proposed approach only requires the measured data as the available information. Since the acquisition time of a single view is extremely short, the motion in a single view is negligible compared with the resolution of the CT. Because of that we assume the position of the scanned object in one view can be represented with one single pose. This indicates that the poses of the object may be different

for each projection view. Consequently, a rigid transformation representing the relative pose for each view can be estimated. With this intermediate estimated motion, a motion-compensated reconstruction can be performed. The motion and reconstructed image can be updated alternately within a multi-resolution scheme, until an optimal motion estimate is found. The final compensation can be performed in a fine-resolution reconstruction process with acceleration. The proposed approach has been validated in various studies and the image quality was improved substantially compared with the uncorrected ones. The proposed approach was also extended to the rigid motion correction for dental cone-beam CT scans. One important difference between a dental cone-beam CT scan and a helical CT scan is that a cone-beam scan often has limited transaxial FOV. We have modified the proposed method according to this difference. The new method was validated in both simulations and a phantom study. We also pointed out that the approach would fail in cases where non-rigid motion is present.

Sometimes patient movement can cause another problem in a CT-scan, which is data-insufficiency. Assuming the existence of ideal and continuous data, satisfying the data-sufficiency conditions would imply that the trajectory of the source (and the detector) generates data that are sufficient for exact reconstruction. Or in other words, the data ensures that the reconstruction problem has a unique solution and its estimate is stable. Data-sufficiency has mostly been studied for untruncated projections. However the results do not apply for a helical CT scan as it is always truncated in the axial direction (so-called "long object problem"). It has been shown that under certain conditions which are usually satisfied in clinical scans, the data produced with a helical CT trajectory are sufficient (Danielsson et al. 1997; Tam et al. 1998). However, in the presence of motion, an effective trajectory is created with respect to the patient. This new effective trajectory differs from the intended helical trajectory, and no longer guarantees producing sufficient data for reconstruction. Data-insufficiency may create artifacts in a reconstructed image, and whether that happens or not depends on the scanned object. Induced artifacts are fundamental and cannot be corrected unless additional information is provided. It would be useful to identify these artifacts from other artifacts which are able to be corrected.

Conventional approaches assessed the global sufficiency condition for an untruncated source trajectory. In this thesis we proposed a measure to quantify the degree to which the data-sufficiency condition is violated at local level, for any arbitrary source trajectory. The proposed approach is specific: voxels found to violate local sufficiency condition definitely pose a reconstruction problem. The proposed approach is independent from the choice of reconstruction algorithm. We have verified the measure in the cases where severe rigid motion and/or detector truncation exist. In all cases, the measure indicated the regions for which insufficient data had been acquired and correctly predicted the regions which suffer from reconstruction artifacts. However, the method does not have perfect sensitivity: we show that in special cases, the local sufficiency

condition is not violated, although the acquired data are not sufficient for exact reconstruction.

# List of symbols

| | |
|---|---|
| $\mu$ | attenuation coefficient |
| $\mu^k$ | attenuation image at $k$th iteration |
| $I_0$ | number of photons before attenuation |
| $I_s$ | number of photons after attenuation |
| $ds$ | distance photon beam travels |
| $\theta$ | rotation angle |
| $FT_1$ | 1D Fourier transform |
| $FT_2{}^{-1}$ | 2D inverse Fourier transform |
| $(x, y)$ | 2D world coordinate system |
| $(r, s)$ | 2D polar coordinate system |
| $f(x, y)$ | 2D object function |
| $p(r, \theta)$ | 2D projection at $\theta$ |
| $\hat{f}(x, y)$ | 2D backprojection |
| $F(\theta, \omega)$ | 2D Fourier transform of $f(x, y)$ |
| $P_\theta(\omega)$ | 2D Fourier transform of $p(r, \theta)$ |
| $p\prime(r, \theta)$ | 2D filtered projection |
| $f(x, y, z)$ | 3D object function |
| $p(\beta, \gamma, v)$ | 3D projection at $\theta$ |
| $g(r)$ | parallel-beam ramp filter |
| $g\prime(\gamma)$ | come-beam (curved detector) ramp filter |
| $W_1$ | pre-weighting factor in FDK |
| $W_2$ | backprojection weighting factor in FDK |
| $l_p$ | pitch of the helix |
| $p_i$ | discrete projection at ray $i$ |
| $b_j$ | discrete backprojeciton at voxel $j$ |
| $a_{ij}$ | intersection length of ray $i$ with voxel $j$ |
| $b_i$ | measured value of ray $i$ in a blank scan |
| $y_i$ | measured value of ray $i$ in transmission scan |
| $\hat{y}_i$ | expected value of ray $i$ in transmission scan |
| $l_i$ | measured line integral at projection ray $i$ |
| $\hat{l}_i$ | expected line integral at projection ray $i$ |
| $\delta^2$ | local variance of transmission scan |
| $\alpha$ | step size of a update equation |

| | |
|---|---|
| $v$ | velocity rate of momentum |
| $\nabla f(\mu^k)$ | gradient of the cost function $f$ at $\mu^k$ |
| $P(y)$ | probability of $y$ |
| $P(\hat{y})$ | probability of $\hat{y}$ |
| $P(y\|\hat{y})$ | probability of $y$ when $\hat{y}$ happens |
| $L(\mu)$ | log-likelihood function |
| $R(\mu)$ | log-prior function |
| $\Phi(\mu)$ | log-posterior function |
| $S(\mu)$ | surrogate function of the prior |
| $\lambda$ | weighting of the prior |
| $c = (x, y, z)$ | 3D world coordinate system |
| $c\prime = (u, v, z)$ | 3D detector coordinate system |
| $S_{world}$ | rigid motion parameters in $c$ |
| $S_{detector}$ | rigid motion parameters in $c\prime$ |
| $S_b$ | subset of projections |
| $l_\theta$ | measured line integrals of projection at $\theta$ |
| $s_\theta^n$ | rigid motion parameters of view at angle $\theta$ at $n$th iteration |
| $r$ | motion parameter to be estimated |
| $\hat{r}$ | actual change in the pose parameter |
| $\Delta r$ | small known increment of the parameter to be estimated |
| $T_{world}$ | transformation matrix of the rigid motion in $c$ |
| $T_{detector}$ | transformation matrix of the rigid motion in $c\prime$ |
| $t_{offset}$ | offset between the $c$ and $c\prime$ in direction of bed movement |
| $\{\vec{l}\}$ | vectors of projection lines through the voxel |
| $\{\vec{n}\}$ | vectors of the planes through the voxel |
| $O$ | source position in world coordinate system |
| $C1, C2, C3, C4$ | rectangular detector corners in world coordinate system |
| $I$ | intersection point between the ray and the detector |

# List of abbreviations

| | |
|---|---|
| 2D | Two-dimensional |
| 3D | Three-dimensional |
| ART | Algebraic reconstruction technique |
| BPF | Backprojection filter |
| B-ICD | Block iterative coordinate descent |
| CPU | Central Processing Unit |
| CT | Computed tomography |
| CUDA | Compute Unified Device Architecture |
| FBP | Filtered backprojection |
| FDK | Feldkamp-Davis-Kriss |
| FFOV | Full field-of-view |
| FOV | Field-of-view |
| FWHM | Full width at half maximum |
| GPU | Graphical Processing Unit |
| ICD | Iterative coordinate descent |
| MAPTR | Maximum a posterior transmission tomography |
| ME/MC | Motion estimation/ Motion compensation |
| MLEM | Maximum likelihood expectation maximization |
| MLTR | Maximum likelihood transmission reconstruction |
| MSSIM | Mean structural similarity |
| OpenCL | Open Computing Language |
| OSEM | Ordered subset expectation maximization |
| OSTR | Ordered subset transmission tomography |
| PET | Positron emission tomography |
| PWLS | Penalized weighted least squares |
| RMSE | Root-mean-square error |
| ROI | Region-of-interest |
| SART | Simultaneous algebraic reconstruction technique |
| SIRT | Simultaneous image reconstruction technique |
| SPECT | Single-photon emission computed tomography |
| TV | Total variation |
| WLS | Weighted least squares |

# Contents

# Contents

# Part I

# Introduction

# Chapter 1

# Evolution of X-ray CT

Wilhelm Röntgen discovered the X-rays in 1895 and he was awarded with the Nobel Prize in physics in 1901 for that. Soon this discovery caught significant interest in the medical field, since X-rays were proven to have the capability of visualizing the human anatomy in a non-interventional way. Although this was an important breakthrough, X-ray imaging only provided a single two-dimensional (2D) projection of the three-dimensional (3D) irradiated object. The acquired image lacked information on soft tissue and low-attenuating organs. Later, some researchers proposed an improved X-ray system to overcome the limited contrast of the measured projection. The idea is that, by moving the X-ray source and/or the detector, one can acquire multiple 2D projections of the object at different positions. Then these projections can be combined by shifting them such that contributions from a particular image plane are always accumulated at the same position, whereas the contributions from other planes are averaged out. This provides some depth information, which improves the visualization of the low contrast region. The rationale behind it led to the development of breast tomosynthesis today. However, the planes above or below the central plane are always blurred in the computed image.

Cormack and Hounsfield were awarded the Nobel Prize in medicine for the invention of computed tomography (CT) Imaging. CT eliminates the blurring created by superimposing different projections. The excellent quality of the CT image makes it one of the most commonly used medical imaging modalities nowadays. Fig. 1.1 demonstrates how the first generation CT scanner works: the X-ray tube emits a pencil beam at one position, which is recorded by a single detector; to scan the whole object at one angle, the detector translates together with the source in one direction, generating a 1D projection (profile); after that the system rotates to several different angles (from 0° to 180°),

and the above acquisition process is repeated at these sampled angles. The resulting data are a set of 1D projections acquired at a series of acquisition angles, uniformly sampled over 180 degrees. By reconstructing an image from this measurement, Hounsfield obtained the very first image of the human head anatomy.
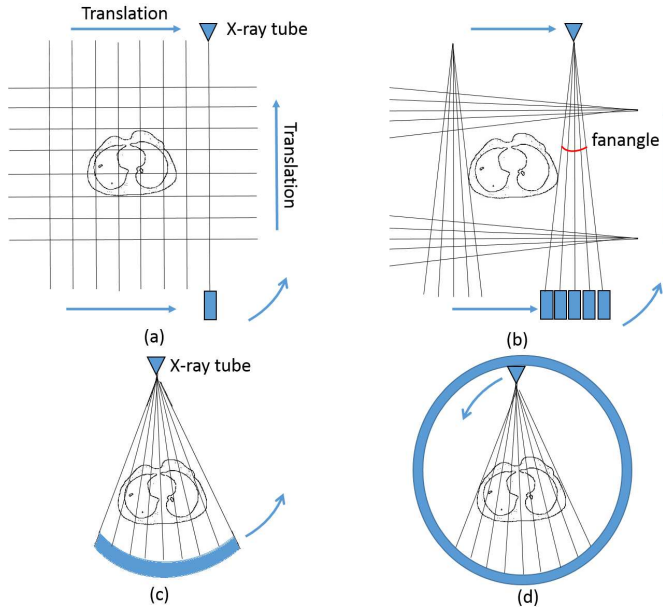


Figure 1.1: Four generations (from (a) to (d)) of CT scanners.

One problem with the first generation CT system is the relatively long acquisition time, e.g. 4-6 mins for a head scan. Second generation CT improves this by introducing a narrow fan-beam, instead of the pencil-beam, with increased number of detectors (Fig. 1.1b). Still the fan angle is small ($\sim 10°$) and the X-ray tube and detector array need to be translated to cover the object before the gantry is rotated. A major improvement was made in the third generation CT, with a substantially larger fan angle to further increase the scan coverage of one exposure (Fig. 1.1c). As a result, the translation of the source and detector is no longer necessary, so the acquisition time of one scan is reduced significantly. Fourth generation CT differs from the third generation one in the design of the detector array, but not in the X-ray source (Fig. 1.1d). The detector array in this generation forms a ring with up to 5000 single elements remaining stationary during a scan, while the X-ray source still rotates in a circular trajectory. The fourth generation CT reduces the possible artifacts due to the misaligned position of the moving detector. Most of the medical X-ray CT scanners today are based on the concept of the third generation CT.

One of the most commonly used scan procedures is the helical scan, which was introduced in early 1990s. Before its appearance, large volumetric data were

acquired in so-called step-and-shoot mode, which contains a bed movement phase and a data acquisition phase using a circular trajectory. In contrast, helical scanning allows simultaneous data acquisition while the bed is moving. The gantry rotation and the bed movement form a virtual X-ray trajectory with helical shape, which guarantees the full coverage of the scan region (Fig. 1.2a).
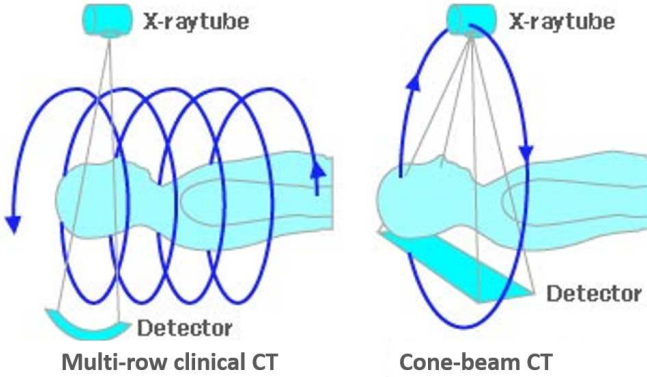


Figure 1.2: Left: multi-row clinical CT, right cone-beam CT.
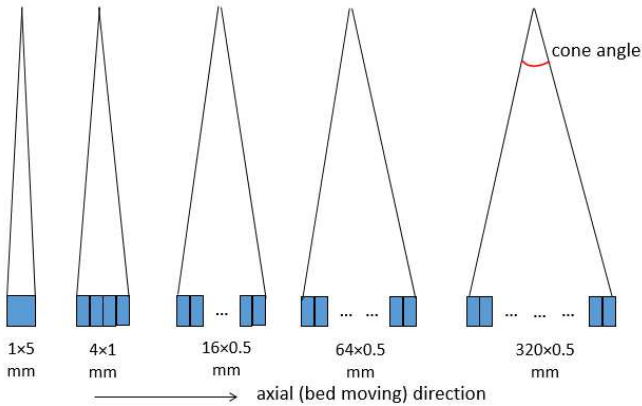


Figure 1.3: Increased axial coverage of the multi-row CT detector, makes it transit to a full cone-beam scanner.

In 1990s multiple-row CT was invented, thanks to advanced detector technologies. As a consequence, the axial coverage of a CT has been increasing steadily (Fig. 1.3). With increasing axial extent of the detector, CT acquisition time can be shortened, hence reducing the possibility of motion artifacts and enabling dynamic imaging of a target organ without table movement. Aside from clinical multi-row CT, cone-beam CT is another scanner that is commonly used in medical imaging (Fig. 1.2b). All micro-CT and C-arm CT scanners belong

Table 1.1: Typical state-of-art scanning parameters of clinical multi-row CT and cone-beam CT systems

|                      | Clinical CT | cone-beam CT |
|----------------------|-------------|--------------|
| Detector matrix size | 920×64      | 1024×1024    |
| Detector pixel size  | 0.3 mm      | 0.15 mm      |
| Contrast             | 3 HU        | 30 HU        |
| Dynamic range        | 20 bit      | 10 bit       |
| Dose efficiency      | 90 %        | 50 %         |
| Lowest rotation time | 0.25 s      | 3 s          |
| Frame rate           | 6000 fps    | 30 fps       |
| X-ray power          | 120 kW      | 20 kW        |
| Peak voltage         | 70-150 kVp  | 30-120 kVp   |

to this category. Movement trajectory of the source is often circular but could be more flexible, e.g. helical or other irregular shapes, depending on the particular application. Similar to the multi-row CT, cone-beam CT has a large axial detector and cone angle could be up to 40-60°. The main difference is the detector technology: cone-beam CT uses flat-panel based, while clinical multi-row CT uses dedicated curved detector. A summary of the technical differences between a common clinical multi-row CT and a common cone-beam CT is listed in Table 1.1.

# Chapter 2

# X-ray physics

X-ray physics describes how X-rays are generated and measured in a CT scanner. In this section we will discuss following physical processes: (1) X-ray generation, (2) X-ray interactions with matter, and (3) X-ray detection.

## 2.1  Generation of the X-ray

Medical X-rays are generated in a vacuum tube which contains one anode and one cathode (Fig. 2.1). Electrons are emitted from a cathode filament, which is heated by a current to reach beyond the binding energy of these electrons on the cathode. The formed electron beam is accelerated towards the anode by the tube voltage between the anode and cathode. A typical acceleration voltage is chosen between 25-150 kV for the diagnostic imaging purpose. The focus spot of the electron beam on the anode is controlled by a magnetic field - a control process which is referred to as electron optics (Rose 2008).

Deceleration happens when the electron beam reaches the surface of the anode. The energy carried by electrons is released in several ways during the deceleration (Fig. 2.2):

(1) Heat production - direct collision between the electron and outer shell electron of the anode. The full energy is transferred to the outer shell electron and gradually emitted as heat.

(2) Bremsstrahlung - interaction between the electron and the nucleus. The path of the electron is bended around the nucleus and the loss of kinetic energy is emitted as a photon.

(3) Characteristic radiation - direct interaction of a fast electron with an inner shell electron of the anode. The inner shell electron is emitted out and an outer shell electron fills the original position, during which a photon is emitted.

Figure 2.1: A typical medical X-ray tube.
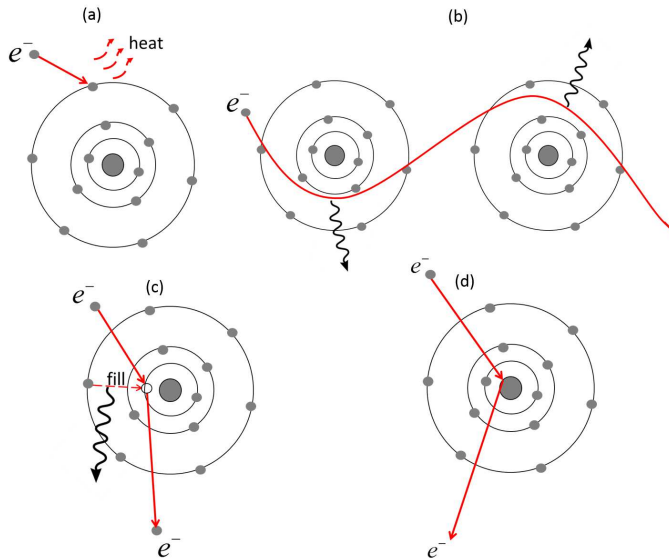


Figure 2.2: Several energy release processes might happen when an electron arrives at the anode: (a) heat production; (b) bremsstrahlung; (c) characteristic effect; (d) direct collision.

(4) Direct electron-nucleus collision - A electron is scattered without energy loss, and continues travelling in a different direction until next interaction happens.

Considering the tube acceleration voltage, direct electron-nucleus collision hardly happens in X-ray CT imaging. In fact emission of the X-ray photons are mainly due to a combination effect of (2) and (3), and the bremsstrahlung effect contributes more than characteristic radiation does (at least for the material commonly used in medical X-ray tube, e.g. tungsten). The emitted X-ray photons from the tube are distributed within a continuous energy range, and a typical energy spectrum is shown in Fig. 2.3. The reason of the presence of this continuous distribution is that, bremsstrahlung can have any energy, ranging from zero to maximum kinetic energy of the electron, depending on the degree that the electron is affected by the nucleus (Fig 2.2b). The maximum kinetic energy of the electron is determined by the tube voltage between the anode and the cathode. The number of the emitted X-ray photons is determined by the cathode current.
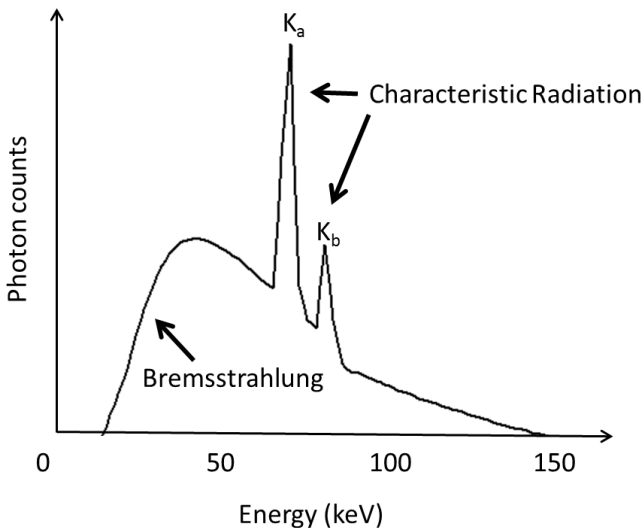


Figure 2.3: X-ray spectrum of a tungsten anode (without filtering) at tube acceleration voltages of 150 kVp (peak kilo-voltage).

## 2.2   Interaction between X-ray and matter

After emission, the X-ray photons travel towards the object and some of them interact with the matter when passing through that object. As a result, the number of photons measured by the detector is less than the number emitted.

This process is often called attenuation of the X-ray photons. The attenuation coefficient defines how easy a photon beam penetrates the object. The linear attenuation coefficient describes the probability of attenuation per unit length, and it depends on the photon energy and the material being traversed (Fig. 2.4a). The mass attenuation coefficient is the linear attenuation coefficient divided by the material density. If we are able to obtain the attenuation value for a particular energy at one voxel, we would have useful (but incomplete) information of which material is located at that pixel.

## 2.2.1 Beer-Lambert's law
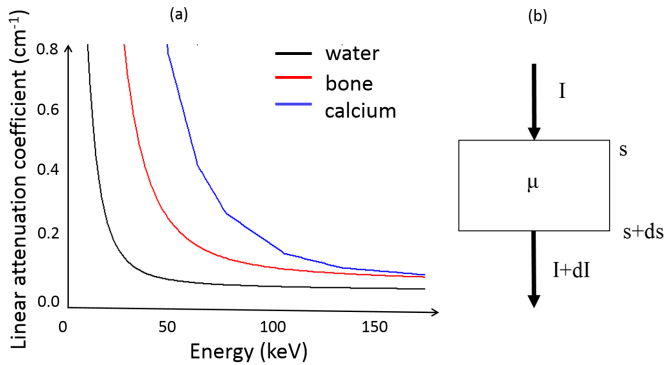


Figure 2.4: (a) Energy dependent linear attenuation coefficient for bone, water, and calcium. (b) X-ray beam travels through a slice of material with attenuation coefficient $\mu$.

Here a mathematical expression of the photon attenuation is given. First, let us see a simple case where all emitted photons have the same energy. In this case a monochromatic X-ray beam propagates over a distance $ds$ through the object (Fig. 2.4b). The linear attenuation coefficient $\mu$ is defined as the fraction of the X-ray beam attenuated per unit distance. The intensity (number of photons) before the attenuation is $I$, after the attenuation is $I + dI$. The change of the intensity can be written as:

$$dI = -I\mu ds \qquad (2.1)$$

This gives:

$$\frac{dI}{I} = -\mu ds \qquad (2.2)$$

Integrating both sides:

$$I_s = I_0 \cdot \exp(-\int_0^s \mu(s) \cdot ds) \tag{2.3}$$

known as **_Beer-Lambert's law_**, which is the fundamental of X-ray CT imaging. $I_0$ is the number of photons that would be detected if no attenuation was present, $I_s$ is the number of photons after attenuation along path $s$. For a real, polychromatic X-ray source, the integration on the right hand side must be over all energies:

$$I_s = \int_{E_{\min}}^{E_{\max}} I_0(E) \cdot \exp(-\int_0^s \mu(E, s) \cdot ds) dE \tag{2.4}$$

### 2.2.2 Interaction with matter

Beer-Lambert's law describes the mathematical process of X-ray photon attenuation, which can happen in several forms of physical processes, distinguished by the changes to the energy or travelling direction of a photon (Fig. 2.5):

(1) Photoelectric effect – at low energies, the entire energy of the photon is absorbed by an atom, and an inner shell electron is emitted from the atom as a photoelectron. The resulting vacancy is filled by an electron from an outer shell, during which a characteristic X-ray fluorescence photon is generated. The closer the photon energy is to the K-shell binding energy, the more likely photoelectric effect is going to happen.

(2) Compton scattering – at middle energies, part of the photon energy is lost during the interaction between the photon and the outer shell electron. As a consequence, a scattered photon with less energy than incoming photon propagates in a different direction. The energy difference is consumed to emit the outer shell electron from the atom. A similar phenomenon is Rayleigh or Thomson scattering, during which there is no energy loss for the scattered photon. Compton scattering can be well modelled as a collision between the photon and a loosely bounded electron, Rayleigh scattering can be modelled as a collision between the photon and the entire atom.

(3) Pair production – at high energies, the photon may interact directly with the nucleus, generating a positron and an electron. The positron then travels a short distance in the matter and interacts with another electron, producing two 511 keV photons which are emitted in opposite directions. This process is called annihilation.

Photoelectric and Compton scattering are the main causes of attenuation in medical X-ray imaging. A composition of all these effects on the mass attenuation coefficient of water is shown in Fig. 2.6.
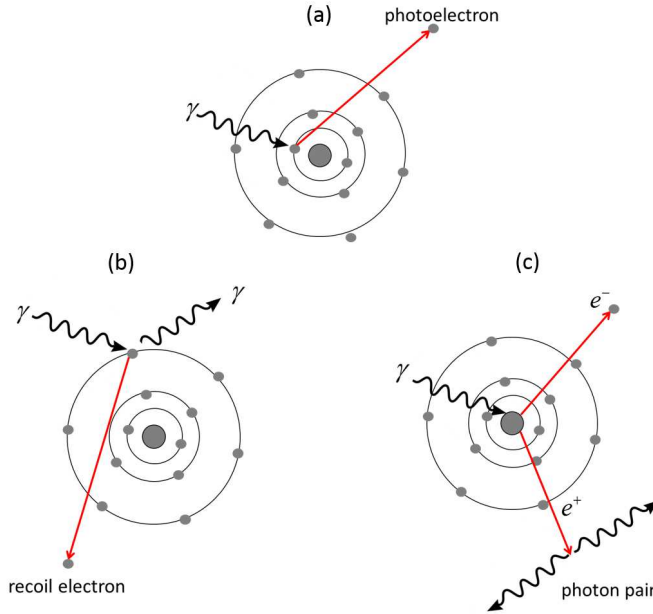
Figure 2.5: Possible X-ray photon interaction processes with the matter: (a) photoelectric absorption; (b) Compton scattering; (c) pair production.
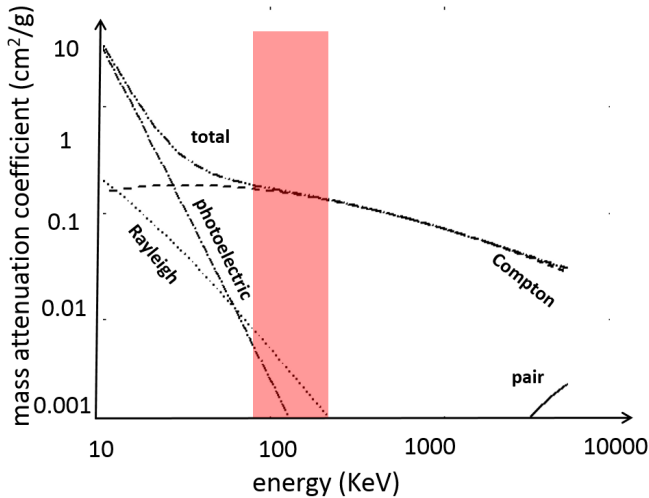


Figure 2.6: Mass attenuation coefficient of water at different photon energy levels. Contribution from different interactions are plotted in different curves. diagnostic window is in red. Plotted data are from NIST XCOM database (https://physics.nist.gov/cgi-bin/Xcom/).

## 2.3   X-ray detection

An X-ray detector measures the amount of the X-ray photons hitting the detector. The conventional energy integrating detector does this in an "indirect" way by measuring the output of interactions between the photons and the detector, i.e. Compton scattering and Photoelectric effect (Fig. 2.7a). A typical process of how an integrating detector measures photons is illustrated below: (1) X-ray photons travel into the scintillator and transfer part of their energy into kinetic energy of electrons; (2) the kinetic energy of these electrons excites a large number of bound electrons; (3) the excited electrons return to their ground state, producing light photons in the scintillator; (4) in the photodiode, the light photons convert to pairs of electrons and holes which create a measurable electric current; (5) analog-to-digital (A/D) converters yield the final measured values, which are proportional to the total energy deposited in the detector. Most of the multi-row CT detectors, and many cone-beam CT detectors use such detectors to perform "indirect" conversion from photons to charge.

One disadvantage of the integrating detectors is that they usually produce very complicated measurement statistics due to the numerous sources of variations, which originate from the above five steps. Some cone-beam CT detectors utilize "direct" conversion, by replacing the scintillator and the photodiode in an integrating detector with an array of X-ray photosensor (Fig. 2.7b). The X-ray photosensor has the ability to convert the X-ray photons directly to electrical signal, hence avoids multiple random processes that happen in a scintillator.
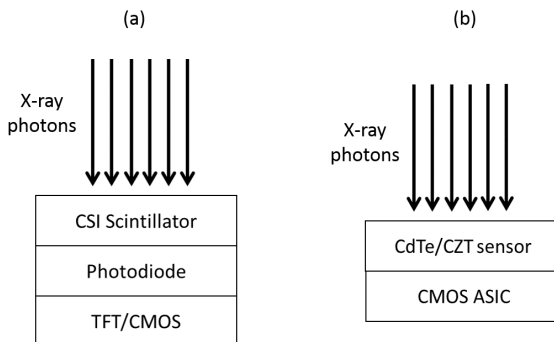


Figure 2.7: (a) "Indirect" conversion detector used in clinical multi-row CT and some cone-beam CT. (b) "direct" conversion detector used in some cone-beam CT.

Based on the "direct" conversion detector, a new design of detector named
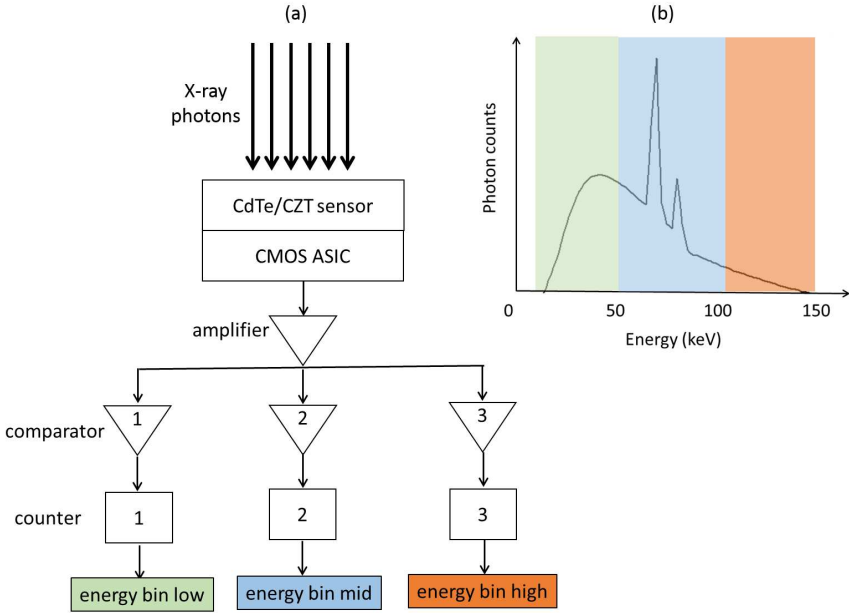
Figure 2.8: (a) Photon counting detector; (b) detected signals are grouped to different bins with different photon energies.

***photon-counting*** detector is emerging rapidly in the medical imaging field. Inherited from the "direct" conversion detector, it can convert X-ray photons directly to charges to be collected by electric circuits. Furthermore, it has the ability to detect each photon (and its estimate energy) individually with the help of fast read-out circuits. An individual photon is detected by checking if the induced charge is above a certain level (Fig. 2.8). Photons at different energy levels can be categorized into different bins with a set of predefined thresholds. The measurement in each bin can be assumed to follow a Poisson distribution provided the dead time losses are modest (Nuyts et al. 2013). Compared with an integrating detector, a photon-counting detector has better capability in distinguishing multiple materials even with lower radiation dose (Polster et al. 2016). It also provides a wider dynamic range, thanks to the measurement of the energy of the individual photons. Two downsides of the photon counting detector are: (1) spectral response may not be perfect as the detector can read one high energy photon as multiple low energy photons; (2) pulse pileup effect may cause loss of photons due to the limited count rate (Kappler et al. 2014). Given that the detector technology is still advancing, these issues will likely be solved in the future. More discussion about the photon-counting detector can be found in (Taguchi et al. 2013).

# Chapter 3

# Reconstruction

Image reconstruction is the process of recovering the representation of the object from the data measured by the detector. In this section, we will (1) introduce the key components of a reconstruction implementation – forward and backprojection; (2) introduce a precondition for an exact reconstruction – data-sufficiency; (3) review several analytical and iterative reconstruction algorithms currently used in clinics and research field; (4) discuss issues about the acceleration of an iterative reconstruction.

## 3.1 Projection and backprojection

In this section we first review two key concepts in a reconstruction process - projection and backprojection.

### 3.1.1 Projection

Beer Lambert's law describes the attenuation law of an X-ray passing through an object over a certain distance. Here we define the process of ***projection***. Let us consider a 2D object $f(x, y)$ which is irradiated by a set of 2D parallel rays (parallel-beam geometry in Fig. 3.1). A second coordinate system $(r, s)$ can be defined, and its relationship with $(x, y)$ coordinate system can be described as:

$$
\begin{aligned}
\begin{bmatrix} r \\ s \end{bmatrix} &= \begin{bmatrix} \cos\theta & \sin\theta \\ -\sin\theta & \cos\theta \end{bmatrix} \begin{bmatrix} x \\ y \end{bmatrix} \\
\begin{bmatrix} x \\ y \end{bmatrix} &= \begin{bmatrix} \cos\theta & -\sin\theta \\ \sin\theta & \cos\theta \end{bmatrix} \begin{bmatrix} r \\ s \end{bmatrix}
\end{aligned}
\tag{3.1}
$$

At $\theta$, if we apply a line integration of the object along all parallel lines, a density profile of the object is obtained:

$$p(r, \theta) = \int_{-\infty}^{\infty} \int_{-\infty}^{\infty} f(x, y)\delta(x\cos\theta + y\sin\theta - r)dxdy \qquad (3.2)$$

According to Eq. 3.1, this line integral at $\theta$ can be expressed in the coordinate system $(r, s)$:

$$p(r, \theta) = \int_{-\infty}^{\infty} f(r\cos\theta - s\sin\theta, r\sin\theta + s\cos\theta)ds \qquad (3.3)$$
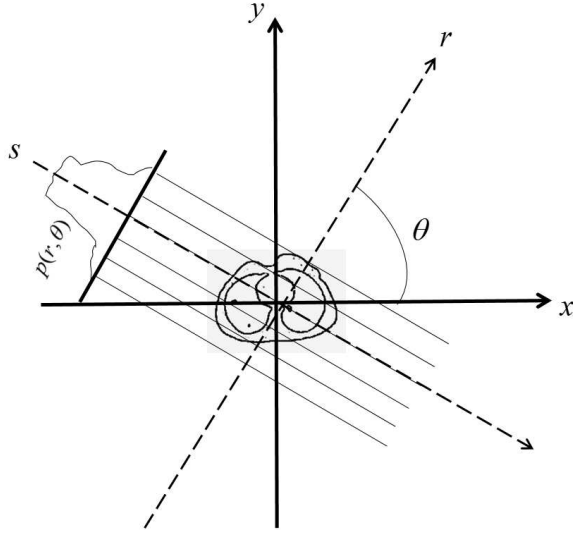


Figure 3.1: The projection process of an object in a parallel-beam geometry at projection angle $\theta$. Note the existence of two coordinate systems $(x, y)$ and $(r, s)$.

Above equation describes the projection process in 2D, and the resulting profile $p(r, \theta)$ is called projection at angle $\theta$. The projection process can be repeated for multiple angles in a parallel-beam geometry in Fig. 3.1, generating a set of 1D projections. Fig. 3.2 is an example showing a point and its projections across 360°. Note the sinusoid shape of the vertically stacked projections along angles, and because of that the 2D image by stacking the 1D projections is often called sinogram in tomography. Fig. 3.3 is an example of a 2D simulated Shepp-Logan phantom and its sinogram, which effectively can be viewed as a superposition of multiple sinusoids from projections of multiple points. In 2D,
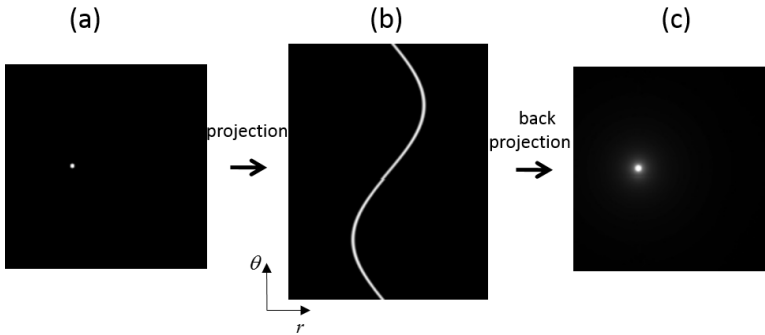
Figure 3.2: An example of (a) a point, (b) its sinogram and (c) its backpro-
jection, which recovers a blurred representation of the point. The projection
$p(r, \theta)$ in (b) is essentially a 2D image, where each row represents the projection
at a particular angle. Note that the projection if the point in (a) contributes a
sinosodial pattern in this image (as can be easily verified with Eq. 3.2).
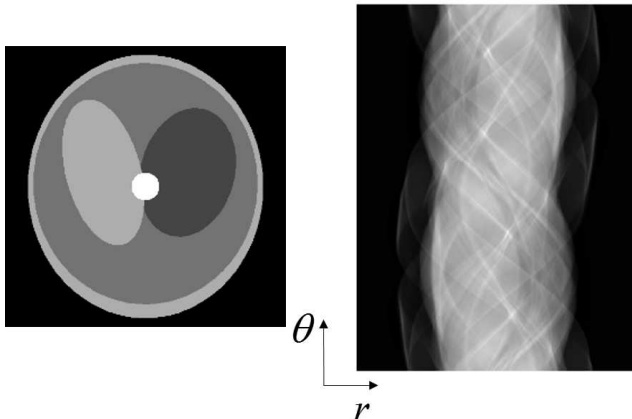


Figure 3.3: A 2D Shepp-Logan phantom and its sinogram.

both X-ray transform and Radon transform describe above process of generating projections at all angles. But in general, the two transforms are different - the X-ray transform produces the set of all line integrals, while the Radon transform produces a set of integrals over all hyperplanes.

The integral in Eq.3.3 assumes continuous models for object and detector representation. However, the computation of a projection process usually involves discretizing a real object in pixels. Also a detector is always discrete in real life. Hence, a discrete form of Eq. 3.3 is of great interest:

$$p_i = \sum_j a_{ij} f_j \qquad (3.4)$$

where $j$ is the index over image voxels $(x, y)$, $i$ is the index over sinogram pixels $(r, \theta)$, $a_{ij}$ represents the intersection length of projection line $i$ with voxel $j$.

## 3.1.2 Backprojection

The projection process maps a 2D object $f(x, y)$ to sinogram $p(r, s)$, consisting of all line integrals through the object. **Backprojection** is the adjoint operation of projection, which is defined as:

$$\hat{f}(x, y) = \int_0^\pi p(x \cos \theta + y \sin \theta, \theta) d\theta$$
$$= \int_0^\pi p(r, \theta) d\theta|_{r = x \cos \theta + y \sin \theta} \qquad (3.5)$$

In the parallel-beam geometry shown in Fig. 3.1, above equation "smears" all projection values back to the volume along the same projection lines used to produce the sinogram. Unfortunately backprojection does not recover the exact representation of the object but gives a blurred version of the object (Fig. 3.2c).

Again we are interested in a discrete version of Eq. 3.5, which is:

$$b_j = \sum_i a_{ij} p_i \qquad (3.6)$$

Backprojection is fundamental to all tomographic reconstruction algorithms.

## 3.2 Data-sufficiency

A precondition for an exact reconstruction is the ***data-sufficiency*** condition. Before designing a reconstruction algorithm for a specific imaging application, it is useful to determine whether the available data are sufficient or not for exact reconstruction of the attenuating object. Here, "exact reconstruction" means that the reconstruction problem has a unique solution and a stable estimate of that solution can be computed from noisy data. Orlov (1975) derived a data-sufficiency condition in parallel-beam tomography. Tuy (1983) extended it to a data-sufficiency condition in cone-beam tomography. Later Metzler et al. (2003a) identified the geometrical equivalence between Orlov's and Tuy's sufficiency conditions. Note that above conditions assume that all projections at all source positions are untruncated, i.e. all projection lines that intersect the object also intersect the detector.

An example acquisition scheme that violates the data-sufficiency condition is the popular circular cone-beam scan (Fig. 3.4a), which never provides sufficient data for an exact reconstruction. Tuy's condition states that, to reconstruct an object exactly, "there should exist at least one cone-beam source position on every plane that intersects the object"(Tuy 1983). For the cone-beam geometry in Fig. 3.4a, above statement is true only for the points within the source plane (i.e. the plane containing the circular source trajectory), but not for ones outside that plane. As a result, exact reconstruction is only possible within the source plane, and indeed, so-called cone-beam artifacts are typically observed for planes away from the source plane. On the other hand, Tuy's condition is satisfied if in addition to the circular trajectory, the source also moves along a line (Fig. 3.4b). If that line is long enough, then "all planes intersecting the object contain at least one cone-beam source position". For the same reason, a tilted circles source trajectory also satisfies data-sufficiency condition (Fig. 3.4c).
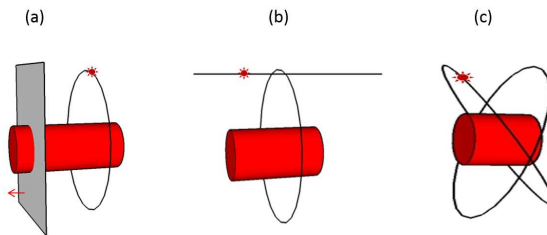


Figure 3.4: Illustration of three different source trajectories: (a) circle, (b) circle and line, (c) tilted circles. The red cylinder represents the object, the source (red asterisk) moves along the solid black lines to acquire the projections of the object. We assume the detector is infinitely large hence no truncation exists during every exposure.

Danielsson et al. (1997) and Tam et al. (1998) first extended the data-sufficiency condition to axially-truncated data in a helical scan. Because of the limited axial detector extent, helical cone-beam data are truncated in all projection views along the axial direction (rotation axis, Fig. 3.5). Tam and Danielsson independently proved that the minimum data required in each view for exact reconstruction is the set of projection values within a constant region. Noo et al. (2004) and Defrise et al. (2006) first derived a data-sufficiency condition for transaxially-truncated data from a scan with reduced fanangle. It was proven that a region-of-interest (ROI) can be reconstructed exactly from the truncated data if all integrals along lines intersecting the ROI are measured, and if that ROI also includes part of the background surrounding the object (Fig. 3.6a). Continuing from those results, Ye et al. (2007), Courdurier et al. (2008), Kudo et al. (2008) and Yu et al. (2009) derived a data-sufficiency condition for the interior problem, where the ROI is strictly within the object support. Assuming all line integrals are measured within an interior ROI, that ROI can be reconstructed exactly if the image values are known a priori in a finite subregion, or if the ROI itself is piecewise constant. All above sufficiency conditions can be viewed as being valid only for several special source trajectory shapes. However, there is currently no data-sufficiency condition general enough to deal with an arbitrary source trajectory shape. Development of a general sufficiency condition is still under investigation.

Another research direction is to investigate the relationship between the data-sufficiency and the degree of data sparsity. Compressed sensing has been shown to enable an acceptable reconstruction from sparsely sampled data (Sidky et al. 2008). Empirical studies showed the existence of a relation between the sparsity and data-sufficiency but yet a theoretical explanation is needed (Jørgensen et al. 2015, 2013).

## 3.3 Analytical reconstruction

After discussing the data-sufficiency condition, we will introduce several reconstruction algorithms in this and next sections. These algorithms are divided in two categories: analytical reconstruction algorithms and iterative reconstruction algorithms. These two categories mainly differ in two aspects: (1) an analytical reconstruction algorithm is based on the mathematical inversion, and gives a one-step solution. On the other hand an iterative reconstruction algorithm is based on the numerical inversion, and updates the image in an iterative way; (2) analytical reconstruction is based on a continuous representation of the object and the sinogram, discretization is only used to implement the algorithm. In contrast, an iterative algorithm starts from a discrete representation of the object and the sinogram. We will first introduce several analytical algorithms in this section.
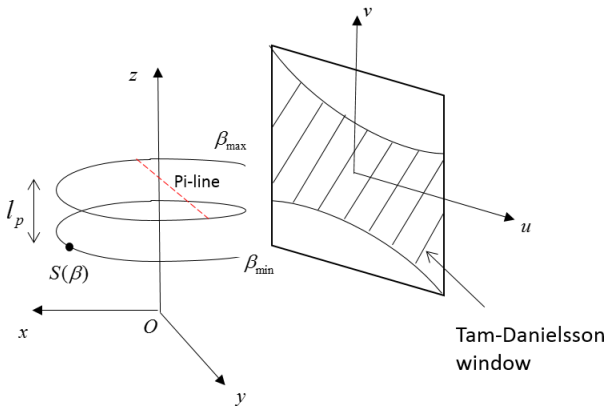
Figure 3.5: A scan setup in helical cone-beam geometry. The source $S$ runs from $\beta_{min}$ to $\beta_{max}$, the pitch of the helix is defined as the table increment per rotation divided by the beam collimation. We define a Pi-line (in red) as a segment with two endpoints located on the helix within one pitch. Tam et al. (1998) and Danielsson et al. (1997) proved that measurement in half turn of the helix would produce sufficient data for exactly reconstructing a voxel on the Pi-line. They also proved that there is one and only Pi-line through any voxel within the helix. In other words if no transaxial truncation is allowed, a set of Pi-lines would cover the whole object. Hence the data-sufficiency condition is satisfied. The Tam-Danielsson window (shaded region) is defined as the detector region in between projections of all Pi-lines within two consective turns of the helix.
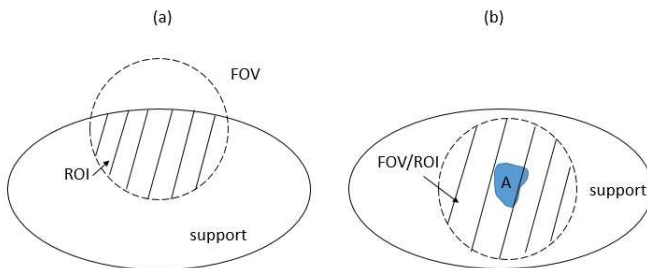


Figure 3.6: Two 2D data-sufficiency problems with transaxial truncation. The support of the object is bounded by the solid curve, and only points inside the dashed circle are projected onto the detector at every angle. Exact and stable reconstruction can be obtained within shaded ROI when either (a) part of the ROI is in the background, or (b) attenuation values are known a priori in a tiny region A, or the object inside the ROI is piecewise constant.

### 3.3.1 Direct Fourier reconstruction

In order to avoid the blurring effect in the image from a simple backprojection (Fig. 3.2c), we need an "exact inverse" operation of the projection. The **Fourier slice theorem**, also known as the central slice theorem, describes the mathematical relationship between an image and its projections. It provides theoretical support for "exact inverse" operation. The Fourier transform of a 2D object is:

$$F(\omega_x, \omega_y) = \int\limits_{-\infty}^{\infty} \int\limits_{-\infty}^{\infty} f(x,y)e^{-j2\pi\omega_x x}dx \ e^{-j2\pi\omega_y y}dy \qquad (3.7)$$

According to

$$\begin{cases} \omega_x = \omega\cos\theta \\ \omega_y = \omega\sin\theta \end{cases}$$

We have

$$F(\theta, \omega) = \int\limits_{-\infty}^{\infty} \int\limits_{-\infty}^{\infty} f(x,y)e^{-j2\pi w(x\cos\theta + y\sin\theta)}dxdy$$

According to Eq. 3.1, we can replace $x$ and $y$ to $s$ and $r$:

$$F(\theta, \omega) = \int\limits_{-\infty}^{\infty} \int\limits_{-\infty}^{\infty} f(r\cos\theta - s\sin\theta, r\sin\theta + s\cos\theta)e^{-j2\pi\omega r}drds$$

$$= \int\limits_{-\infty}^{\infty} \int\limits_{-\infty}^{\infty} f(r\cos\theta - s\sin\theta, r\sin\theta + s\cos\theta)ds \ e^{-j2\pi\omega r}dr$$

Based on Eq. 3.3, we have the Fourier transform of a 2D object as:

$$F(\theta, \omega) = \int\limits_{-\infty}^{\infty} p(r, \theta)e^{-j2\pi\omega r}dr$$

$$F(\theta, \omega) = P_\theta(\omega) \qquad (3.8)$$

This implies that the 1D Fourier transform of the parallel projection at angle $\theta$, equals the profile along the radial line in the 2D Fourier transform of the object at the same angle (Fig. 3.7). This relationship is referred to as the Fourier slice theorem. If a sufficient number of projections are measured, $F(\theta, \omega)$ would

be known at all positions in the frequency domain. According to Eq. 3.8, the object can be exactly reconstructed by applying a 2D inverse Fourier transform for the 1D Fourier transform of the projections. The actual implementation of this reconstruction process includes three steps:

(1) Compute the 1D Fourier transforms of the projections at all angles, resulting in $F(\theta, \omega)$

$$F(\theta, \omega) = FT_1\{p(r, \theta)\}$$

(2) Convert $F(\theta, \omega)$ from polar coordinate to Cartesian coordinate in the Fourier domain

$$F(\omega_x, \omega_y) = gridding\{F(\theta, \omega)\}$$

(3) Apply the 2D inverse Fourier transform to obtain the reconstructed image

$$f(x, y) = FT_2^{-1}\{F(\omega_x, \omega_y)\}$$

Above steps is often called **direct Fourier reconstruction**. Although this approach is straightforward, one has to convert $F(\theta, \omega)$ to Cartesian coordinates before applying the inverse Fourier transform. This involves an interpolation process called *gridding*, which is sensitive to errors in frequency domain (Natterer 2001).
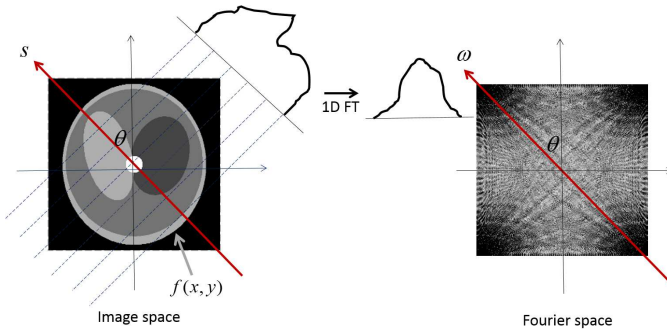


Figure 3.7: Fourier slice theorem. The 1D Fourier transform of the projection $p(\theta)$ equals the central profile at angle $\theta$ through the 2D Fourier transform of the object.

## 3.3.2 Filtered backprojection

Another analytical reconstruction algorithm is **filtered backprojection** (FBP), which can be derived from the Fourier slice theorem as well. It has the advantage of avoiding the gridding in the direct Fourier reconstruction. To obtain FBP, one first obtains $f(x, y)$ by rewriting Eq. 3.7:

$$f(x,y) = \int\limits_{-\infty}^{\infty} \int\limits_{-\infty}^{\infty} F(\omega_x, \omega_y) e^{j2\pi(\omega_x x + \omega_y y)} dx dy \tag{3.9}$$

Express $F(\omega_x, \omega_y)$ in a polar coordinate system $(\theta, \omega)$:

$$f(x,y) = \int\limits_{0}^{\pi} \int\limits_{0}^{\infty} F(\theta, \omega) \left|\omega\right| e^{j2\pi\omega r} d\omega d\theta|_{r = x\cos\theta + y\sin\theta} \tag{3.10}$$

where $|\omega|$ is Jacobian of the coordinate transform. According to Eq. 3.8, $F(\theta, \omega)$ can be replaced by a 1D Fourier transform of the projection $P_\theta(\omega)$:

$$f(x,y) = \int\limits_{0}^{\pi} \int\limits_{0}^{\infty} P_\theta(\omega) \left|\omega\right| e^{j2\pi\omega r} d\omega d\theta|_{r = x\cos\theta + y\sin\theta} \tag{3.11}$$

where $|\omega|$ can be viewed as a filtering operation, which allows high frequency information to pass but suppresses low frequency information (Fig. 3.8). Because of the shape, we often call this filter the ramp filter. Let us define the inner integration over $\omega$ in Eq. 3.11 as $p'(r, \theta)$:

$$p'(r, \theta) = \int\limits_{0}^{\infty} P_\theta(\omega) \left|\omega\right| e^{j2\pi\omega r} d\omega \tag{3.12}$$

Put $p'(r, \theta)$ back to Eq. 3.11, we arrive at the fact that $f(x, y)$ can be exactly reconstructed by integrating the filtered projections at all angles:

$$f(x,y) = \int\limits_{0}^{\pi} p'(r, \theta) d\theta|_{r = x\cos\theta + y\sin\theta} \tag{3.13}$$

Compared with Eq. 3.5, the only difference is Eq. 3.13 filters the projection whereas the regular backprojection does not. Hence the derived algorithm is called filtered backprojection. An alternative to filtering the projections in frequency domain is convolving the projections in spatial domain (Fig. 3.8), which leads to a different implementation of FBP (Zeng 2015):

$$p'(r, \theta) = p(r, \theta) \otimes g(r)$$

$$where \quad g(r) = W \frac{\sin(2\pi W r)}{\pi r} - \frac{\sin^2(\pi W r)}{(\pi r)^2} \tag{3.14}$$

$\otimes$ denotes convolution, $W$ is the cutoff frequency typically chosen to be the Nyquist frequency. Ramp filtering or convolution can be further combined with low pass filtering, e.g. Hann filtering, to remove the undesired noise in the measured data.
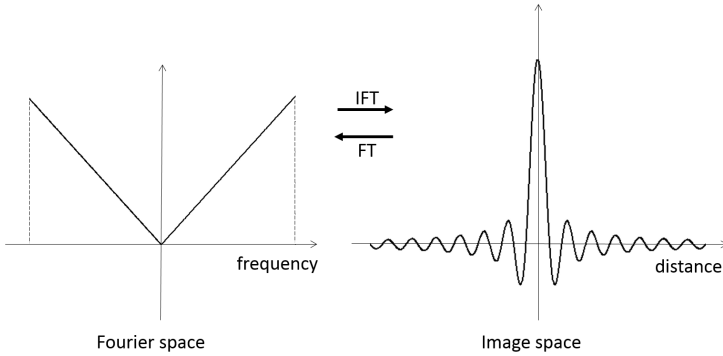


Figure 3.8: Filtering in frequency domain equals convolution in spatial domain, of which the kernel is the Fourier transform of the response function in the frequency domain. More details about the ramp filtering can be found in (Zeng 2015).

Note that the FBP algorithm derived above is only valid in a 2D parallel-beam geometry. In this thesis we are interested to derive an FBP-like algorithm that works for a 2D fan-beam geometry with curved detector. One can choose to rebin the fan-beam data to parallel-beam ones before the reconstruction (Herman et al. 1976). But a rebinning process involves interpolation which might compromise the spatial resolution of a reconstructed image. An alternative choice is to extend the parallel-beam FBP algorithm to fan-beam one. Fig. 3.9 shows the coordinates transformation between a parallel-beam geometry $(r, \theta)$ and a fan-beam one $(\gamma, \beta)$. $\beta$ is the angle between the central ray of the fan and the y-axis, $\gamma$ is the angle between a ray and the central ray of the fan, fan angle is $\Delta\gamma$, $R$ is distance between the source and the center of the rotation. The transformation between two coordinates is:

$$\begin{cases} \theta = \gamma + \beta \\ r = R \sin \gamma \end{cases} \tag{3.15}$$

A fan-beam FBP algorithm for geometry in Fig. 3.9b first requires adjusting on the ramp filtering in Eq. 3.14:
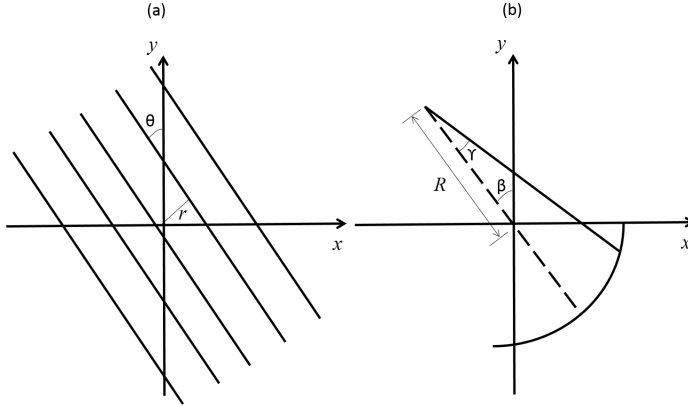
Figure 3.9: (a) A parallel-beam geometry and (b) a fan-beam geometry. The detector in the fan-beam geometry is equiangular since the detector elements are distributed uniformly along the fanangle.

$$g'(\gamma) = \left(\frac{\gamma}{\sin \gamma}\right)^2 g(\gamma) \tag{3.16}$$

where $g(\gamma)$ is the parallel-beam ramp filter.

A FBP algorithm for geometry in Fig. 3.9b also requires additional weightings to be introduced. A first weighting factor is the pre-weighting applied before applying the ramp-filtering. A second weighting is backprojection weighting applied during the backprojection operation. These two weighting factors have the expression below:

$$W_1 = \cos \gamma$$
$$W_2 = \frac{R}{(x + R \sin \beta)^2 + (y - R \cos \beta)^2} \tag{3.17}$$

After modifying the ramp filtering and introducing the additional weights, the resulting fan-beam FBP algorithm (with curved detector) is:

$$f(x, y) = \frac{1}{2} \int_0^{2\pi} W_2 \int_{-\Delta\gamma/2}^{\Delta\gamma/2} \{(W_1 p(\gamma, \beta)) \otimes g'(\gamma)\} d\gamma d\beta \tag{3.18}$$

In a 360° circular scan (2D), measured data are redundant for reconstruction. For a parallel-beam geometry, data from a 180° scan is enough for a reconstruction. For a fan-beam geometry, data from a short scan (scan view range

$[0, \alpha]$, $\alpha \in [\pi + \Delta\alpha, 2\pi]$) is enough for a reconstruction. When reconstructing a short scan, some proper weighting function needs to be introduced to handle the redundancy in each projection view (Parker 1982; Silver 2000). This process is often referred to as Parker's weighting.

### 3.3.3   3D approximate reconstruction

The 2D fan-beam FBP algorithm can be extended into a 3D cone-beam one. In a circular cone-beam geometry, we know that measured data are not sufficient for reconstruction. For this geometry, a type of reconstruction algorithms uses all data and accounts for the obliqueness of the projection lines by adjusting backprojection weights. An example is the **_Feldkamp-Davis-Kress_** (FDK) algorithm (Feldkamp et al. 1984). FDK is an approximate reconstruction algorithms - as the number of modern scanner detector rows increases, their approximate errors outside the central plane are no longer negligible.
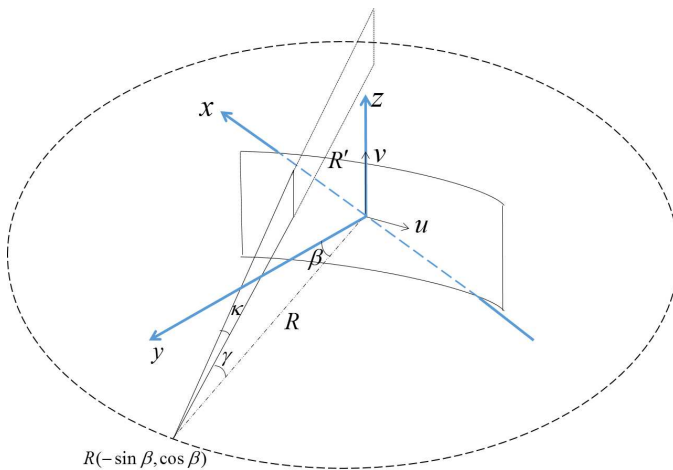


Figure 3.10: Circular cone-beam geometry with a virtual cylindrical detector in the center of field-of-view (FOV). $R$ is the distance between the source and the rotation center, $R'$ is the distance between the source and the voxel, $r$ is the fanangle increment of a perticular ray, $k$ is the coneangle increment of a particular ray.

We hereby describe the FDK algorithm as a representation of the 3D approximate algorithms for a circular cone-beam geometry. Let us consider the algorithm for the measured cone-beam data from sources on a circular trajectory. In the coordinate system defined in Fig. 3.10, we denote the trajectory as $R(-\sin\beta, \cos\beta)$. The detector is in cylindrical shape. A virtual cylindrical detector $(\gamma, v)$ is placed on the axis of rotation so that v-axis coincides with the z-axis. The cone-beam measured data are represented as $p(\beta, \gamma, v)$. From

Eq. 3.18, circular cone-beam FDK algorithm reconstruct $f(x, y, z)$ by:

$$f(x, y, z) = \frac{1}{2} \int\limits_{0}^{2\pi} W_2 \int\limits_{-\Delta\gamma/2}^{\Delta\gamma/2} \{(W_1 p(\beta, \gamma, v)) \otimes g(\gamma)\} d\gamma d\beta$$

$$\text{where} \quad v = \frac{zR}{\sqrt{(x + R\sin\beta)^2 + (x - R\cos\beta)^2}}$$

$$W_1 = \cos k \cos\gamma$$

$$W_2 = \frac{R^2}{R'^2} = \frac{R^2}{(x + R\sin\beta)^2 + (y - R\cos\beta)^2 + (z - v)^2}$$

(3.19)

where again $W_1$ is the pre-weighting term, $W_2$ is the backprojection weighting term. In practice, circular FDK algorithm is implemented in four steps:

(1) Multiply the projections with both column-dependent weight $\cos\gamma$ and row-dependent weight $\cos k$.

(2) Apply the Parker's weighting to the data if the scan is a short scan. For simplicity it is not shown in Eq. 3.19.

(3) Apply the ramp filtering along each row in each projection. Often implementation is via 1D convolution along the rows in each projection.

(4) Compute the weighted backprojection from the filtered projections.

The computation of the FDK algorithm is straightforward and parallelizable. Despite its approximate nature, FDK is found to be robust and accurate for many clinical applications. However, as illustrated in the beginning of this section, cone-beam artifacts are becoming a problem when the axial detector extent becomes very large. As a result, reconstructed values will become less trustable in planes far away from the midplane. Variations of FDK such as P-FDK (Turbell et al. 1999) and T-FDK (Grass et al. 2000) were proposed to reduce these cone-beam artifacts. These variations are different in the way of the rebinning and/or filtering directions on the measured data are defined.

Now circular cone-beam FDK can be readily extended to helical cone-beam FDK or even a general FDK for any given geometry. We denote the helical source trajectory as $(-R\sin\beta, R\cos\beta, l_p\beta/2\pi)$ in the coordinate system, where $l_p$ is the helical pitch (see Fig. 3.5). A helical FDK algorithm can be derived based on Eq. 3.19:

$$f(x,y,z) = \int\limits_{\beta_z-\pi}^{\beta_z+\pi} \frac{R^2}{(x+R\sin\beta)^2 + (y-R\cos\beta)^2 + (z-v)^2} \int\limits_{-\Delta\gamma/2}^{\Delta\gamma/2}$$

$$\{(\cos k \cos\gamma\, p(\beta,\gamma,v)) \otimes g(\gamma)\} d\gamma d\beta \qquad (3.20)$$

$$\text{where}\ \ v = \frac{(z - l_p\beta/2\pi)R}{\sqrt{(x+R\sin\beta)^2 + (x-R\cos\beta)^2}}$$

where $\beta_z$ is the current view angle, $v$ is now view-dependent due to the axial movement of the source. Comparing Eq. 3.20 with Eq. 3.19, it is almost the same except that the preweighting, filtering and backprojection are all performed with respect to the helix. The outer integration range is $2\pi$, which means that for each view only information within that range is used for reconstruction. In fact, if we project a trajectory segment over $2\pi$ onto the detector, the projected region coincides with the region inside the Tam-Danielsson window (Fig. 3.5).

Note that above derivations are only for the data acquired with a 3D cylindrical detector. Another common detector shape is planar. For example, the circular cone-beam FDK algorithm for this configuration is quite similar to Eq. 3.19, except no modification on the ramp filtering. Details about how to derive the planar detector FDK algorithm for (both circular and helical) cone-beam data can be found in (Turbell 2001).

### 3.3.4   3D exact reconstruction

Let us assume that the data-sufficiency condition is satisfied for the measured data. Rather than using an approximate algorithm (e.g. for a helical cone-beam geometry), a completely different strategy is to derive an exact reconstruction algorithm to reconstruct the image. Such an algorithm is guaranteed to provide the "exact" inverse of the operator that models the acquisition process. Three types of 3D exact reconstruction algorithms will be briefly reviewed in this section, including Grangeat's equation, Katsevich's approach and backprojection filtering.

In 2D parallel-beam geometry, the Fourier slice theorem describes the relationship between the measured data and the object, which provides the theoretical support for the exact reconstruction. Likewise in 3D cone-beam geometry, Grangeat (1991) derived ***Grangeat's equation*** which describes a relationship between the cone-beam data (a subset of the X-ray transform) and the 3D Radon transform of the object. With such a relationship, reconstructing a 3D object exactly is possible and requires two steps: (1) compute the derivatives of measured data; (2) reconstruct the image by applying 3D inverse Radon transform to the derivatives. Grangeat's equation was proved to be able to

reconstruct the data acquired from many source trajectories (Caroline et al. 1994; Defrise et al. 1994). As a type of direct Fourier reconstruction algorithms, computation complexity of Grangeat's equation is often very high for a realistic problem.

***Katsevich's approach*** (Katsevich 2002) is a general reconstruction approach for data acquired along many source trajectories. This algorithm is a type of FBP algorithm and of which the implementation is considered to be more efficient than the implementation of Grangeat's algorithm. Here let us consider the helical cone-beam geometry in Fig. 3.5 and recall the definition of the Pi-line and Tam-Danielsson window. The implementation of Katsevich's algorithm consists of four steps in such a geometry (Noo et al. 2003): (1) compute the derivatives of measured data with respect to the rotation angle; (2) for each voxel, find the corresponding Pi-line and determine the backprojection integration range over the rotation angle; (3) for each projection, perform 1D Hilbert filtering along the predefined direction on the detector; (4) perform backprojection with the distance weighting.

Zou et al. (2004) proposed an exact reconstruction algorithm ***backprojection filtering*** (BPF). Unlike Katsevich's approach, BPF performs the filtering after the backprojection (for example for a helical cone-beam scan, 1D Hilbert transforms are performed along Pi-line in the image domain, after differential cone-beam data are backprojected). In contrast, for a FBP-type algorithm, filtering is always performed before the backprojection step. BPF has the advantage that is capable of dealing with cone-beam data with a certain amount of truncation. Hence it is often used for the exact reconstruction in region-of-interest (ROI) scans (Courdurier et al. 2008; Defrise et al. 2006; Ye et al. 2007).

In a real scan, it is often preferred to reconstruct an image using an approximate algorithm (e.g. FDK), rather than an exact one (e.g. BPF). There are mainly four reasons for this preference: (1) mathematical exactness is difficult to be implemented for an exact algorithm due to the discretized representation of the image model; (2) an approximate algorithm may produce comparable or even better image quality, especially when measured data are insufficient or noise-contaminated; (3) some approximate algorithms are able to use all the data (e.g. in a helical scan), while the exact one cannot; (4) an approximate algorithm is often computationally efficient and easily to be implemented for various geometries. In contrast, a new design of an imaging geometry may require a new associated exact reconstruction algorithm.

## 3.4 Iterative reconstruction

After introducing the analytical reconstruction algorithms, we will introduce several iterative reconstruction algorithms in this section. Many iterative algorithms have been proposed for the purpose of tomographic reconstruction.

From an optimization theory point-of-view, iterative reconstruction is essentially an unconstrained optimization process. It aims at searching an estimated object that minimizes the inconsistency between the measured data and the projections computed from that estimated object. Types of iterative reconstruction algorithms differ in choice of cost function and/or optimization strategies. A flowchart describing how an iterative algorithm works is shown in Fig. 3.11a.

The fundamental differences between the analytical and iterative algorithm were discussed in the beginning of the Section 3.3. In contrast to an analytical algorithm, an iterative algorithm has the advantages of:

(1) Better handling the discretized image model by representing both object and sinogram in discretization. This allows application of numerical approaches to solve the reconstruction.

(2) Enabling more complex physical models of the measurement process. For example when the noise is high in the measured data, the reconstruction suffers from significant noise propagation. Incorporating the appropriate noise model to an analytical inversion can be very complicated. On the other hand, iterative reconstruction algorithms can be developed which are based on an accurate statistical model for the data noise.

(3) Including prior information to force the estimated object close to a solution with desired properties. In this case, the reconstruction then becomes a constrained optimization process. For example if the prior knowledge is "the object is piecewise constant", iterative reconstruction will balance the minimization of the data inconsistency and the prior information to achieve an overall noise-suppressed solution.

In this section, we will briefly review three common iterative reconstruction algorithms in CT imaging.

### 3.4.1   Algebraic reconstruction technique

A popular iterative reconstruction algorithm is **algebraic reconstruction technique** (ART), which is adapted from the original Kaczmarz's method for solving an overdetermined problem (Chong et al. 2011):

$$A\mu = l \tag{3.21}$$

where $l$ are the observed data, $\mu$ contains the variables to be estimated and $A$ is the system matrix mapping $\mu$ to $l$. From an optimization theory point-of-view, ART can be viewed as a special case of the Projection onto Convex sets (POCS) method for finding solutions of a system of equations (Bauschke et al. 1996; Escalante et al. 2011). The first application of ART on tomography is
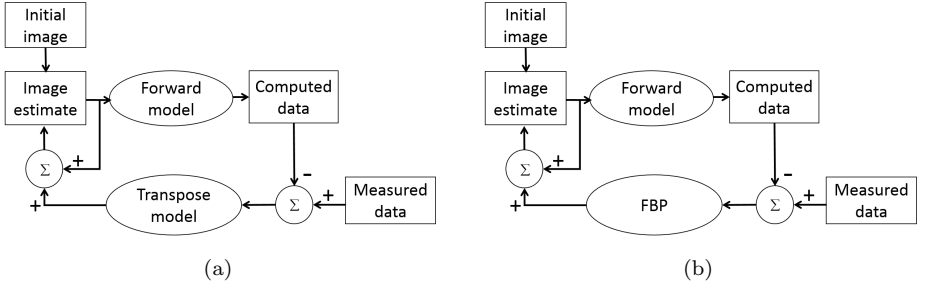
Figure 3.11: (a) The flowchart of a typical iterative reconstruction algorithm. Image estimate goes through forward model and the residual errors in projection domain are back-propagated via the transpose of the forward model. (b) A variation of (a) which replaces the transpose model with an analytical reconstruction (e.g. FBP). The algorithm in (b) is often referred as Iterative FBP (Sunnegårdh et al. 2008) and the details are not covered in this thesis.

proposed by Gordon et al. (1970). The basic idea in that work is to solve a set of linear equations by finding the estimate that satisfies all the constraints (equations). The image is updated sequentially according to each measured ray, which is considered as a constraint to the solution and the updates over rays can be repeated for several iterations. Later Gilbert proposed to update the image based on all measured rays in all views simultaneously, instead of updating only based on individual rays (Gilbert 1972). The resulting algorithm is simultaneous image reconstruction technique (SIRT). Another variant of ART is simultaneous algebraic reconstruction technique (SART) (Andersen et al. 1984), which updates the image at every time based on all rays in one individual view. The update equation for ART (and its related algorithms) is:

$$
\mu_j^{k+1} = \mu_j^k + \alpha_j \cdot \frac{\sum\limits_{i \in \Omega} a_{ij} \frac{l_i - \hat{l}_i}{\sum\limits_{j} a_{ij}}}{\sum\limits_{i \in \Omega} a_{ij}}
$$

$$
\text{where } \hat{l}_i = \sum_{j=1}^{J} a_{ij} \mu_j = \ln \left( \frac{b_i}{\hat{y}_i} \right)
$$

(3.22)

$b_i$ is the measured value of ray $i$ in the blank scan, $\hat{y}_i$ are the expected data computed from projections of the estimated object, $k$ is the iteration number, $\alpha_j$ is the relaxation factor, $i$ is the ray index, $j$ is the voxel index and $a_{ij}$ indicates the intersection of the ray $i$ through the voxel $j$. SIRT and SART differ in the summation range in both numerator and denominator in Eq. 3.22. When $\Omega$ is the whole set (all rays from all projections), above equation is the

update equation of SIRT; when $\Omega$ is a subset containing all rays from one view, above equation is the update equation of SART. SART usually converges faster than SIRT but may end into a limit cycle. So for SART the relaxation factor alpha is often set to a value larger than 0 less than 1.

In transmission tomography, ART, SART or SIRT are often referred as a post-log algorithms, because they are applied to the data after the log-conversion (Eq. 3.22). Drawback of applying ART in tomography is that it does not work well for noisy measurements. ART is designed to solve a set of linear equations, which does not account for the noise characteristics of the measured data well. As explained in (Natterer 2001), ART will converge to the minimum norm solution if the data are consistent. However, it will converge to a weighted least square solution if data are inconsistent. Hence an ART reconstruction could be very sensitive to the perturbation (e.g. noise) in a scan.

## 3.4.2 Maximum likelihood algorithm

Rather than finding the solution in an algebraic way, an alternative way is to construct a cost function which accounts for noise characteristics explicitly and optimize it. Here $y$ is the measurement, $\hat{y}$ is the expectation based on $\mu$, i.e. a noise-free simulation of the CT assuming that $\mu$ was the object being scanned. A statistical model describes the object function of $\mu$ as a function of the measured data $y$. The aim is to find the distribution $\mu$ that maximizes the probability $P(\mu|y)$. According to Bayes rule, we express such probability to be maximized as:

$$P(\mu|y) = \frac{P(y|\mu) \cdot P(\mu)}{P(y)} \tag{3.23}$$

where $P(\mu)$ contains the prior information and $P(y)$ is independent from $\mu$. If we assume no prior information is available, the problem reduces to the maximization of $P(y|\mu)$. For a monochromatic transmission scan, we link the expected value $\hat{y}$ to the attenuation $\mu$ via a discretized version of Beer-Lambert's law (Eq. 2.3):

$$\hat{y} = b_i \cdot \exp(-\sum_{j=1}^{J} a_{ij}\mu_j) \tag{3.24}$$

where $b_i$ is the measured value of ray $i$ in the blank scan. In an ideal photon-counting scan, it is safe to assume each of photons Poisson-distributed. Since all measured photons are independent from each other, the probability in Eq. 3.23 turns to:

$$P(y|\mu) = P(y|\hat{y}) = \prod_{i=1}^{l} P(y_i|\hat{y}_i) = \prod_{i}^{l} \frac{\hat{y}_i^{y_i} e^{-\hat{y}_i}}{y_i!} \tag{3.25}$$

Maximizing above probability is equivalent to maximizing the logarithm of it, which is called log-likelihood hereafter (ignoring the constant):

$$L(\mu) = \ln\left(P(y|\hat{y})\right) = \sum_{i=1}^{I} \left(y_i \cdot \ln \hat{y}_i - \hat{y}_i\right) \tag{3.26}$$

Many algorithms optimizing the above function exist, and they are often referred to as ***Maximum Likelihood Algorithms*** for transmission tomography. For example, maximum likelihood transmission reconstruction (MLTR) applies a gradient descent algorithm to maximize the above function (Nuyts et al. 1998; Van Slambrouck et al. 2012). The update equation of MLTR is:

$$\Delta\mu_j = \frac{\sum\limits_{i} a_{ij}(\hat{y}_i - y_i)}{\sum\limits_{i} a_{ij}(\sum\limits_{h} a_{ih})\hat{y}_i} \tag{3.27}$$

When prior information is available, the log-posterior function to be maximized can be derived from Eq. 3.23:

$$\Phi(\mu) = L(\mu) + \lambda R(\mu) \tag{3.28}$$

where $R(\mu)$ is log-prior, $\lambda$ is the prior weight. Maximum a posteriori reconstruction for transmission tomography (MAPTR) is the associated reconstruction algorithm for above function. For a convex prior, its update equation can be derived as (Michielsen et al. 2015):

$$\Delta\mu_j = \frac{\sum\limits_{i} a_{ij}(\hat{y}_i - y_i) + \lambda\frac{\partial S(\mu)}{\partial \mu_j}\big|_{\mu=\mu_{old}}}{\sum\limits_{i} a_{ij}(\sum\limits_{h} a_{ih})\hat{y}_i - \lambda\frac{\partial^2 S(\mu)}{\partial \mu_j^2}\big|_{\mu=\mu_{old}}} \tag{3.29}$$

where $S(\mu)$ is the separable surrogate function of $R(\mu)$. A similar derivation for Eq. 3.27 was proposed by introducing a separable quadratic surrogate for the likelihood function (Erdogan et al. 1999a; Fessler et al. 1997). Note that another similar algorithm was derived as Convex algorithm for transmission

scan, which behaves differently in convergence (Beekman et al. 2001; Lange et al. 1995).

These update equations require the knowledge of both transmission and blank scans. Unfortunately they are not always available from a clinical CT scanner. In such a case only the data after log-conversion are available:

$$l_i = \ln\left(\frac{b_i}{y_i}\right) \tag{3.30}$$

If we incorrectly assume that each integral is Poisson-distributed, similar to Eq. 3.26 we arrive at a log-likelihood function of $l_i$ instead of $y_i$:

$$L(\mu) = \sum_{i=1}^{I}\left(l_i \cdot \ln \hat{l}_i - \hat{l}_i\right) = \sum_{i=1}^{I}\left(l_i \cdot \ln \sum_{j=1}^{J} a_{ij}\mu_j - \sum_{j=1}^{J} a_{ij}\mu_j\right) \tag{3.31}$$

where $\hat{l}_i$ is the expected line integral at $i$. Here we assume there is no prior information available. Aiming at maximizing the above log-likelihood function, an update equation of $\mu$ can be derived with classical 2-step Expectation Maximization algorithm (Borman 2009):

$$\Delta\mu_j = \frac{\mu_j \sum_i a_{ij}\frac{l_i - \hat{l}_i}{\hat{l}_i}}{\sum_i a_{ij}\frac{1}{\hat{l}_i}\sum_h a_{ih}\mu_h} \tag{3.32}$$

Above is the update equation of the maximum likelihood expectation maximization (MLEM) algorithm (Lange et al. 1984; Shepp et al. 1982). It is appropriate for emission data, because measured activity data can be accurately modelled as Poisson-distributed, and MLEM is often considered to be the routine reconstruction algorithm in emission tomography. For transmission tomography, MLEM is often referred to as a post-log algorithm, as the available data are after the log-conversion. On the other hand MLTR is a pre-log algorithm, which requires both transmission and blank scans are available.

### 3.4.3 Weighted least squares algorithm

Recall that for a transmission scan, MLTR assumes that the measured data satisfy the Poisson distribution, while MLEM incorrectly assumes log-converted data to be Poisson-distributed. Some researchers proposed to use a Gaussian distribution to model the log converted data. Again assuming no prior information is available, the probability in Eq. 3.23 to be maximized is:

$$P(l|\mu) = P(l|\hat{l}) = \prod_{i=1}^{I} P(l_i|\hat{l}_i) = \prod_{i=1}^{I} \frac{1}{\sigma_i \sqrt{2\pi}} \exp\left(-\frac{\left(l_i - \hat{l}_i\right)^2}{2\sigma_i^2}\right) \qquad (3.33)$$

where $\sigma$ is the standard deviation. We can obtain the log-likelihood by taking the logarithm of above probability and ignore the constant term:

$$L(\mu) = -\sum_{i=1}^{I} \frac{1}{2\sigma_i^2} \left(l_i - \hat{l}_i\right)^2 = -\sum_{i=1}^{I} \frac{1}{2\sigma_i^2} \left(l_i - \sum_{j=1}^{J} a_{ij}\mu_j\right)^2 \qquad (3.34)$$

The associated reconstruction algorithm for above log-likelihood function is often referred to as **weighted Least Squares** (WLS) algorithm. From Eq. 3.23, we can incorporate prior information to form a log-posterior $\Phi(\mu)$ and the associated optimization algorithm is the penalized weighted least squares algorithm (PWLS):

$$\Phi(\mu) = -L(\mu) + \lambda R(\mu) \qquad (3.35)$$

Note that here we have a minimization problem rather than a maximization problem. So the prior has to be multiplied with $-1$ to become a penalty in above equation. If the prior is convex, the posterior must be convex since the likelihood function is quadratic. Fessler (1994) and Sauer et al. (1993) applied Gauss-Seidel algorithm to optimize the above log-posterior function, during which the image is updated on a voxel-by-voxel basis. A different strategy is to introduce a separable quadratic surrogate approach (Elbakri et al. 2002; Erdogan et al. 1999b), during which all voxels are updated simultaneously. In (Elbakri et al. 2002), the following update equation for the attenuation is obtained by maximizing the surrogate function at every iteration:

$$\Delta\mu_j = \frac{\sum_{i=1}^{I} a_{ij} w_i \left(\sum_{j=1}^{J} a_{ij}\mu_j - l_i\right) + \lambda \frac{\partial S(\mu)}{\partial \mu_j}\big|_{\mu=\mu_{old}}}{\sum_{i=1}^{I} a_{ij} w_i (\sum_{j=1}^{J} a_{ij}) + \lambda \frac{\partial^2 S(\mu)}{\partial \mu_j^2}\big|_{\mu=\mu_{old}}} \qquad (3.36)$$

where $S(\mu)$ is the separable surrogate function of the prior, $w_i = 1/\sigma_i^2$, denotes the inverse of the local variance in the transmission scan. The interpretation of the weighting factor $w_i$ is straightforward - it reduces the weighting associated with low photon counts, hence reducing the possibility of artifacts.

### 3.4.4   Discussion of iterative reconstruction algorithms

Both maximum likelihood and weighted least squares algorithms assume a simple statistical model, either Poisson or Gaussian. When using an integrating detector (Section 2.2), this is merely an approximation to the complex random processes. Several mixture models are proposed to better model the complex statistics. Snyder et al. (1993) and Ma et al. (2012) proposed to use a "Poisson+Gaussian" model to account for Gaussian-like electronic noise. Whiting (2002) and Elbakri et al. (2003) proposed to use a "compound Poisson" model to model the statistics at several distinct energy levels. An even more accurate modelling would involve Monte Carlo simulations (Jan et al. 2011).

When using a post-log algorithm to reconstruct a real transmission dataset (like using SART or FBP), in theory one shouldn't assume noise-free data. Simply treating the log-converted line integrals as Poisson-distributed (using MLEM) is also suboptimal (as the new distribution of the converted data is not Poisson anymore). Nevertheless, post-log algorithms like MLEM, SART or even FBP often produce acceptable reconstruction when the noise level is low in measured data. In contrast, another post-log algorithm WLS works well even when noise is high in the data. The reason is that it includes some statistical weighting strategy during the reconstruction, which has the same effect as modelling a statistical model in a pre-log algorithm. A detailed comparison between pre-log and post-log algorithms can be found in (Fu et al. 2017).

Algebraic reconstruction, maximum likelihood and weighted least squares algorithms can all be interpreted as a general gradient decent optimization method, of which the update equation is:

$$\mu^{k+1} = \mu^k - \alpha \nabla f(\mu^k) \tag{3.37}$$

where $f$ is the cost function, $k$ is the iteration number, $\alpha$ is the step size, $\nabla f$ is the first derivative of the cost function at $x^k$.

## 3.5   Accelerating iterative reconstruction

Although widely used in nuclear medicine, iterative reconstruction has only been receiving more attention recently in CT imaging and was only implemented a few years ago in some of the vendor software packages, e.g. Veo from GE and iMR from Philips. Iterative reconstruction is promising for applications to low dose CT-scan (Sidky et al. 2008) and artifact reduction (De Man et al. 2001). However, one major concern is the relatively long computation time, due to the frequent forward and backprojection operations. When prior information is available, the additional calculation may further increase the

computation time. There is a general interest in accelerating the iterative reconstruction to facilitate the acceptance in clinical routine. In this section, we will introduce several approaches to accelerate an iterative reconstruction algorithm. These approaches are general, meaning that they can be combined with most iterative algorithms. More complicated acceleration techniques aim at choosing advanced optimization methods for the cost function, especially with the prior information (Chun et al. 2014; Nien et al. 2015; Ramani et al. 2012). These techniques are beyond the scope of this thesis.

### 3.5.1   Ordered subsets and block iterative algorithm

An iterative reconstruction can be accelerated by applying sequential updates for different subsets of the measured data. Hudson et al. (1994) first proposed such a technique for MLEM reconstruction, resulting in OSEM algorithm for emission tomography. Later this technique was introduced to the reconstruction of the transmission data, resulting in algorithms like OS-MLTR (Nuyts et al. 1998), OSTR (Erdogan et al. 1999a), OS-PWLS (Erdogan et al. 1999b) and OS-SIRT (Wang et al. 2004). To obtain a good convergence rate, such an update requires any projection view within one subset should be as far away as possible from others in the same subset - obviously any neighboring views or opposite views should be avoided in a single subset. For the same reason, it is better to make the angular distance between the views in subsequent subsets as large as possible. Because of the predefined order used to group the projections, this technique is called ***ordered subsets*** acceleration. One problem when using the ordered subsets acceleration in reconstruction is that the algorithm converges to a limit cycle. The reason is that ordered subsets reconstruction algorithm is essentially a stochastic gradient optimization algorithm which approximates the full gradient with sub-gradients from all subsets. The variance introduced by such approximation is no longer negligible when a large number of subsets are used. Hence a too large number of subsets is not preferable in an iterative reconstruction, unless relaxation is applied in later iterations (e.g. in SART) or a descending numbers of subsets is applied as the iteration number increases (Ahn et al. 2003, 2006; De Pierro et al. 2001; Kole 2005).

As an alternative of the ordered subsets technique, the ***block iterative coordinate descent*** (B-ICD) update algorithm was proposed to accelerate an iterative reconstruction. Unlike in ordered subsets acceleration where the measured data are divided in subsets, in this approach the volume is divided into blocks. The divided blocks are updated sequentially in a predefined order - again arranged such that the neighboring blocks are as far away from each other as possible. B-ICD was integrated into SART (Byrne 2005), PWLS (Benson et al. 2010), MLTR and MLEM (Van Slambrouck et al. 2014). A special case of Benson et al. (2010) is when the size of a single block reduces to single voxel, the algorithm then becomes the iterative coordinate descent algorithm (ICD) (Sauer et al. 1993). Note that when a block only contains one (e.g. in ICD)

or few voxels, a special design of the projector is often needed for efficient reconstruction (Fessler et al. 2011; Van Slambrouck et al. 2014). A downside of B-ICD is the unbalanced convergence rates in different blocks. Hence it is often suggested to start the reconstruction from an initial image obtained from an analytical reconstruction. One may wonder about the possibility to combine ordered subsets and B-ICD techniques. It is often true that such a combination can further accelerate the iterative reconstruction. However, one needs to carefully avoid making reconstruction converge to in a limit cycle or even obtaining a diverged solution, due to the fact that ordered subsets approach is not guaranteed to achieve convergence, as discussed in the last paragraph.

## 3.5.2  First order momentum

As mentioned at the end of Section 3.4, the iterative reconstruction algorithms introduced in this thesis can be viewed as "simple" gradient descent algorithms, which are known to have a slow convergence rate considering the existence of advanced optimization methods. First order momentum is a common method to solve an unconstrained optimization problem. It requires to calculate the first derivatives (Jacobian) of the cost function - such as conjugate gradient descent and other gradient descent algorithms. Second order methods require to calculate the second derivatives (Hessian), an example being Newton's method. Superior convergence rate can be achieved over the "simple" gradient descent algorithm when using some of the first order and second order approaches. However a careful selection on searching directions and step sizes is often required during the optimization.

Momentum methods are a type of first order method thst can accelerate the reconstruction significantly and can easily be applied on top of "simple" gradient descent methods. The classical momentum works in a way to "accumulate a velocity vector in directions of persistent improvement in the cost function" (Sutskever et al. 2013). Let us apply the classical momentum approach to the general update equation of a tomographic image reconstruction:

$$\mu^{k+1} = \mu^k - \alpha \nabla f(\mu^k) + v(\mu^k - \mu^{k-1}) \tag{3.38}$$

where $\alpha$ is the step size, $v$ is the velocity rate, $\mu^k$ is the current image estimate and $\mu^{k-1}$ is the previous one, $\nabla f$ is the first derivative of the cost function at $x^k$. It can be seen that when $v$ equals to zero, the momentum method reduces to the standard gradient descent algorithm (Eq. 3.37).

As a momentum method, **_Nesterov's method_** is proved to have good convergence rate for convex optimization (Nesterov 1983). It differs from the classical momentum method in two aspects: (1) Nesterov's method gives formulas for the step size and velocity rate, whiles the standard method does not. (2) Nesterov's method calculates the gradient after applying the velocity, while

standard momentum methods calculate the gradient before applying the velocity. With suggested parameters in (Beck et al. 2009), Nesterov's approach can be applied on top of an (ordered subsets) iterative reconstruction algorithm as follows:

> For each itertation
> For each subset
> $\quad$ iter $0$ : choose $\mu^0$, set $\rho^0 = \mu^0$, $t^0 = 1$
> $\quad$ iter $k$ : $\mu^k = \rho^k - \frac{1}{L}\nabla f(\rho^k)$ $\qquad$ ; $update\ \mu$
> $\qquad$ $t^{k+1} = \left(1 + \sqrt{1 + 4(t^k)^2}\right)/2$
> $\qquad$ $\rho^{k+1} = \mu^k + \frac{t^k-1}{t^{k+1}}(\mu^k - \mu^{k-1})$ $\qquad$ ; $apply\ momentum$
> Endfor
> stop until convergence
> Endfor

where $\rho$ is an auxiliary variable and $L$ is the Lipschitz constant. Above algorithm uses two previous updates ($\mu^k$, $\mu^{k-1}$) to calculate the momentum. Nesterov (2005) proposed a momentum method using all previous updates to further improve the stability and convergence rate of the optimization.

It is often still slow to solely apply Nesterov's method in CT reconstruction, due to the large number of parameters to be estimated. Kim et al. (2015a) proposed to combine Nesterov's method with the ordered subsets technique. However, a combination can magnify the accumulated variances from an ordered subsets reconstruction algorithm. To reduce the instability introduced by variances, Kim et al. (2015a) proposed to apply relaxations on both velocity $v$ and step size $\alpha$ in Eq. 3.38. As an alternative approach inspired by (Johnson et al. 2013), Zhou et al. (2017) proposed to include a correction step after every image to update reduces the variances. Both approaches were proved to allow the usage of large number of subsets in CT reconstruction, while combined with the momentum approach.

### 3.5.3 Parallel computing

Rather than modifying the algorithm itself, another approach to accelerate an iterative reconstruction is running the computational intensive operations on multiple-core CPU/GPU(s). Repetitive forward and backprojection often are the bottleneck in an iterative reconstruction process. Both forward and backprojection are parallelizable. In principle, forward and backprojection operations can be performed either in voxel-driven or ray-driven manner. For instance, a ray-driven forward projection loops through all rays and for each ray, reads and sums the voxels contributing to that ray; a voxel-driven forward projection loops through all voxels and for each voxel, updates the voxel by receiving contributions from all passing rays.

In sequential computing, e.g. on a single thread CPU, the computation burden of ray-driven and voxel-driven forward and backprojection are very similar. But in **parallel computing**, the computation time associated with a voxel-driven or ray-driven implementation can be very different due to "racing", i.e. multiple writes to one address in memory at the same time. Although modern parallel computing languages (e.g. CUDA or OpenCL) have a built-in atomic function to handle such conflicts, this comes at the cost of additional calculation times (because of introduction of the scheduling scheme). Hence for forward projection, it is preferred to use the ray-driven manner to avoid the racing on ray updates. For the same reason for backprojection, it is preferred to use the voxel-driven manner to avoid the racing on voxel updates. In practice, such preferences are inconvenient, since it is much easier to ensure that backprojection is the exact adjoint of the forward projection, i.e. both are ray-driven or both are voxel-driven).

Additional attention should be paid when performing parallel computing on a GPU - one needs to maintain all pipelines busy to hide the latency of context switching between the CPU and GPU. This requires transferring the data to GPU infrequently hence reducing overall transferring time. For this reason an ordered subsets reconstruction could be ineffective when only forward and backprojection are performed on GPU. One can imagine when a large number of subsets are used, context switching time cannot be hidden anymore (Maaß et al. 2011; Xu et al. 2010). To maximize the overall efficiency, a trade-off between the acceleration from ordered subsets and the acceleration from parallelization needs to be found. One way is to select a proper number of subsets which results in an overall acceleration, while the selection depends on data size and hardware features. Another way is to let the whole iterative algorithm run on GPU, rather than just forward and backward projection operations (Fig. 3.12) (Keck 2014). In such a way no context switching between CPU and GPU is required. However, prototyping an iterative reconstruction algorithm may be not easy on GPU. Note that parallel computing on CPU suffers less from the above issue, since transferring memory from CPU to RAM is much cheaper than from CPU to GPU.
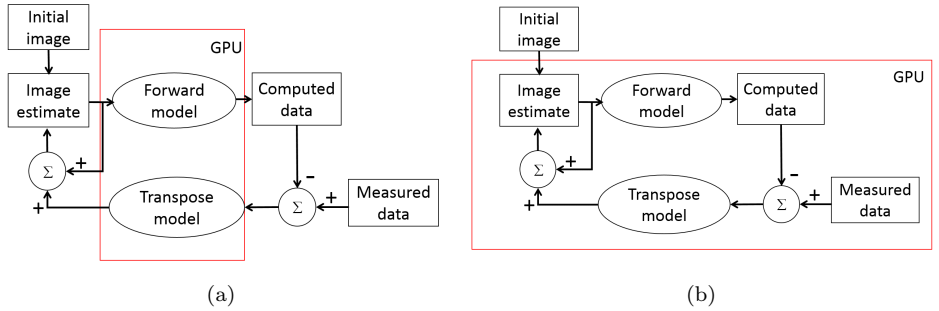
Figure 3.12: Different strategies to implement an iterative reconstruction algorithm on GPU: (a) only running forward and backward projections on GPU, and rest of the program on CPU. (b) running the whole algorithm on GPU.

# Chapter 4

# Motion artifact reduction

In CT Imaging, artifacts can be defined as the discrepancy between the estimated object and the real attenuation representation of that object. The artifacts can appear as a pattern of rings, cupping, streaks, shading and blurring, etc. Most artifacts arise from inaccuracies in the models used to represent the image, the physics and/or the geometry. One typical image model error originates from the discretized representation of the continuous object and rays. Physical model errors result from the inaccurate models of the physical processes that contribute to CT imaging, including noise, beam hardening, scatter and movement, etc. Geometrical model error refers to the failure of calibration of the mechanical alignment of the detector and/or source positions. If any of above factors are not addressed properly during reconstruction, the resulting image can be difficult to interpret. A review on various artifacts in CT imaging can be found in (Barrett et al. 2004). Numerous methods were proposed to eliminate or reduce each type of image artifacts. All these methods are either based on image processing techniques or on the design of more accurate reconstruction models (Nuyts et al. 2013).

Voluntary and involuntary patient motion are very common causes of image artifacts in CT imaging. Patient motion can be categorized into either rigid motion (head and extremities) or non-rigid motion (heart, lung and other internal organs). In CT imaging, we can assume that the motion during the acquisition of a single view is negligible, because of the high sampling rate. Except for some dedicated respiratory or cardiac procedure, the reconstruction applied in clinical CT imaging assume that there is no patient or organ movement during the scan. Therefore, any motion would break the data-consistency and induce artifacts in the reconstructed image. Motion correction is of general interest in research and clinical fields. In this section, we will review several techniques that eliminate or reduce the motion artifacts. Motion correction methods are divided into two categories in this Chapter. The first group requires the motion information, and consists of motion acquisition and motion compensation

processes. Motion acquisition derives the motion from reference images, surrogate signals or from the data themselves. Motion compensation compensates the artifacts during a reconstruction process. The second group corrects the motion artifacts using ways of image-processing techniques, without knowing the motion information.

# 4.1 Methods requiring motion information

When motion is known or can be derived, motion compensated reconstruction can compensate that motion. In this section, we will first introduce the ways to derive the motion. Then we will introduce the ways to compensate the motion in a reconstruction. In the end, we will introduce a joint estimation method that estimates and compensates the motion alternately in an iterative scheme.

## 4.1.1 Motion acquisition

### Deriving motion from reference images

Sometimes motion-free prior scans of the same patient are already available before the motion correction for the current scan. Some researchers investigated the possibility to estimate the motion with the prior scans (Gendrin et al. 2012; Markelj et al. 2012). This is based on the fact that a set of motion-free projections should match the reprojections of the reconstruction image from a prior scan, which is considered to be a *reference image*. In each view, 2D/3D registration can estimate the motion of the reference volume that fits best to the motion-contaminated projections. Both rigid and non-rigid motion across views can be determined in such way. Furthermore, the estimated motion can be refined in an iterative manner by repeating above 2D/3D registration process at each projection view.

### Deriving motion with external and internal tracking

Unfortunately prior scans are not always available. Then rigid motion of head or extremities, or surrogate signals of some periodic internal organ motion can be measured with the help of dedicated external devices. These devices work with mechanical, acoustic, magnetic or optical tracking techniques, and are often commercially available. Such measurement is often referred to as *external tracking*. External tracking was proven to be able to measure the rigid motion. Kim et al. (2015b) applied a marker-based optical tracking system to monitor the movement of the patient head during helical CT scans. Markerless optical tracking techniques have been also applied in tracking head movement in positron emission tomography (PET) and CT scans (Bier et al. 2017; Kyme

et al. 2014). For the non-rigid motion of the internal organs, external tracking can only provide surrogate signals but not the actual motion. Cardiac and respiratory surrogate signals are measured with the help of dedicated devices in diagnostic imaging, image-guided surgery, and radiation therapy (Desjardins et al. 2004; Hugo et al. 2012).

Fiducial markers are sometimes used to track the movement of internal organs, this technique is referred to as ***internal tracking***. Internal tracking is commonly used in radiotherapy, during which the accurate beam delivery is crucial. Before the therapy, fiducial markers are implanted close to the tumor, allowing real-time tracking of the tumor movement in simultaneously acquired fluoroscopy (2D projections) during the therapy (Keall et al. 2004; Shirato et al. 2003). In diagnostic imaging, applications of fiducial markers have also been investigated in extremity imaging. Choi et al. (2013, 2014) used implanted markers to estimate the knee motion in weight-bearing imaging. In that work the rigid pose in each projection was estimated by minimizing the difference between the expected and measured locations of the markers in projections. Non-rigid movement can also be estimated based on projections by identifying the locations of multiple markers in the projections. Rene (2010) assumed little lung movement within one scanner rotation and estimated 2D motion fields for each projection within that rotation. Then a 3D motion field relative to a reference pose was derived from that set of estimated 2D fields. Sometimes when fiducial markers are not available, high intensity structures (e.g. bones) are used as virtual fiducial markers in projections, since the movement of the high intensity structures contributes the most to the estimation of the deformation in projections.

**Deriving motion from the data**

When neither tracking data nor prior scans are available, motion acquisition has to rely on the measurement data only and is often more challenging. In such cases, the acquisition of the motion essentially is a motion estimation process. One data-driven approach is based on ***motion artifact metrics***, which are defined as image features that are sensitive to the motion artifacts, e.g. entropy, sharpness, gradients. The rigid or non-rigid motion in each projection view can be estimated by minimizing these metrics from a motion-corrupted image. Rohkohl et al. (2013) and Hahn et al. (2017) estimated the non-rigid motion by minimizing the image entropy within a cardiac ROI. Promising results on motion reconstruction of coronary arteries were reported in those studies. Sisniega et al. (2017) compared different artifacts metrics when estimating the rigid motion in weight-bearing imaging. That work suggested that gradient-based metrics gave overall the best performance in motion estimation for high resolution cone-beam CT scans. However, it is questionable how well a motion artifact metric method would work for severe motion estimation, as optimizing a certain metric might lead motion estimate to a local minima.

Another data-driven motion estimation approach is based on ***data-consistency***. In a CT-scan, data-consistency describes the data redundancy from the multiple scanning positions of the same object. When motion occurs, the consistency conditions would no longer be satisfied in the measured data. Because of that, one can estimate the motion by forcing the data to satisfy the consistency conditions. The Helgason-Ludwig consistency condition (HLCC) (Ludwig 1966; Sigurdur 1999) is a condition describing the relationship between the Radon transform of parallel projections and the imaged object. For instance in parallel-beam geometry, the zero-order HLCC states that the summation of all projections is a constant independent from the view. HLCC was extended into fan-beam (Leng et al. 2007; Yu et al. 2007, 2006) and cone-beam (Clackdoyle et al. 2013, 2016) geometries, and showed promising results when applied to motion estimation. Other consistency conditions can also be used for motion estimation, e.g. Fourier consistency condition (Berger et al. 2017), Epipolar consistency condition (Aichert et al. 2015) and John's equation-based consistency condition (Levine et al. 2010). However, we observed that most of the above methods were only verified in simulation studies. One possible reason is that all consistency conditions are derived based on ideal assumptions - with continuous image and detector models, no truncation and monochromatic X-ray source, etc. A real scan can cannot match all these assumptions. Hence artifacts from compound sources may affect the accuracy of the motion estimation, as many factors other than motion contribute to the violation of the data-consistency.

## 4.1.2 Motion compensation

### Compensating in an analytical reconstruction algorithm

After motion is acquired, the next step is to reconstruct an image with compensation for that motion. It is possible to perform this in an analytical reconstruction algorithm. In 2D, exact FBP reconstruction with known affine motion is possible for both parallel-beam and fan-beam geometries (Desbat et al. 2007; Roux et al. 2004). In 3D, a generalized BPF algorithm is proposed to exactly reconstruct the non-truncated data measured with an arbitrary source trajectory (Ye et al. 2005), which effectively is a motion-corrected trajectory when motion is present. Due to the complexity of implementation in an exact algorithm, other researchers use approximate algorithms to perform the motion compensation instead. For example in an FDK algorithm, motion is corrected in the backprojection step, ignoring the adjustment of the ramp filtering and weightings. The reconstructed image quality is often acceptable when the motion is small. Schäfer et al. (2006) have shown that when the cardiac motion is known, one can compensate that motion by reconstructing the image in a particular reference pose. This is achieved by changing the intersection position of the ray and the volume during the backprojection step of an FDK algorithm in all views. The effective ray path is a warped version

of the original path - deformed by the non-rigid motion (Fig. 4.1b). Rather than compensating the motion during the backprojection, alternately one could compensating the motion after the backprojection. A straightforward way is to first perform the normal backprojection, then compensating the motion by warping the backprojected image with respect to the known motion field. This approach is commonly-used in 4D CT imaging.

**Compensating in an iterative reconstruction algorithm**

Aside from an analytical algorithm, it is also possible to perform motion compensation in an iterative reconstruction algorithm. Kim et al. (2015b) corrected the rigid motion with respect to an arbitrary coordinate system fixed to the object. They re-oriented the ray paths by transforming the source-detector pairs during both forward and backward projections (Fig. 4.1c). Compared with an FBP-type algorithm, an iterative reconstruction algorithm does not involve ramp-filtering and pre-weighting. This allows compensating larger motions but often with long computation times due to the repetitive nature of the iterative algorithm.

### 4.1.3 Joint motion estimation and compensation

If the motion is known as a priori, then it is relatively straightforward to implement the motion-compensated reconstruction. Another way to correct the artifacts is to perform a joint motion estimation and motion compensation process. Rohkohl et al. (2013) and Hahn et al. (2017) alternately estimated the non-rigid motion in a cardiac ROI and compensated that motion in an FDK reconstruction. The process was repeated for several iterations until a satisfied image was obtained.

## 4.2 Image-processing based methods

When the motion is not known, motion correction can be implemented with an image-processing process, directly targeting artifact-contaminated projections or images. Lu et al. (2002) correct the measured data from a respiratory motion-contaminated scan, under the assumption of a simple motion model. The restored projections can then be reconstructed to an artifact-reduced image. Schretter et al. (2009a) attempted to segment an artifacts-only image, by comparing the forward projections of an initial reconstructed image and the actual measured projections and reconstructing the differential projections. The artifacts-only image can then be subtracted from the initial reconstructed image and above procedure can be repeated several times. Schretter et al. (2009b) and Marchant et al. (2011) tried to register the measured projections to the forward-projections of the initial reconstructed image non-rigidly. The
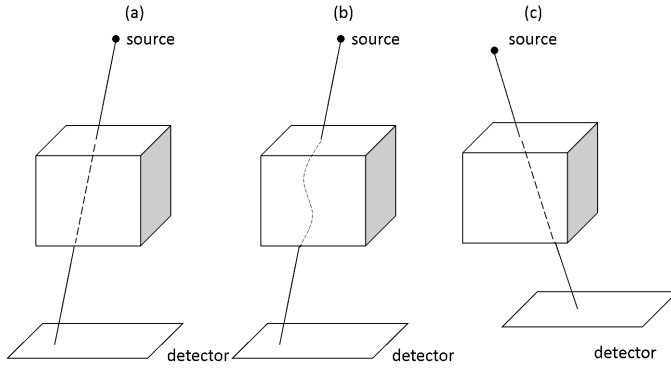
Figure 4.1: (a) Backprojection geometry at one view position. (b) non-rigid motion is compensated by performing the backprojection over a warped ray path deformed by the motion. (c) rigid motion is compensated by performing the backprojection with transformed source-detector pair position.

registered projections were used to generate an initial compensated image and this procedure can be repeated iteratively until a final compensated image was obtained. Other techniques assumed that the periodic movement of a lung tumor or the beating heart only result in blurring on the image (Fang et al. 2013; Nett et al. 2016; Schlueter et al. 1994; Xu et al. 2011). Such blurring can be modelled as a convolution on a motion-free tumour or heart region. The correction performs deconvolution on the region with blurring while keeping other regions unchanged. All above image-processing techniques often produce images with residual artifacts, due to the lack of exact motion information.

# Part II

# Objectives

# Chapter 5

# Objectives

The overall purpose of this thesis is to investigate and mitigate the potential effect of patient head movement on image quality in CT imaging. Specifically, the first objective is to propose a new approach to mitigate the rigid motion artifacts in helical head CT images. Our second objective is to extend this motion artifacts reduction approach to applications in dental cone-beam CT imaging. Sometimes we observed residual artifacts even after compensation based on perfect knowledge of the motion. Those residual artifacts are believed to be mostly due to incomplete measurement. Hence our third objective is to identify the degree of incompleteness of the measurement at voxel level in motion-corrected scans, which can be used to indicate associated artifacts in a reconstructed image.

## An iterative projection-based motion estimation and compensation scheme for head X-ray CT

We aim to perform motion correction for motion-contaminated helical CT scans. We assume the movement in these scans can be modelled as a series of rigid poses across projection views. The proposed approach would only require the measured raw data, without any prior knowledge of motion or reference scans. The proposed approach estimates the motion in an iterative scheme, where the motion and the image are updated alternately. A subsequent high-resolution reconstruction is performed to compensate the last motion estimate. In Chapter 6, we evaluate the proposed approach in simulations, a phantom study and patient studies.

# A motion compensation approach for dental cone-beam region-of-interest imaging

Dental imaging is often performed on dedicated cone-beam CT systems rather than clinical multi-row CT systems. During a scan, cone-beam CT uses a circular trajectory and keeps the targeted structure in the FOV during the entire scan. We aim to investigate a motion correction approach for dental cone-beam CT based on the previous approach. In this study, we assume that we are dealing with the dental scans with rigid motion but not non-rigid motion. Compared with motion correction on a helical CT scan, there are three challenges when correcting a dental scan: (1) a dental scan has a longer duration thus there is a higher probability of patient movement; (2) resolution of a dental scan is often quite high which makes the reconstructed image even sensitive to a slight movement; (3) a dental scan often reduces the irradiated volume by limiting both transaxial and axial FOV. Induced transaxial truncation in data may have negative effects on motion correction performance, whereas clinical CT data only suffer from axial truncation. We proposed modifications to the motion estimation and motion compensation procedures to account for these challenges. In Chapter 7, we evaluate the proposed approach in both simulations and a phantom study.

# Estimation of local data-insufficiency in motion-corrected helical CT

We aim to find a way to determine the local data-insufficiency in a CT-scan. Data-insufficiency problems arise from the fact that (1) interference between patient motion and gantry motion might occur, which causes angular sampling to change and become insufficient; (2) part of the object that should be seen in a particular view moves out of the FOV, because of the patient motion in combination with axial truncation. These effects cause insufficient data and motion correction would not eliminate the artifacts from the data insufficiency. Currently there is no general theory to assess data-sufficiency for tomographic acquisition with truncated views, as is always the case in a helical CT scan. All motion involved in this study are rigid. We propose a measure that quantifies the degree to which the local sufficiency condition is violated. The approach would be potentially useful in many tomographic applications, regardless of motion. In Chapter 8, we evaluate the proposed approach in simulations and a phantom study.

**Part III**

# Research articles

# Chapter 6

# An iterative projection-based motion estimation and compensation scheme for head X-ray CT

**Purpose** Although current CT systems can scan the head in a very short time, patient motion sometimes still induces artifacts. If motion occurs, one has to repeat the scan; to avoid motion, sedation or anaesthesia is sometimes applied.

**Method** We propose a method to iteratively estimate and compensate this motion during the reconstruction. We assume that the motion of the human head is strictly rigid. In every iteration, the rigid motion was estimated view-by-view and then used to update the system matrix. A multi-resolution scheme was used to speed up the convergence of this joint estimation of the image and the motion of the subject. A final iterative reconstruction was performed with the last motion estimate.

**Results** The method was evaluated on simulations, patient scans and a phantom

study. The quality of the reconstructed images was improved substantially after the compensation. In simulation and phantom studies, root-mean-square error (RMSE) was reduced and mean structural similarity (MSSIM) was increased. In the patient studies, most of motion blurring in the reconstructed images disappeared after the compensation.

**Conclusions** The proposed approach effectively eliminated motion-induced artifacts in head CT scans. Since only measured raw data is needed for the motion estimation and compensation, the proposed approach can be applied retrospectively to clinical helical CT scans affected by motion.

**Personal contribution** The PhD student proposed the methodology, with contribution from Johan Nuyts. Simulation was performed by the PhD student. Patient and phantom data were collected with the help of Roger Fulton and Jung-Ha Kim. Software was implemented, evaluated and optimized by the PhD student, who also drafted the manuscript. The co-authors Johan Nuyts, Roger Fulton and Jung-Ha Kim contributed to the editing of the manuscript.

## 6.1 Introduction

A slight movement of the patient can lead to a reduction of spatial resolution in Computed Tomography (CT), in severe cases resulting in corrupted images unsuitable for diagnosis or further processing. To reduce the likelihood of motion artifacts, CT manufacturers have made scans faster by increasing the number of detector rows and the rate of rotation of the x-ray source and detector. Other ways to reduce the patient motion include general anesthesia, sedation (Wachtel et al. 2009) and the use of restraining devices for head and neck imaging (Barrett et al. 2004).

In practice it is difficult to completely eliminate motion, and compensating motion artifacts is of considerable general interest in tomography. A variety of methods for assessing motion in CT exist, including directly estimating motion using a camera system with visual markers (Bhowmik et al. 2012; Kim et al. 2013, 2015b, 2016) or without markers (Noonan et al. 2012). Artificial or anatomical landmarks can be also tracked in the image or projection domains (Lu et al. 2002; Ritchie et al. 1996). Indirect estimation methods have been proposed where motion is estimated through the minimization of errors in consistency conditions (Clackdoyle et al. 2015; Leng et al. 2007; Yu et al. 2007, 2006), or estimate the motion by minimizing an image-based cost function (which essentially detects motion artifacts) (Kingston et al. 2011; Kyriakou et al. 2008; Rohkohl et al. 2013). Another approach has used similarity measures to quantify changes between successive projections to measure subject motion (Ens et al. 2009). Once motion parameters have been estimated, a compensation for the motion can be applied, either to the measured raw data or during the reconstruction process.

Among these methods, some addressed the problem in 2D parallel-beam or fan-beam geometries (Clackdoyle et al. 2015; Leng et al. 2007; Yu et al. 2007, 2006). Other retrospective motion estimation and compensation methods addressed the problem for 3D circular cone-beam CT (Kingston et al. 2011; Kyriakou et al. 2008; Lu et al. 2002; Ritchie et al. 1996). Motion estimation and compensation is arguably simpler in cone-beam CT since the entire object is normally in the field of view at all times. In contrast, in helical CT, the object is always truncated in the axial direction, limiting the amount of information that can be used to verify consistency of the projections. Relatively few studies have been done for clinical helical CT, and some of those require additional measurement to acquire the motion (Bhowmik et al. 2012; Kim et al. 2013, 2015b, 2016).

In this study, we propose an approach to reduce or eliminate motion artifacts in helical CT reconstruction. The proposed motion estimation and compensation method only needs the measured raw data. The method assumes that for each view, the pose of the measured object may be different. Consequently, for every view, a rigid transformation representing the object pose is estimated. An initial compensation for changes in pose (motion) during projection acquisition is applied during reconstruction by incorporating the motion estimates into the system matrix (Kim et al. 2015b). Then the motion and the reconstructed image can be updated alternately in an iterative scheme until an optimal motion estimate is found. The proposed approach has been validated on simulations and a phantom study by comparing reconstructed images with and without motion compensation. Results on patient scans are also presented.

## 6.2 Materials and Methods

### 6.2.1 Coordinate system

A clinical helical CT system usually has a cylindrical detector surface, with a radius equal to the detector source distance. We define the world coordinate system $c = (x, y, z) \in \Re^3$ in Fig. 6.1. It is fixed with respect to the scanner, and its $z$-axis coincides with the rotation axis of the scanner. The detector coordinate system $c' = (u, v, z) \in \Re^3$ is fixed with respect to the rotating source-detector system: its origin moves along $z$-axis while the system moves, $u$ is tangent and $v$ is orthogonal to the detector. For one projection view, we define the rigid motion transform in the coordinate system $c$:

$$S_{world} = (\varphi_x, \varphi_y, \varphi_z, t_x, t_y, t_z)^{\mathrm{T}} \tag{6.1}$$

where $\varphi_x$, $\varphi_y$, $\varphi_z$ are 3 rotations, $t_x$, $t_y$, $t_z$ are 3 translations. The motion can be mapped in a detector coordinate system $c'$:

$$S_{detector} = (\varphi_u, \varphi_v, \varphi_z, t_u, t_v, t_z')^{\mathrm{T}} \tag{6.2}$$

where $\varphi_u$, $\varphi_v$, $\varphi_z$ are rotations, $t_u$, $t_v$, $t_z'$ are translations. A small motion in the direction perpendicular to the detector $t_v$, results in a very small magnification of the projection, which is assumed negligible (Gullberg et al. 1987). In every projection view, then, we set $t_v$ to zero and only 5 parameters need to be estimated in our scheme in the detector coordinate system $c'$:

$$S_{detector} = (\varphi_u, \varphi_v, \varphi_z, t_u, t_z')^{\mathrm{T}} \tag{6.3}$$
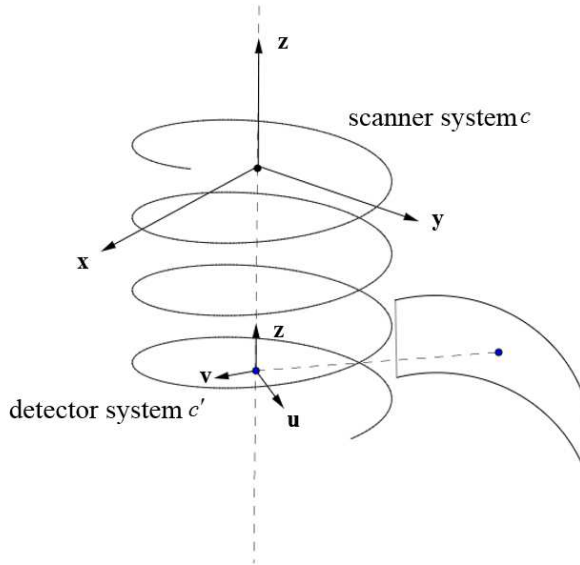


Figure 6.1: The scanner and detector system on which motion estimation and compensation is based. The offset along the rotation axis between origins of the two systems is $t_{offset}$.

## 6.2.2 OSEM reconstruction

In the presence of object motion, the helical CT-orbit is distorted into an effective orbit with arbitrary shape (Kim et al. 2015b). Because this is problematic for analytical reconstruction, an iterative reconstruction algorithm is needed. We used OSEM as the reconstruction algorithm (Hudson et al. 1994):

$$\mu_j^{k+1} = \frac{\mu_j^k}{\sum\limits_{i \in S_b} a_{ij}} \sum_{i \in S_b} a_{ij} \frac{l_i}{\sum\limits_h a_{ih} \mu_h^k} \tag{6.4}$$

where $l$ is the log converted sinogram, $S_b$ is one subset (consisting of $b$ views). We used the OSEM algorithm for convenience, but if the use of a better noise model would be required, it can be replaced with a dedicated iterative algorithm for transmission tomography (Nuyts et al. 1998).

### 6.2.3 General motion estimation and compensation scheme (ME/MC)

The aim is to estimate the pose of the object for each of the acquired CT views. This is achieved by a 3D registration of the object to each of the 2D views independently. The first estimate of the 3D object is obtained with an initial reconstruction without motion compensation. As a result, that first image suffers from motion artifacts, which will adversely affect the accuracy of pose estimates associated with each view. Nevertheless, we find that the 2D-3D registration process described below still captures part of the true motion, such that reconstruction with motion compensation based on these (poor) motion estimates improves the reconstruction. Reiterating the process with this improved reconstruction in turn produces more accurate motion estimates. This leads to an iterative algorithm which alternately estimates the motion for each view and the motion compensated image. This algorithm is explained in more detail in the following paragraphs.

Although the initial reconstructed image is motion-contaminated, it can be used to generate a first rough motion estimate. This motion is taken into account in a reconstruction process to generate a motion-corrected image at the first iteration. Then the motion-corrected image and the motion estimate are alternately updated to increase the likelihood, the iterations are stopped when the updated motion seems to have converged (Fig. 6.2). The algorithm consists of two parts: (1) the joint image and motion estimation (JIM) and (2) the final reconstruction (motion compensation). Each JIM-iteration consists of 2 steps: a motion update and an image update. The image update is done by applying multiple iterations of the OSEM algorithm.

Hence, the implementation involves four steps: (1) a motion update, a 2D-3D image registration to update the pose estimate for each view in the current JIM-iteration; (2) an image update, computed with an iterative reconstruction algorithm incorporating the updated motion estimate in its system matrix at the current JIM-iteration; (3) alternate updates of both image and motion within a multi-resolution scheme; (4) final reconstruction with a system matrix based on the last motion estimate. Details on each part of the framework are described below.
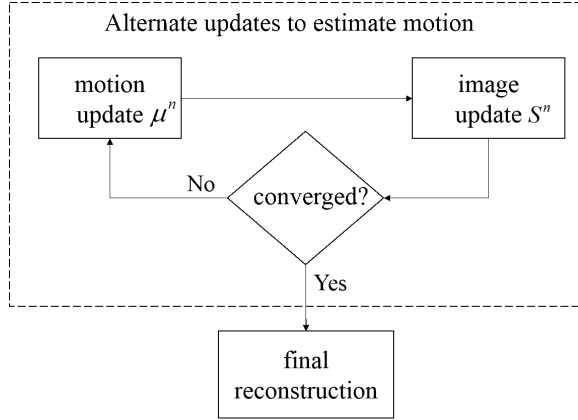
Figure 6.2: General motion estimation and compensation scheme. $\mu$ is the update of the attenuation image, $S$ is the update of the rigid motion.

### Motion update

For one projection line $i$, we integrate along the projection line to define the forward projection of the estimated image $\mu$ at current JIM-iteration:

$$l_i = \sum_j a_{ij} \mu_j \qquad (6.5)$$

where $i$ is the projection line index, $j$ is the voxel index, $a_{ij}$ is the effective intersection length of the line $i$ with voxel $j$. In helical CT, the line integrals are organized in views, where view $\theta$ contains all line integrals associated with a single source position:

$$l_\theta = \{l_i\} \qquad (6.6)$$

Suppose the general motion estimation and compensation scheme (Fig. 6.2) is at the JIM-iteration $n$, hence the current motion estimate is $s^n$. For view $\theta$, the current pose estimate is $s_\theta^n$ and the 5 motion parameters in Eq. 6.3 are estimated one after the other. Let $r$ be one of these parameters (a rotation or translation) to be estimated. Assuming that the change in the pose parameter represented by $\hat{r}$ is small, the derivative of projection $l$ with respect to $r$ can be approximated as a finite difference of the intensities:

$$\frac{\partial l_\theta}{\partial r} \approx \frac{l_{\theta,m} - l_\theta(s_\theta^n)}{\hat{r}} \qquad (6.7)$$

where $l_\theta(s_\theta^n)$ is the calculated re-projection (using the current estimates of the image and motion), $l_{\theta,m}$ is the measured projection for view $\theta$. For view $\theta$, $\hat{r}$ minimizes the difference between $l_\theta(s_\theta^n + \hat{r})$ and $l_{\theta,m}$. To estimate $\hat{r}$ in Eq. 6.7, we need to know the derivative on the left hand side. Therefore, we introduce another equation which is very similar to Eq. 6.7:

$$\frac{\partial l_\theta}{\partial r} \approx \frac{l_\theta(s_\theta^n + \Delta r) - l_\theta(s_\theta^n)}{\Delta r} \qquad (6.8)$$

where $\Delta r$ is a known small increment of the parameter to be estimated. When $\Delta r$ represents a translation, $l_\theta(s_\theta^n + \Delta r)$ can be approximated as a simple translation of current re-projection $l_\theta(s_\theta^n)$; for in-plane rotation, again $l_\theta(s_\theta^n + \Delta r)$ can be approximated as a simple rotation of the re-projection $l_\theta(s_\theta^n)$, as shown in Fig. 6.3 For the two out-of-plane rotations, we calculated $l_\theta(s_\theta^n + \Delta r)$ with a forward projection using a system matrix adjusted with $\Delta r$.

Eq. 6.7 and Eq. 6.8 assume that a small increment of one degree-of-freedom rigid motion only results in a linear change of the intensities in the projection. All the above lead to a least squares minimization problem for view $\theta$ at the current JIM-iteration $n$:

$$\hat{r} = \arg\min_r \|\Delta r\, [l_{\theta,m} - l_\theta(s_\theta^n)] - r\, [l_\theta(s_\theta^n + \Delta r) - l_\theta(s_\theta^n)]\|^2 \qquad (6.9)$$

To find $\hat{r}$, Eq. 6.10 was solved analytically. Defining

$$\begin{aligned} P_\theta &= l_{\theta,m} - l_\theta(s_\theta^n) \\ Q_\theta &= l_\theta(s_\theta^n + \Delta r) - l_\theta(s_\theta^n) \end{aligned} \qquad (6.10)$$

and setting the derivative of the right hand side in Eq. 6.9 with respect to $r$ to zero, one obtains:

$$\hat{r} = \frac{\sum\limits_N P_\theta \cdot Q_\theta}{\left\|\sum\limits_N Q_\theta{}^2\right\|} \Delta r \qquad (6.11)$$

where $N$ is total number of voxels in projection view $\theta$.

The above procedure showed how to estimate one parameter in one projection view. For view $\theta$, this procedure was applied to estimate all five parameters in Eq. 6.3. The sequence of the estimation was translation first, then rotation. The newly estimated parameter values were used immediately when estimating

the value of next parameter. This sequential estimation of five motion para-
meters for all projection views completes the update of the rigid motion at the
current JIM-iteration (Fig. 6.2).

Now the estimated motion is obtained in the detector coordinate system $c'$
(Fig. 6.1). It is transformed to the motion in the world coordinate system $c$,
as motion-corrected reconstruction requires the motion in the world coordinate
system:

$$\left\{ S_\theta^{n,inc} \mapsto T_\theta^{n,inc} \right\}_{\theta=0,\dots,M} \tag{6.12}$$

where $T$ is the $4{\times}4$ homogeneous matrix representation of the estimated motion
in the world coordinate system. More details about Eq. 6.12 are given in the
Appendix.

The transformation matrix obtained in the $n$th JIM-iteration was then used
to update the previous motion estimate for every view, which was used in the
next JIM-iteration $(n+1)$:

$$\left\{ T_\theta^{n+1} = T_\theta^n T_\theta^{n,inc} \right\}_{\theta=0,\dots,M} \tag{6.13}$$
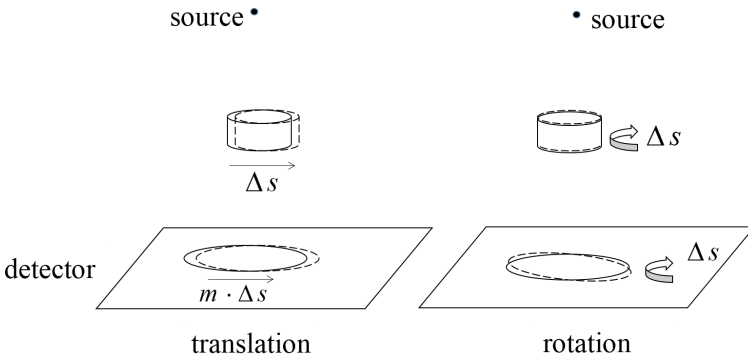


Figure 6.3: In the detector coordinate system, the effect of object translation
or rotation parallel to the detector can be well approximated as translation
and rotation of the projection. For simplicity, the curvature of the detector is
ignored. In the left half figure, $m$ is the magnification factor from the object
to detector.

**Image update**

After obtaining the motion, the image representing the attenuation coefficients
can be updated with iterative reconstruction. We used OSEM as the recon-

struction algorithm.

Instead of moving the reconstructed image in every view, rigid motion compensation is done by considering a coordinate system fixed to the object and incorporating the motion (now associated to the source-detector pair) into the system matrix. This corresponds to an arbitrary 3D motion of a virtual gantry around the object being scanned, created by the superposition of the inverse of the object motion on the helical trajectory (Kim et al. 2015b). Motion compensation is enabled by introducing a modified version of standard OSEM:

$$\hat{T}_i^{n+1} = invert(T_i^{n+1})$$
$$\mu_j^{n+1} = \frac{\mu_j^n}{\sum\limits_{i \in S_b} \hat{T}_i^{n+1}(a_{ij})} \sum\limits_{i \in S_b} \hat{T}_i^{n+1}(a_{ij}) \frac{l_i}{\sum\limits_{k} \hat{T}_i^{n+1}(a_{ik})\mu_k^n} \qquad (6.14)$$

where $\hat{T}_i$ is a $4 \times 4$ transformation matrix applied to the projection line $i$. If $T_i$ is the identity matrix for all projection lines, then Eq. 6.14 is the same as standard OSEM (Eq. 6.4). In helical CT, $T_i$ is constant for all projection lines in one projection view, hence the inversion is done for every single view. Because of the high rotation speed and the large number of views, the motion within a single view is negligible.

Distance-driven projection is used for interpolation during the (back) projection (De Man et al. 2004). The new estimate of the attenuation image is then used for the next motion update.

Image update

level 4, 64×64×64,        1 iteration 20 subsets
level 3, 128×128×128,     1 iteration 30 subsets
level 2, 256×256×256,     1 iteration 40 subsets
level 1, 512×512×512,     no updates

Figure 6.4: An example of the number of OSEM-iterations and subsets applied for the image update at each resolution level. Note that we stop the estimation at the second last level, hence no image and motion updates were computed at level 1.

**Multi-resolution alternate updates**

By repeating steps 1 and 2 we can update the motion (Eq. 6.13) and reconstruction (Eq. 6.14) alternately. Because the image and the motion parameters are jointly estimated from the measured data, the problem of error propagation is minimized. An approach to reduce computation time is to apply a multi-resolution technique. We utilized this by running the algorithm from a coarse

to fine representation of the image. For example, the starting image resolution level is $8 \times 8 \times 8$, i.e. a down-sampling factor of eight was applied in all directions. There is a resampling with a factor of two between adjacent levels. Image updates were reconstructed at coarse resolution at early JIM-iterations, while the resolution increased as the iteration numbers increased. The number of OSEM-iterations applied for the image update was the same within one resolution level. These numbers were optimized based on simulations which had a similar configuration as the patient study (Fig. 6.4). A possible additional advantage of the multi-resolution technique is that it may help avoiding convergence to an undesired local maximum.

It was not obvious how to define good stopping criteria when estimating the motion at each level, especially considering that the ground truth image was missing for clinical studies. In our implementation, the summation of projection errors between the re-projected and measured data over all views was computed, and at each resolution level, the iterations were stopped when the relative change of this error measure did not exceed 0.2 %. In our experiments, we observed that the motion estimate hardly changed during the computations at the finest resolution. Since these computations (if included) are the most expensive ones in the multi-resolution scheme, we stopped the scheme at the second finest resolution.

The motion updates were smoothed (by filtering each degree-of-freedom independently along the projection views) to remove outliers. We chose the Savitzky-Golay filter (Savitzky et al. 1964) to do the smoothing. The optimal size of the smoothing kernel depends on both the view sampling rate of the measured data and the axial detector extent. The clinical data usually have a high view sampling rate, while we used a lower rate in simulations. The axial extent varies with different scan configuration (slice collimation). The optimal smoothing kernels are determined by simulations with several common collimation configurations, as shown in Table 6.1. If the number of views per rotation is increased, the number of kernel points is increased accordingly.

Table 6.1: The motion smoothing kernel width for common slice collimation

|  | Case 1 | Case 2 | Case 3 | Case 4 |
|---|---|---|---|---|
| Angles per rotation | 150 | 150 | 150 | 150 |
| Collimation (mm) | $96 \times 0.6$ | $64 \times 0.6$ $(32 \times 1.2)$ | $32 \times 0.6$ | $16 \times 0.6$ |
| Smoothing kernel (points) | 17 | 23 | 75 | 105 |

**Final reconstruction**

When the motion estimate has converged, a final reconstructed image with diagnostic quality must be produced for a clinical scan (Fig. 6.2). One way to speed up the final reconstruction is choosing an initial image which is close to the maximum likelihood solution. Faster convergence is achieved if the iterative reconstruction could be started from a sharper image. In simulations we started the final reconstruction with the last image update from the alternate updates. Since the alternate multi-resolution scheme was terminated at a coarser grid, the initial image must be created by interpolating to the finer grid, and as a result, the initial image is relatively smooth.

For that purpose, we implemented an approximate helical FDK algorithm. We utilized all the data in each projection view. A first order motion compensation is obtained by taking the motion for each view into account in the backprojection step. This approximation creates artifacts, but these have typically low spatial frequencies. Since low frequencies tend to converge relatively fast in iterative algorithms such as OSEM, only few updates are needed to eliminate them. For the clinical studies, this FDK-initialisation was used since it was found to be more efficient to reach convergence.

To further accelerate the final reconstruction, Nesterov's momentum approach (Nesterov 2005) was applied (using all previous iterates to compute the momentum) in the final reconstruction. All forward and backward projection operations were also implemented in OpenCL and run on a GPU (NVIDIA Tesla C2075).

## 6.2.4   Design of the experiments

**Simulations**

In simulations, measured motion segments from volunteers were applied to a phantom to generate simulated CT scans subject to patient motion. Details about measuring these motions are given in (Kim et al. 2016). The phantom was a 3D voxelized phantom from the Visible Human Project (Ackerman 1998). The image intensities were converted from Hounsfield (HU) to attenuation coefficients $(cm^{-1})$ at an effective energy of 70 keV. Image size was $256 \times 256 \times 240$; pixel size was $1 \times 1 \times 1$ mm$^3$.

All helical scans were simulated as being scanned with a Siemens Definition AS CT scanner (Siemens Medical Solutions USA, Inc., Malvern, PA), with reduced angular sampling to reduce computation times. The scan parameters were: angles per rotation 150, pitch 1.0, collimation $32 \times 1.2$ mm. Six measured motion segments (referred as studies 1 to 6) were applied to the phantom for the simulated helical scans. Examples of volunteer motion segments are shown in Fig. 6.5. To avoid artifacts, all simulated helical scans covered a bit more

than the entire object. Reconstructed images from these scans were analyzed quantitatively to assess the performance of the proposed approach.

Alternate updates of both image and motion were performed within the multi-resolution scheme to obtain the final motion estimate. OSEM was used for all reconstructions, with motion compensation enabled (Eq. 6.14). During the JIM, the attenuation image was updated using the OSEM iteration schemes shown in Fig. 6.6. For the final reconstruction, the pixel size was $1 \times 1 \times 1$ mm$^3$, and 4 iterations with 60 subsets were applied.

Poisson noise was added to the raw simulated data before the reconstruction (assuming 1000 photons were detected on each detector element in the blank scan). Again OSEM was used for this reconstruction, but as mentioned in Section 6.2.2, it can be replaced by a dedicated iterative algorithm for transmission tomography.
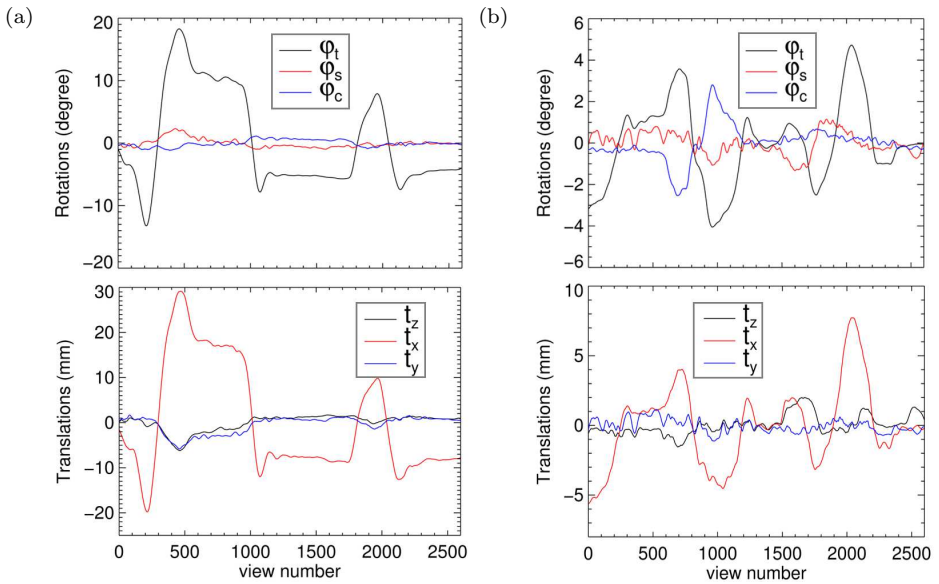


Figure 6.5: Examples of the simulated volunteer head motion. (a) Moderate motion from study 1. (b) Slight motion from study 6. Details of motion tracking are given in (Kim et al. 2016).

**Patient scans**

The method has been applied to clinical studies in which motion artifacts had been observed. The anonymized raw data of four patients who had previously undergone head CT scans in the Department of Radiology at Westmead Hospital, Sydney, Australia, were collected with the approval of the Human Research Ethics Committee of the Western Sydney Local Health District. The

scans were performed on a Siemens Force scanner (Siemens Medical Solutions USA, Inc., Malvern, PA). The scan parameters are listed in Table 6.2.

Because the head support and the bed do not move with the patient during the scan and would compromise the estimation of the patient motion, they were removed from the raw data prior to further processing. The head support and (or) bed were firstly segmented from an initial low-resolution reconstructed image. The segmented portion of image was then forward-projected to generate a new set of projections, which were subtracted from the measured projections before the motion estimation and compensation scheme was executed.

Because of the large size of the raw data, motion was estimated at every 8th view to accelerate both motion and image updates. This resulted in approximately 500 views per rotation. With a rotation time of 1 s, this yields a temporal sampling of 500 Hz, which was considered sufficient for motion estimation. The multi-resolution JIM scheme was applied as in Section 6.2.3. For all patient studies, the motion smoothing kernel sizes were selected based on Table 6.1.

For the final OSEM reconstruction, the starting image was computed with helical FDK reconstruction with motion compensation enabled. Six iterations with 30 subsets were applied in combination with Nesterov's acceleration. Other reconstruction parameters are listed in Table 6.2. Also, the entropy of the reconstructed images was computed for reconstructions with and without motion compensation for comparison.

Table 6.2: Scan and reconstruction parameters

|  | Patient 1 | Patient 2 | Patient 3 | Patient 4 |
|---|---|---|---|---|
| Tube voltage (kVp) | 120 | 120 | 120 | 120 |
| Tube current (mA) | 120 | 154 | 150 | 150 |
| Rotation time (s) | 1.0 | 1.0 | 1.0 | 1.0 |
| Pitch | 0.55 | 0.55 | 0.55 | 0.55 |
| Angles per rotation | 4200 | 4200 | 4200 | 4200 |
| Collimation (mm) | $64 \times 0.6$ | $96 \times 0.6$ | $32 \times 0.6$ | $96 \times 0.6$ |
| Flying focus | phi, z | phi, z | phi, z | phi, z |
| Pixel size ($mm^3$) | $0.4 \times 0.4 \times 0.75$ | $0.45 \times 0.45 \times 0.5$ | $0.455 \times 0.455 \times 0.5$ | $0.451 \times 0.451 \times 0.5$ |
| Dimension | $512 \times 512 \times 219$ | $512 \times 512 \times 550$ | $512 \times 512 \times 376$ | $512 \times 512 \times 404$ |

**Phantom scan**

In our previous work (Kim et al. 2015b), we developed and optimized a rigid motion compensation technique for helical CT brain scanning, in which the motion information was obtained using an optical motion tracking system. We observed that after motion compensation based on the tracking data, some residual artifacts were still present. We attributed these artifacts to the finite accuracy of the motion tracker. In this experiment, we verified whether the proposed approach can be used to refine the motion estimate from the optical system.

The scan was performed in the Department of Nuclear Medicine and Ultrasound at Westmead Hospital, on a Siemens Sensation 16 scanner (Siemens Medical Solutions USA, Inc., Malvern, PA). The scan parameters were: pitch 1.0, tube voltage 120kVp, tube current 280 mA and tube collimation $16 \times 0.6$ mm. Flying focus was turned off.

An optical motion tracking system (Polaris Spectra, Northern Digital Inc., Waterloo, Canada) was placed at the rear of the scanner. A 3D Hoffman brain phantom, which contained air inside was used in this experiment. The phantom was placed off-center on the curved bed and held in place with a wedge (Fig. 6.6a). During the scan, the wedge was removed by pulling a string from outside the room. The phantom then started rolling left and right on the bed to finally come to rest at a stable position at the center of the bed. This motion was too severe to be compensated only by the proposed approach, since the initial reconstruction was corrupted severely. The tracked rigid motion is shown in Fig. 6.6b, relative to its pose at the start of the scan.

## 6.2.5 Evaluation of the results

In the simulation studies, the effects of motion compensation were evaluated by visual assessment and with quantitative analysis. The reconstructed images and the ground truth images were compared in all planes with similarity metrics. We chose RMSE and MSSIM (Wang et al. 2004) as the metrics. Note that before the calculation of these metrics, both motion-corrected and uncorrected images were registered to the true image plane by plane (Fig. 6.7). This was done because motion and motion-compensation may introduce positional differences which are irrelevant for image quality and therefore should not affect the evaluation of similarity.

In the patient studies, image entropy, with and without motion compensation applied, was also computed (plane-by-plane), based on the assumption that motion-induced artifacts would tend to increase the image entropy.

In the phantom study, the quality of the reconstructed images was assessed for reconstructions with and without motion compensation by comparison to reconstructions from motion-free CT-scans.
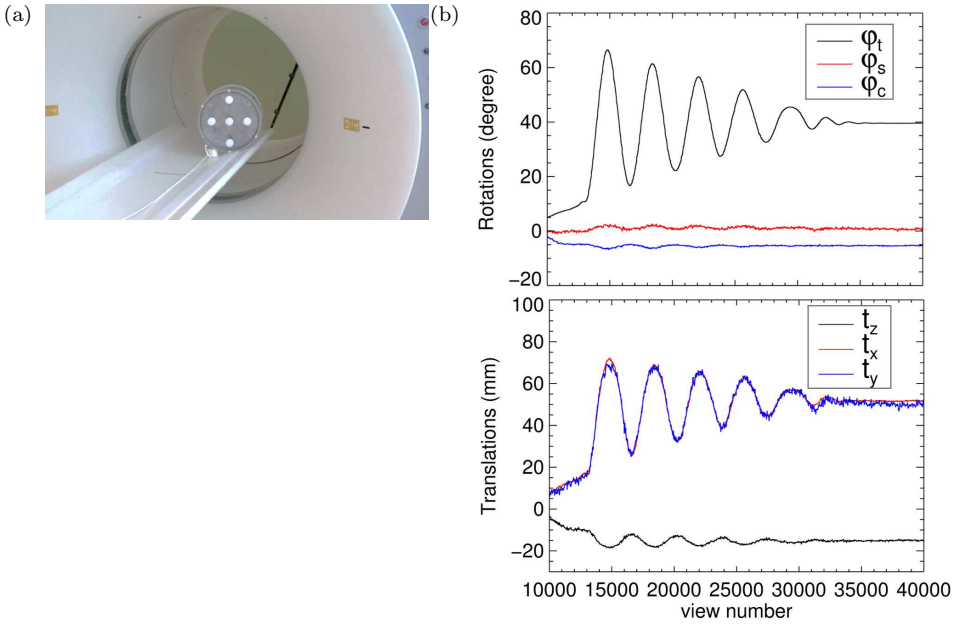
Figure 6.6: (a) Setup of the Hoffman phantom used in the experiment, and (b) measured motion.
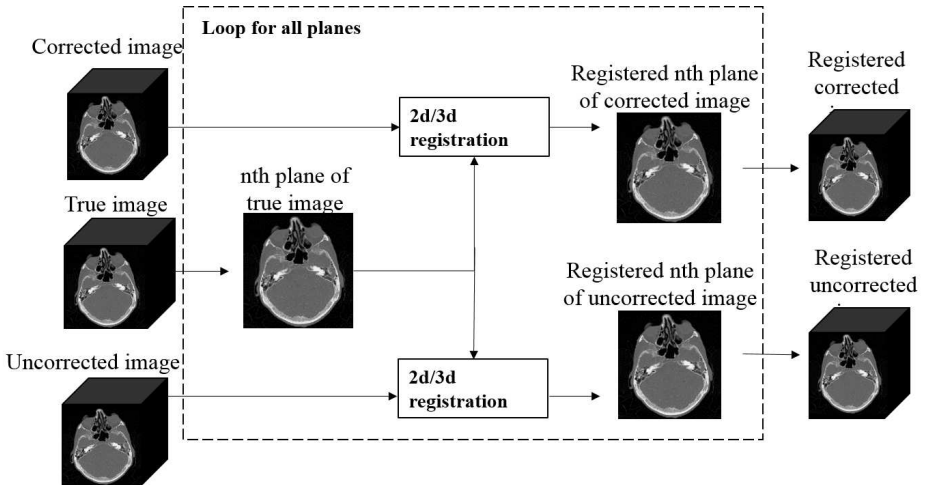


Figure 6.7: Pre-processing of the motion-corrected and uncorrected images before quantitative analysis in simulation studies.

## 6.3 Results

### 6.3.1 Simulations

Fig. 6.8 shows the corrected image of a selected simulation using a moderate motion segment. Most of the distortions are eliminated. Fig. 6.9 shows the quantitative analysis of a selected simulation using a slight motion segment. The true image is much more similar to the corrected image than the uncorrected one. Fig. 6.10 shows the overall improvement across all image planes in all 6 studies with different motions. Fig. 6.11 shows the result of the simulation study 1 with relatively high noise. The motion estimation and compensation is still effective on data with high noise level.
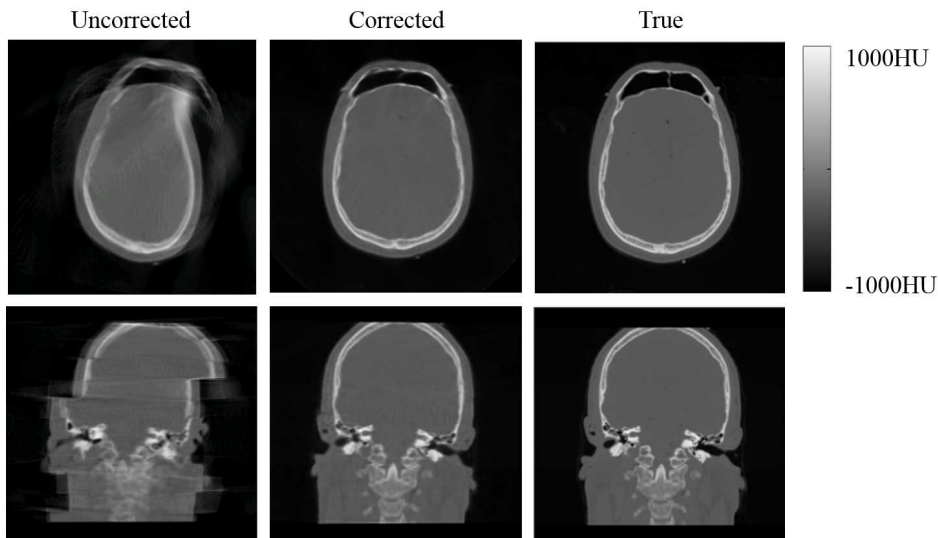


Figure 6.8: Results from the simulation study 1 using moderate motion (Fig. 6.5a). Selected transaxial (top) and coronal (bottom) slices from reconstructions without and with motion compensation, and also from the true image.

### 6.3.2 Patient scans

Fig. 6.12 and Fig. 6.13 show the non-motion corrected image (reconstructed with the scanner system software) and motion-corrected reconstructed images from patient 1 and patient 2, respectively. Fig. 6.14 compares the image of a repeat scan (which was done because of the observed motion in the first scan) with the reconstructions, with and without motion compensation for patient
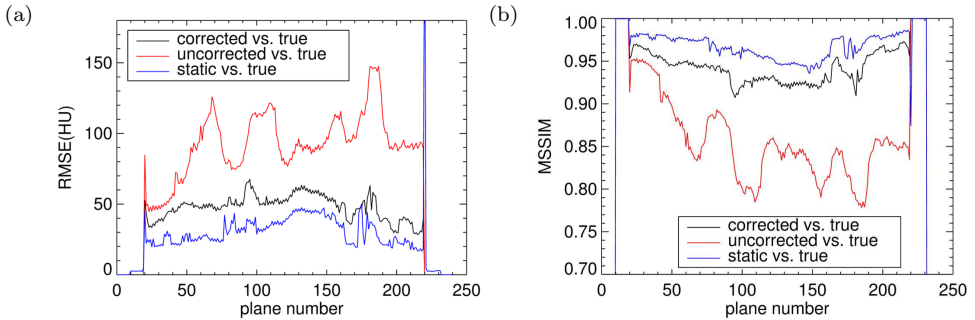
Figure 6.9: Results from the simulation study 6 using slight motion (Fig. 6.5b). Similarity metrics with and without motion compensation over reconstructed planes. Top: RMSE. Bottom: MSSIM. The difference between the static reconstruction and true image was displayed as the reference.
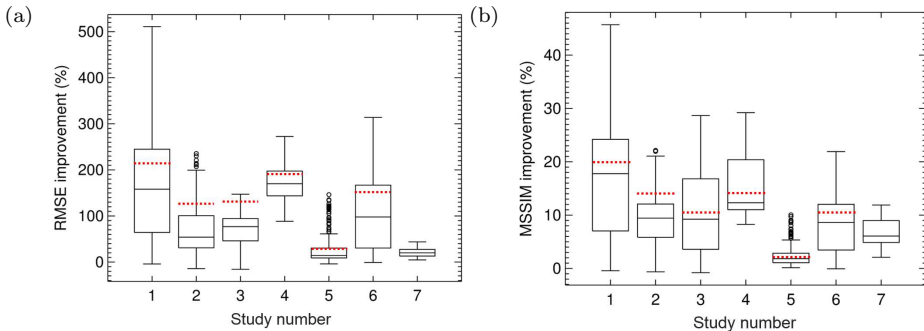


Figure 6.10: Box plots of improvement over reconstructed planes of each individual study — simulation studies (1-6), phantom scan (7). Left: RMSE improvement. Right: MSSIM improvement. The upper and the lower limit of the bar are the maximum and minimum. The upper and the lower limit of the box are the first and third quartiles. The central line is the median. The circles are the outliers. As a reference for each study, the red dashed lines represent the medians of the improvement of the static reconstructed image over the uncorrected image.

Uncorrected　　　　Corrected
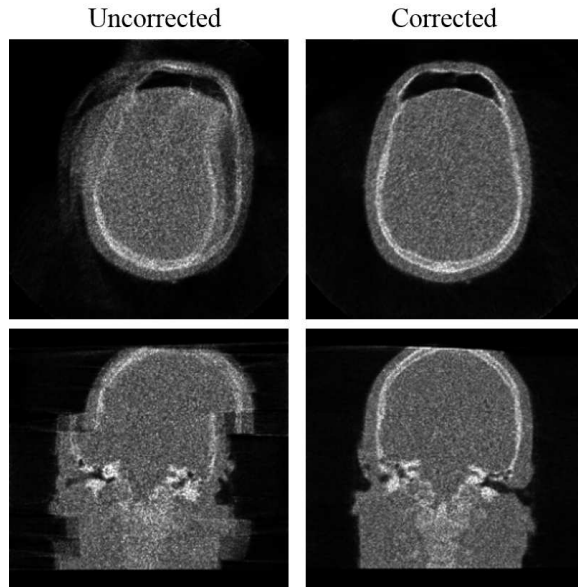


Figure 6.11: Noisy simulation of study 1. Selected transaxial (top) and coronal (bottom) slices show the improvement on image quality.

3. Fig. 6.15 shows the change of the total image entropy, as an indicator of artifact reduction.

### 6.3.3 Phantom scan

As shown in the top row of Fig. 6.16, some small irregularities were visible at the edges of the phantom in the reconstructed image after a first compensation using the tracked motion. A possible reason is the finite accuracy of the pose measurements. For this scan, we applied the proposed approach to compensate these residual "jagged" artifacts due to the imperfect motion recording. The motion estimation process was identical to the one applied in the patient studies, except that the measured motion was used as the initial motion estimate. The proposed approach removed the artefacts (Fig. 6.16, middle). Quantitative analysis was done similarly to what has been done in simulation studies. The true image was obtained from a static scan of the same phantom. Fig. 6.10 (box 7) shows the overall improvement of the RMSE and MSSIM across image planes.
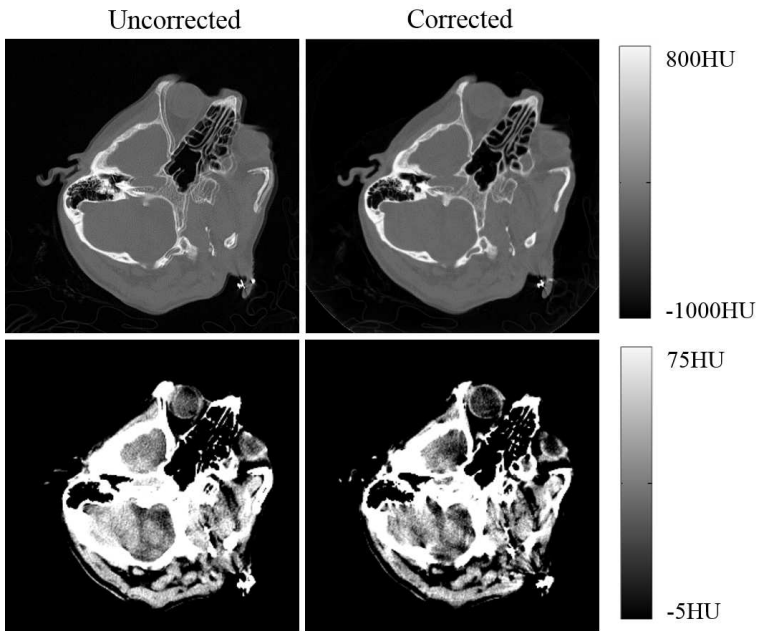
Figure 6.12: Top: Selected transaxial plane, without (left) and with (right) compensation for motion artifacts in a scan from patient 1. The uncorrected image was from a standard vendor reconstruction. Bottom: the same plane that is shown in a narrow window (Gaussian smoothed with full width at half maximum (FWHM) = 2 mm).

Uncorrected          Corrected
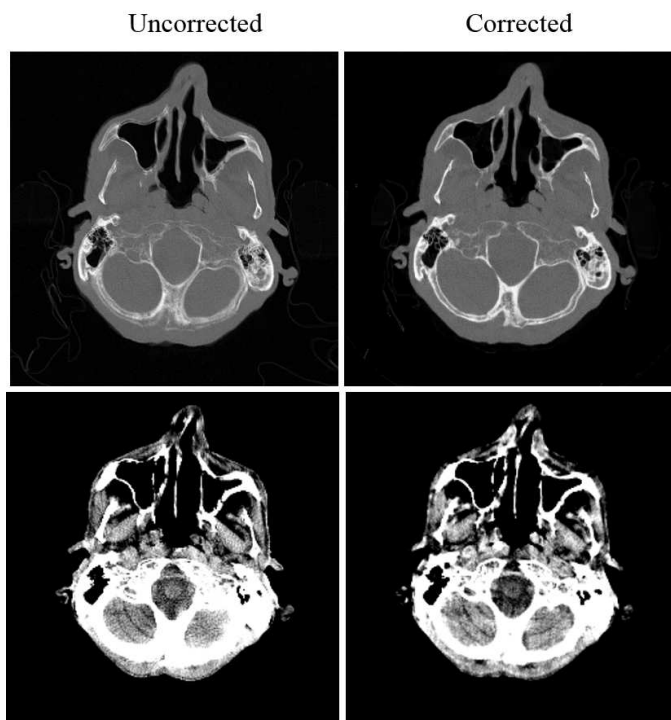


Figure 6.13: Top: Selected transaxial plane, without (left) and with (right) compensation for motion artifacts in a scan from patient 2. Bottom: the same plane that is shown in the same narrow window used in Fig. 6.12 (Gaussian smoothed with FWHM = 2 mm).
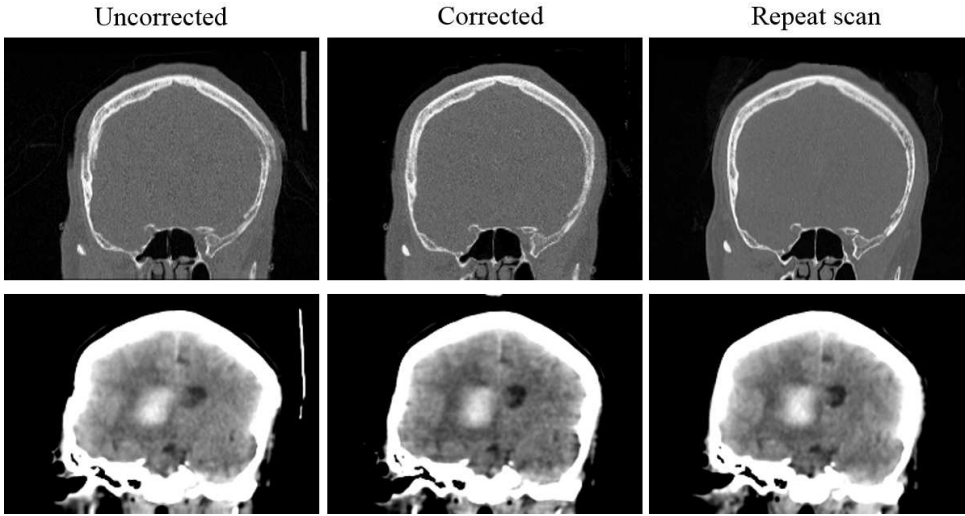
Figure 6.14: Top: Selected coronal plane without (left) and with (middle) compensation in a scan (effective mAs 272) from patient 3. As a reference, the repeated scan (effective mAs 327, registered to the first scan) is displayed on the right. Bottom: another plane contains a lesion that is shown in the same narrow window used in Fig. 6.12 (Gaussian smoothed with FWHM = 2.5 mm).
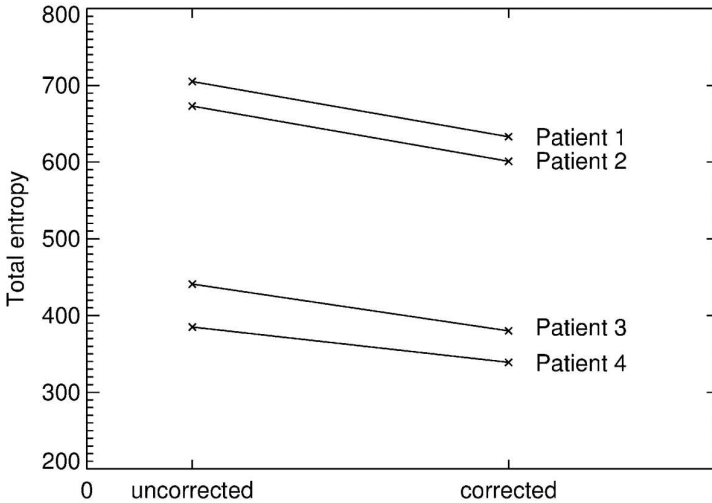


Figure 6.15: The total entropy change for 4 patient scans. The entropy in each individual plane (not shown here) decreased for all the studies.
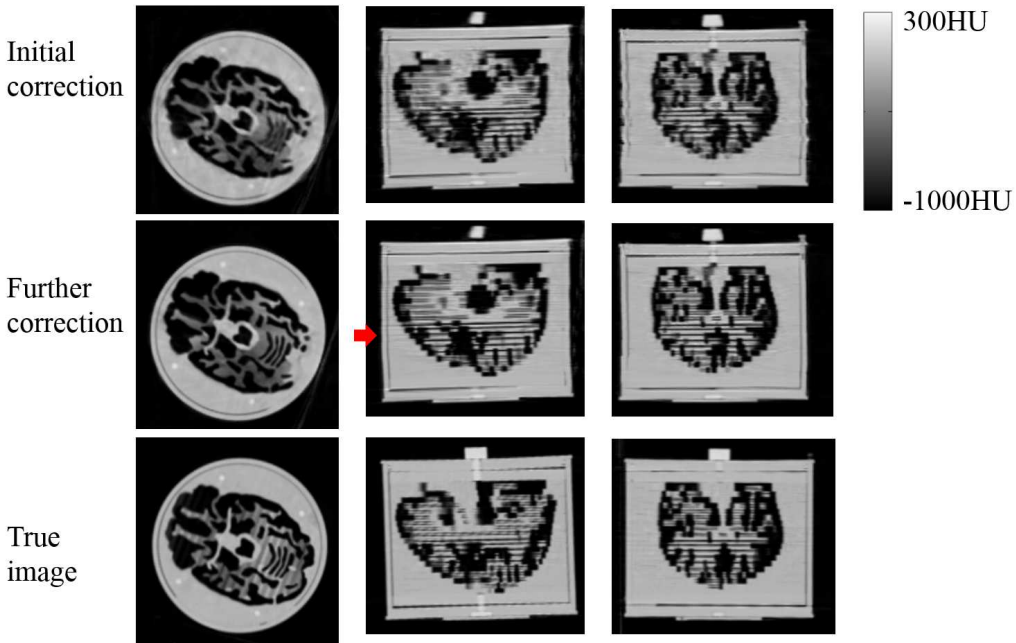
Figure 6.16: Selected transaxial, sagittal and coronal planes, with and without compensation for residual motion. Top: reconstructed image with motion compensation based on optical tracking data; Middle: reconstructed image with further compensation by the proposed approach; Bottom: reference image reconstructed from a static scan.

# 6.4 Discussion

In this paper, the simulation studies were performed with a (simulated) 64-row CT scanner, while the patient studies were performed with a 96-row CT, and the phantom study was performed with a 16-row CT. In other tests (not shown here), the method performed well for data from scanners with different row numbers as well, but the performance of the proposed approach was found to be better in the case of a higher number of detector rows, as expected since a wider detector provides more information in a single projection view. For the data from a scanner with a narrower detector, a stronger smoothing was needed to suppress the noise on the estimated motions (Table 6.1).

The large number of CT views in clinical scans creates an impressive computational challenge. Currently, the time for estimating the motion is about 2 hours for a single patient scan (from Siemens Force scanner), while the time for the final iterative reconstruction is about 12 hours (a high number of updates is required to obtain a quality comparable to the vendor images). A possible way to accelerate the final reconstruction is to replace the iterative reconstruction algorithm with a dedicated motion-sensitive analytical reconstruction algorithm. This is under development by the authors.

As illustrated in Fig 6.8, the proposed approach performed well even for relatively large patient motion. In our simulations, the proposed approach usually worked well when the amplitude of the rotations was less than $10°$ and amplitude of the translations was less than 20 mm, which in our opinion are unlikely to be exceeded in most clinical scans. Nevertheless, we observed that it did not perform well in cases of severe motion such as that of Fig. 6.6b. We have shown previously that optical motion tracking methods are effective, even for very severe motion (Kim et al. 2015b, 2016). As shown in Section 6.3.3, the proposed approach can refine the tracker based motion estimation. Consequently, combining both methods would relax the specifications for the tracking device significantly and at the same time provide accurate motion compensation even in the presence of very severe motion.

The multi-resolution technique accelerated the motion estimation algorithm. Using too coarse a starting resolution, however, should be avoided because the excessive blurring may suppress important high-frequency features. We observed that this can lead to an overestimation of the motion.

We ignored estimating the translation perpendicular to the detector in every projection view. We repeated the simulation studies in Section 6.3.1, where that translation was estimated and compensated too. The results (not shown) indicated that compensating for that translation had no or a negligible effect on the quality of the corrected image. Considering the additional time to estimate that particular motion, we did not take it into account in our studies.

The estimated motion is not always identical to the true motion. First, the pose of the reconstructed object is arbitrary, and probably roughly corresponds

to the average pose during the scan. Moreover, slow components of the motions may not be fully estimated, but instead partly be incorporated as a gradual and almost rigid distortion of the image along the z-axis. Such a small distortion can be observed in the phantom image of Fig.6.16 (middle). These small distortions are not expected to have an adverse effect on the diagnostic value of the image.

The proposed approach relies on 2D-3D image registration, and is therefore expected to be less effective when the contrast in the object is low. In CT brain imaging, the high contrast between the skull and soft tissue was found to provide adequate information for estimating the motion. For other possible applications where the contrast would be lower, pre-processing to enhance the contrast of the raw projection data might be necessary.

We only considered the application on diagnostic CT where the noise in the raw data is typically very low. We performed a noisy simulation, in which the proposed approach worked fine even with relatively high Poisson noise. We think one reason is that most of the artifacts were already eliminated during the early resolution levels, which had smooth image updates as the pixel size was large. Still, it would be interesting to investigate how the proposed approach works on the data from low dose CT scans.

The motion was estimated using an analytical expression based on a linearization. Instead, a more accurate non-linear least squares algorithm could be used. However, that approach would have a much larger computational cost. The linearization approximation becomes better closer to convergence, and the experimental results indicate that even for large motions it is good enough to improve the estimate in every JIM-iteration.

In our current approach, an independent rigid motion was estimated for every view. The method could be further improved by modelling the motion as a parameterized function of time (or view number) (Clackdoyle et al. 2015; Yu et al. 2011). This would reduce the number of unknowns and impose a physically meaningful smoothness to the estimated motion.

## 6.5 Conclusion

In this paper, we proposed a rigid motion estimation and compensation approach for helical X-ray CT of the head, for which the only required input is the measured raw data. Since no additional measurements are needed, it can be applied retrospectively to standard helical CT data. We believe that, when sufficiently accelerated, it can become a valuable clinical tool, since it would reduce the need for anaesthesia or sedation in children and other patients who are likely to move, and decrease the number of repeat scans. Further testing of the method with more clinical data is ongoing.

## Acknowledgement

## Appendix A

This section explains how the rigid motion parameters in the detector coordinate system are transformed to a homogeneous matrix in the world coordinate system. From Eq. 6.3, we have 5 degrees-of-freedom for each projection view $\theta$:

$$S_{detector} = (\varphi_u, \varphi_v, \varphi_z, t_u, t_z)^{\mathrm{T}}$$

Transform $S_{detector}$ into homogeneous matrix:

$$
T_{detector} =
\begin{bmatrix}
\cos\varphi_z & -\sin\varphi_z & 0 & 0 \\
\sin\varphi_z & \cos\varphi_z & 0 & 0 \\
0 & 0 & 1 & 0 \\
0 & 0 & 0 & 1
\end{bmatrix}
\begin{bmatrix}
1 & 0 & 0 & 0 \\
0 & \cos\varphi_u & -\sin\varphi_u & 0 \\
0 & \sin\varphi_u & \cos\varphi_u & 0 \\
0 & 0 & 0 & 1
\end{bmatrix}
$$
$$
\begin{bmatrix}
\cos\varphi_v & 0 & \sin\varphi_v & 0 \\
0 & 1 & 0 & 0 \\
-\sin\varphi_v & 0 & \cos\varphi_v & 0 \\
0 & 0 & 0 & 1
\end{bmatrix}
\begin{bmatrix}
1 & 0 & 0 & t_u \\
0 & 1 & 0 & 0 \\
0 & 0 & 1 & t_z \\
0 & 0 & 0 & 1
\end{bmatrix}
$$

Now the motion is in detector coordinate system, we still need to map $T_{detector}$ into world coordinate system:

$$
T_{world} =
\begin{bmatrix}
\cos\theta & -\sin\theta & 0 & 0 \\
\sin\theta & \cos\theta & 0 & 0 \\
0 & 0 & 1 & t_{offset} \\
0 & 0 & 0 & 1
\end{bmatrix}
\cdot T_{detector}
$$

where $t_{offset}$ is the offset between the world and detector system in the direction of bed movement.

# Chapter 7

# A motion compensation approach for dental cone-beam region-of-interest imaging

*This chapter is modified based on the publication: T. Sun, J. Nuyts, R. Fulton, "A motion compensation approach for dental cone-beam region-of-interest imaging," in Conference Record of International Meeting on Fully Three-Dimensional Image Reconstruction in Radiology and Nuclear Medicine, Xi'an, China, 2017.*

**Purpose** Motion of the patient affects image quality in dental cone-beam imaging. While efforts are always made to minimize motion during the scan, relatively little attention has been given to methods of compensating for the motion during the reconstruction of the image.

**Method** In a previous study, we proposed an approach to iteratively estimate and compensate for rigid head motion within the reconstruction process for helical CT. This study reports on an extension of this method to mitigate the effect of the limited FOV in the dental scan. We assume the motion in a dental scan that we are dealing with is strictly rigid.

**Results** The new method was evaluated both in simulations and a phantom scan. The quality of the reconstructed images was improved substantially after motion compensation. The proposed approach eliminated most of the motion-induced artifacts in dental ROI imaging. Although some residual resolution loss was observed.

**Conclusions** The preliminary results indicate that the proposed motion correction approach is effective for dental CT scans, where the rigid motion is present.

**Personal contribution** The PhD student proposed the methodology, with contribution from Johan Nuyts. Simulation and phantom data were collected by the student. Software was implemented, evaluated and optimized by the PhD student, who also drafted the manuscript. The co-authors Johan Nuyts and Roger Fulton contributed to the editing of the manuscript.

## 7.1 Introduction

Patient motion is one of the main causes of visible image artifacts in oral and maxillofacial cone-beam CT imaging. Dental imaging most commonly uses cone-beam CT, which requires a longer scan time and thus increases the probability of patient motion during the examination, compared to clinical multi-row CT. For example some patients, in particular children could move their head during a scan, due to fear of the scanner movement. Also in practice, it is difficult to prevent aged patients with mental disease, e.g. Parkinson's disease from movement. In a study (Donaldson et al. 2013), it was found that about 18 % of the youth and 24 % of the aged subjects were likely to move in the scan, which induces motion artifacts in the reconstructed images.

The motion artifacts in the reconstructed image can degrade the image quality, adversely affecting diagnosis or treatment planning (Donaldson et al. 2013; Hanzelka et al. 2013; Pauwels et al. 2015; Spin-Neto et al. 2013; Spin-Neto et al. 2016). Even though sometimes the movement is too small to be noticed by human eyes, the reconstructed image can still suffer from a loss of resolution. Hence the resolution of the flat panel detector would not be the limiting factor of the image resolution but the motion is. Further problems arise when metal implants are present together with the movement (Nardi et al. 2015). All these may induce the retake of the scans, which inevitably causes additional radiation dose to the subjects.

Various efforts have been made to prevent patient motion during a scan. It is often suggested an examiner should instruct a subject to close their eyes and be prepared for the scanner movement prior to an acquisition. During a scan, patients are sometimes immobilized with a head strap, and/or a chin holder. However, solely relying on the hardware to fix the head might not prevent all possible movements (Hanzelka et al. 2013; Nardi et al. 2017).

Relatively little research has focused on methods to reduce motion artifacts in the reconstructed images for dental CT scans. One recent work demonstrates the potential to track the movement of the head using an optical camera (Spin-Neto et al. 2017). More approaches have been focusing on other cone-beam CT

systems or clinical multi-row CT systems. Similar to Spin-Neto et al. (2017), a motion detection approach was invented but for clinical head CT scans (Kim et al. 2015b), and the corresponding compensation was proposed. Some approaches detect the motion by tracking artificial or anatomical landmarks in the image or projections (Lu et al. 2002; Ritchie et al. 1996). Others minimize an image-based cost-function which is sensitive to motion artifacts to estimate the motion (Kingston et al. 2011; Kyriakou et al. 2008; Rohkohl et al. 2013).

Previously we have described an iterative method to estimate and compensate the head motion in clinical CT scans (Sun et al. 2016). In the present study, we extend that approach to dental CT imaging. In the following context, we assume the motion happens in a dental scan is strictly rigid. We will describe how the previous method has been adapted to overcome new challenges encountered in this application. The proposed approach is evaluated in both simulations and a phantom study, comparing motion-compensated reconstruction to reconstruction from motion-free data. Throughout the following context, we define the full field-of-view (FFOV) as the entire reconstructed region, ROI as the fully sampled region which is the same as the scan FOV, *background* as the region outside ROI and within the FFOV.

## 7.2  Methods

### 7.2.1  A revisit of previous approach

Our previously described approach performs rigid motion correction on clinical helical CT scans (Sun et al. 2016). That method assumes that the rigid pose (motion) of the measured object may be different for each projection view. The coordinates system are defined as in Fig. 7.1. A rigid transformation representing the object pose can be estimated (Motion Estimation in Fig. 7.2) by a 3D-2D registration process for every view. The translation perpendicular to the detector was neglected because estimating it was found to have negligible effect on the corrected image. The remaining five rigid parameters were estimated in a sequential way at each projection view. The sequence of the parameter estimation was translation first, then rotation. The newly estimated parameter values were used immediately when estimating the value of the next parameter. This sequential estimation of five motion parameters for all projection views completes the update of the rigid motion at the current iteration.

A compensation for changes in pose during the scan is applied in the reconstruction by incorporating the motion into the system matrix ("recon" in Fig. 7.2). Ordered Subsets Expectation Maximization (Hudson et al. 1994) was used as the reconstruction algorithm. Instead of moving the reconstructing image in every view, rigid motion compensation is done by considering a coordinate system fixed to the object and incorporating the motion (now associated to the source-detector pair) into the system matrix. This corresponds to an
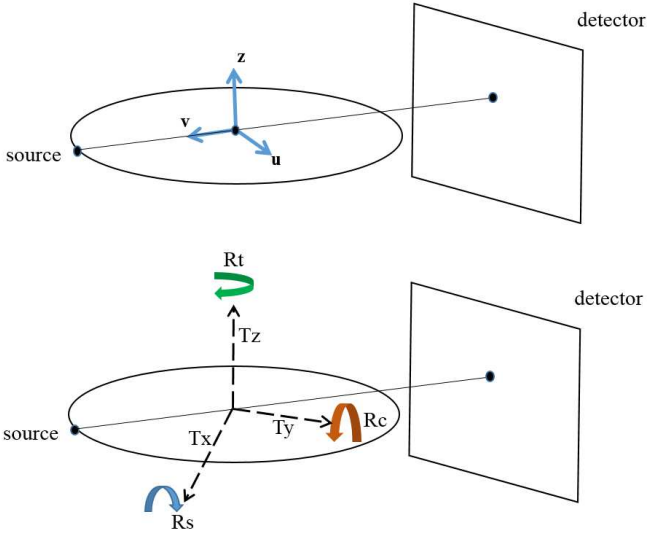
Figure 7.1: In one view, (a) the detector coordinate system (blue solid arrows) and (b) scanner coordinate system (black dashed arrows), the center of these two systems coincide with each other. Motion estimation is based on detector system. Motion compensation in all views is based on scanner system.

arbitrary 3D rigid motion of a virtual gantry around the object being scanned, created by the superposition of the inverse of the object motion on the helical trajectory.

The motion-corrected image and the motion estimate are alternately updated to increase the likelihood, and the iterations are stopped when the estimated motion seems to have converged. A multiresolution approach was applied to accelerate the computation. There is a resampling with a factor of two between adjacent levels. A similar multi-resolution approach can be also applied in the projection domain. The proposed approach has been shown to effectively suppress the motion artifacts in helical CT scans with different setups.

## 7.2.2 New challenge in dental ROI imaging

Some important differences exist between clinical multi-row CT and the cone-beam CT, which may affect ME/MC (motion estimation and motion compensation) on a dental scan. The most significant are the differences in axial and transaxial truncation. In a circular scan the constant axial FOV in dental cone-beam CT is expected to facilitate ME/MC. On the other hand, dental cone-beam CT typically uses transaxial truncation to reduce the irradiated volume, which is expected to adversely affect ME/MC. Specifically, the ME step is based on re-projection, requiring a FFOV reconstructed image,
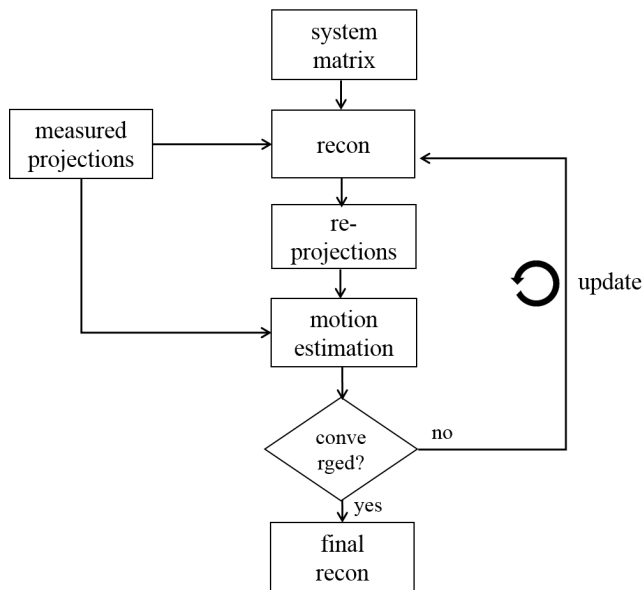
Figure 7.2: General Motion Estimation/ Motion Compensation (ME/MC) scheme in (Sun et al. 2016). One iteration of ME/MC involves 1 ME step and 1 MC step. One ME step attempts to adjust the object pose at each view to minimize the difference between the measured projections and the re-projected object. One MC step compensates for the motion during the scan in a reconstruction process, by incorporating the current motion estimates into the system matrix.

which is not available in an ROI scan. In addition, the MC step uses an iterative reconstruction, which also requires a FFOV reconstructed image during forward/back-projection. Hence insufficient information outside the fully sampled ROI in a reconstructed image could induce errors when using above the ME/MC scheme. These errors could be streak artifacts in the reconstructed image after every iteration of MC, and inaccurate estimated motion after every iteration of ME.

Another concern is that the information in the *background*, while not of clinical importance, is required by an iterative reconstruction algorithm. An analytical reconstruction algorithm such as FDK (Feldkamp et al. 1984) can restrict the computations to the ROI, making it very efficient for such applications. In contrast, when an iterative reconstruction algorithm is used, the entire object must be reconstructed. Since our current motion compensation approach relies on iterative reconstruction, there is value in minimizing the amount of computations devoted to the *background*, without compromising on reducing the motion artifacts.

### 7.2.3 Improved Patch-based ME/MC

In this study, we propose a patch-based ME/MC. By applying this technique, we believe the two concerns in the last section can be mitigated.

**Patch-based reconstruction**

Let us first introduce the reconstruction algorithm used in this paper. We use a Maximum Likelihood algorithm to perform the reconstruction. Ignoring the polychromatic sources and scattering effect, the Poisson log-posterior function of the attenuation is:

$$\Phi(\mu) = y_i \ln \hat{y}_i - \hat{y}_i - \lambda R(\mu) \tag{7.1}$$

$i$ is the index of the projection line, $y_i$ is the measured transmission scan at $i$, $\hat{y}_i$ is the estimated transmission scan at $i$ computed from the current reconstructed image $\mu = \{\mu_j\}$, where $\mu_j$ is the linear attenuation coefficient at voxel $j$. $R(\mu)$ is the logrithm of the penalty, multiplied with $-1$ to turn it into a log-prior, and $\lambda$ is the weighting factor. By maximizing the above function, one is able to find the optimal attenuation image iteratively. For example, when no prior information is available, the update function of MLTR is as follows (Nuyts et al. 1998):

$$\mu_j^{new} = \mu_j + \frac{\sum_i a_{ij}(\hat{y}_i - y_i)}{\sum_i a_{ij}(\sum_h a_{ih})\hat{y}_i} \tag{7.2}$$

where $a_{ij}$ is the intersection length of projection line $i$ with voxel $j$. Motion correction can be incorporated by adjusting the system matrix on-the-fly according to the known rigid motion.

Patch-based reconstruction approaches have been proposed for various applications in CT imaging (Fessler et al. 1997; Van Slambrouck et al. 2012; Yu et al. 2006). The idea is that a reconstruction volume can be divided into interesting patches and not-so-important patches. For each of these patches a different resolution model can be defined. The voxel weighting factor plays an important role in convergence of the attenuation values at each voxel. The patches are updated sequentially, each patch is considered as a group of pixels in a grouped coordinate algorithm. Sequentially updating groups of pixels is known to improve convergence, e.g. in the modified update equation of MLTR (Eq. 7.3), the denominator of the update steps will be smaller when the area of the updated patch is smaller.

$$\mu_j^{new} = \mu_j + \frac{\alpha_j \sum_i a_{ij}(\hat{y}_i - y_i)}{\sum_i a_{ij}(\sum_h a_{ih}\alpha_h)\hat{y}_i} \tag{7.3}$$

where

$$\begin{cases} \alpha_j = 1 \text{ if } j \in \text{patch} \\ \alpha_j = 0 \text{ if } j \notin \text{patch} \end{cases}$$

is the voxel weighting.

**Patch-based ME/MC**

Patch-based ME/MC used above described Patch-based reconstruction. To implement a patch-based ME/MC, we need to define two patches for dental ROI imaging (Fig. 7.3a). We first performed an initial FFOV FDK reconstruction, and then defined one high-res patch and one low-res patch by thresholding and dilating. The resulting high-res patch contains the teeth inside the fully sampled ROI, where a smaller voxel size is used; the resulting low-res patch comprises the remainder of the FFOV, where a coarser sampling is used.

Specifically, both ME and MC need to be adjusted for the patch-based implementation. For ME, the re-projection process involves the forward projections with different resolutions for different patches. For MC (iterative reconstruction), each update of the image can be divided into 2 steps (Fig. 7.3b) a first update performed only in the high-res patch, and a sequential update performed in low-res patch only:

(1) First update on high-res patch

We want the high-res patch to contain the high contrast structures, i.e. the teeth and the surrounding structures inside the fully sampled ROI, because they provide the most useful information for ME. During a reconstruction in MC (Fig. 7.2), the first update was limited to voxels within the high-res patch using Eq. 7.3. L1-norm total variation (TV) regularization (Sidky et al. 2008) was applied in the iterative reconstruction to preserve the high-frequency structures while reducing the streak artifacts surrounding the teeth in the high-res patch.

(2) Sequential update on low-res patch

Following the first update in the high-res patch, a sequential update was performed for the low-res patch. The voxel size in the low-res patch is 4 times larger than the one in the high-res patch. Eq. 7.3 performed updates for low-res patch, within which voxels are updated.

### 7.2.4   Final reconstruction

On completion of the iterative Patch-based ME/MC process, an initial corrected image is available. In this image only the teeth (high-res patch) are with fine resolution. To produce an image with diagnostic quality, a final fine-resolution reconstruction in the FOV is still required. In the following simulations, iterative reconstruction was used in the final reconstruction and patched-based reconstruction was used to accelerate the iterative reconstruction. The patches were defined differently from the ones in the estimation. The high-res patch contained the scan FOV (red circle in Fig. 7.3b), while the rest of the FFOV is low-res patch. The update strategy was the same as in the estimation. To accelerate this reconstruction, the starting image was created from an FDK reconstruction with the estimated motion. For this purpose, an approximate circular FDK algorithm was implemented, where a first order motion compensation is obtained by taking the motion for each view into account in the back-projection step. In contrast, in the phantom study, an FDK reconstruction image was produced as final reconstructed image, which is restricted to the scan FOV only. This is because of the fact that the motion to be estimated in this study is small, and for a real scan an analytical reconstruction is often much faster than an iterative reconstruction.

## 7.3   Simulations

### 7.3.1   Phantom and motion

A digital phantom (Fig. 7.4) was used in all simulations. It was discretized into an image of $256 \times 256 \times 70$ voxels with a voxel size of $1.0 \times 1.0 \times 1.0$ mm$^3$. A detector with $200 \times 80$ detector pixels of $1.0 \times 1.0$ mm$^2$ was simulated to create

(a)



high-res patch
in white

low-res patch
in black

(b) 1. first update on high-res patch   2. then update on background patch
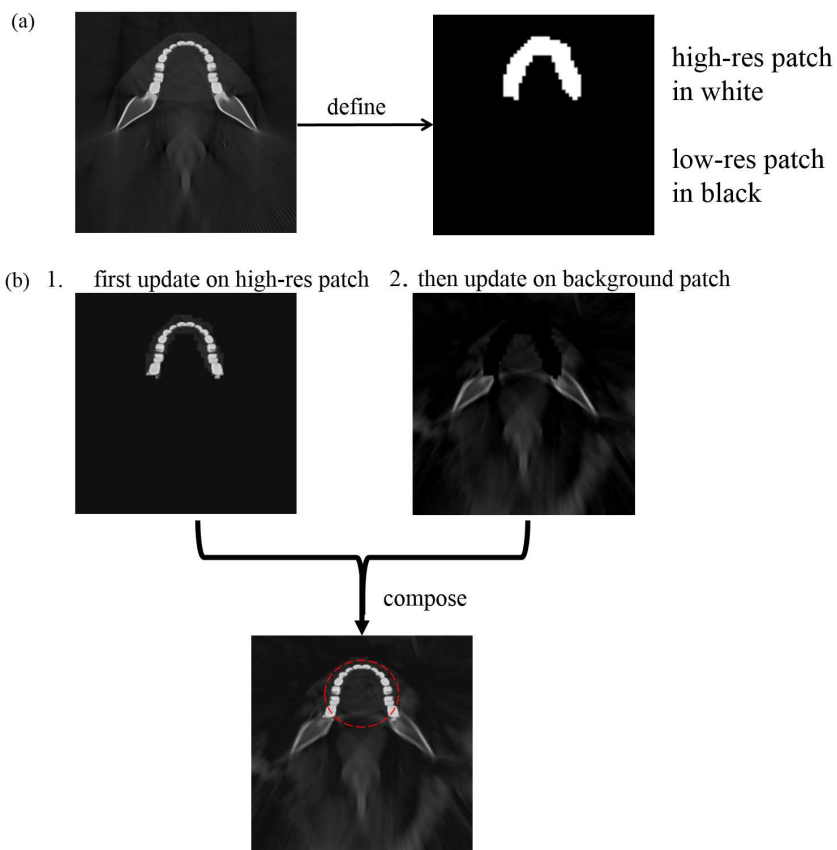


compose



Figure 7.3: (a) The patch definition for dental ROI imaging. (b) The patch-based reconstruction of a single iterative process in MC. A first update was only performed in the high-res patch, and a sequential update was performed in the low-res patch. The red circle indicates the scan FOV.

the transaxially truncated projections in dental imaging. The distance between the X-ray source and the detector was 575.0 mm, the distance between the detector and the rotation center was 216.5 mm. The scan FOV diameter was about 125.0 mm.

Two segments of rigid head motion of a volunteer recorded over a 5 s period (Fig. 7.5) were applied to the digital phantom while cone-beam projections were computed. The total simulated scan duration was also 5 s. The total number of views was 360 covering 1 full rotation (360°). The motion was simulated by applying the inverse motion to the CT-detector gantry for each individual view. Like for clinical multi-row CT, we have the assumption that the motion within one cone-beam projection view is negligible. Hence there was no motion simulated within one projection view.
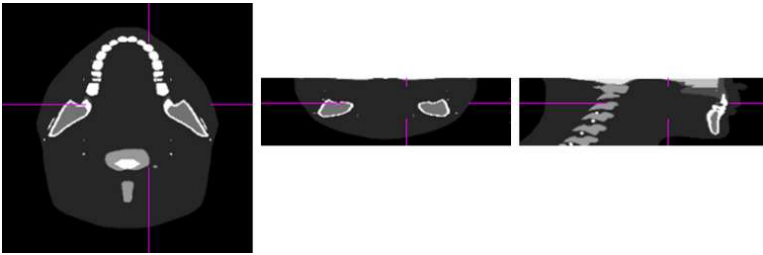


Figure 7.4: The digital phantom used in the simulations. From left to right: selected transaxial, coronal and sagittal slice through the phantom.

## 7.3.2 Design of experiments

From a set of simulated motion-contaminated projections, we computed the reconstructed images from four different experiments: one with the compensation using the exact simulated motion, one without any compensation, one with ME/MC and one with Patch-based ME/MC. We aimed to compare the image quality and computation time for all images. Details of how these images were obtained are listed below:

(1) A reference image was obtained from an MLTR reconstruction with the exact simulated motion taken into account, starting from an initial-corrected FDK image. Distance-driven projection is used for interpolation during the forward and back-projection (De Man et al. 2004). The iterative reconstruction parameters were: 4 reconstruction iterations, 40 subsets, voxel size 1.0×1.0×1.0 mm$^3$.

(2) An MLTR reconstruction was performed, starting from an initial FDK reconstruction. No motion compensation was applied. The iterative reconstruction parameters were the same as in (1).

(3) The total number of ME/MC iterations was 40 (Fig. 7.2). In one MC, the patched MLTR algorithm updated the FFOV image (4 reconstruction iterations
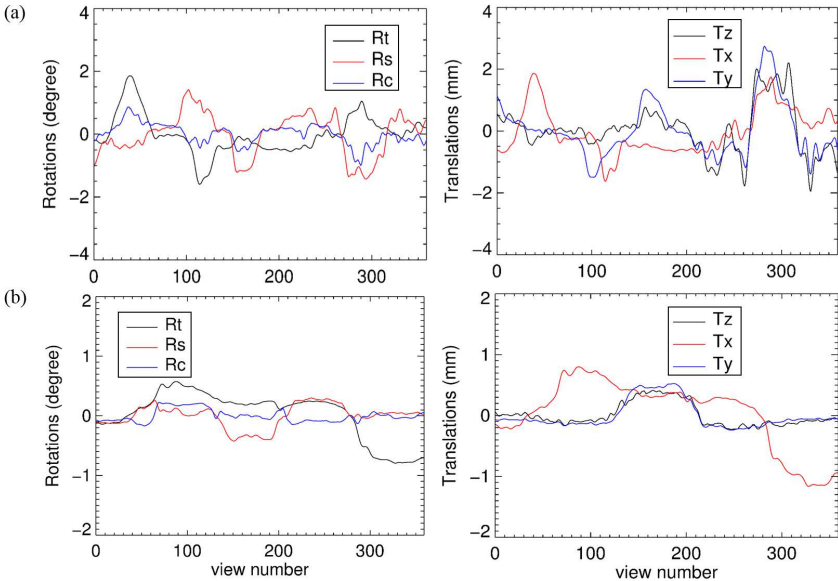
Figure 7.5: The recorded rigid motion segments (a) and (b) which were used to generate the motion-contaminated projections. The motion themselves and details of how it was recorded can be found in (Kim et al. 2015b).

40 subsets). The resolution in the high-res patch is four times higher (along each direction) than the one in the low-res patch. A final MLTR reconstruction was performed with the final estimated motion taken into account, starting from an initial-corrected FDK image.

(4) The total number of iterations of ME/MC was 40. In one MC, the patched MLTR algorithm updated the FFOV image (4 reconstruction iterations 40 subsets). The high-res patch are updated with TV regularization. In one ME, re-projection was done by combining the forward projections of the two patches. A final MLTR reconstruction was performed with the final estimated motion taken into account, starting from an initial-corrected FDK image.

## 7.3.3 Results

Fig. 7.6 shows the resulting images from the simulation experiments. For both simulations with motion from Fig. 7.5a and Fig. 7.5b, compared with the reference image, the image without any compensation was clearly contaminated by motion artifacts (red arrow). After applying ME/MC to the measured data, most of the artifacts were suppressed (after 15 iterations of ME/MC, the improvement on motion estimation stopped). But there was still some resolution loss. Patch-based ME/MC reduced this resolution loss and did so at lower computation time with the same number of iterations. This is confirmed

in the plot of convergence in Fig. 7.7.
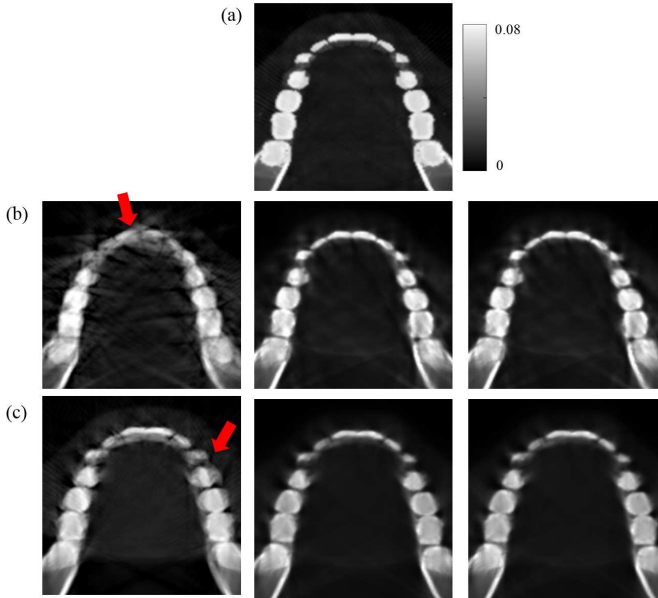


Figure 7.6: The final reconstructed images in the simlation studies. (a) reference image. (b) results from the simulation with motion in Fig. 7.5a. (c) results from the simulation with motion in Fig. 7.5b. From left to right in (b) and (c) — the image without compensation; the image with ME/MC; the image with Patch-based ME/MC.

## 7.4 Phantom study

### 7.4.1 Design of the study

Phantom scans were performed on an Accuitomo 170 scanner (J Morita Mfg. Inc., Kyoto, Japan) in Oral and Maxillo-facial Surgery Department of the UZ Leuven. The anthropomorphic phantom used in this study is the Sectional Head Phantom SK150 (Phantom Laboratories, Salem, NY, USA). This phantom has an internal air cavity representing the oral, pharynx and trachea anatomy. The scan setup is shown in Fig. 7.8. The scan was a full rotation scan with 512 views, and lasts for about 30 s, within which 10 s is the irradiation time. Other scan parameters were: detector size $940 \times 748$; detector pixels pitch of $0.2 \times 0.2$ mm$^2$; FOV diameter 140 mm; distance between the X-ray source and the detector 842.0 mm; distance between the detector and the rotation center 302.0 mm.

A movement scan was first performed. Prior to that scan, the phantom was
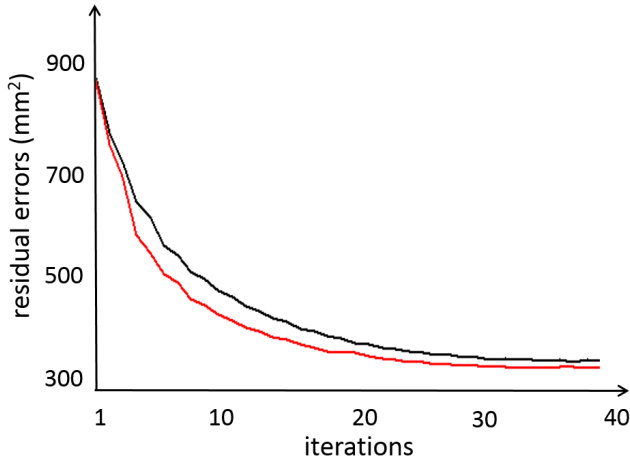
Figure 7.7: Restoration of the image quality by ME/MC (black) and Patch-based ME/MC (red) for simulation with motion in Fig. 7.5a. The residual ROI errors (squared difference between corrected and the reference image) were measured. With 40 iterations, the total time of ME/MC was 2h13m, the time of the Patch-based ME/MC was 1h15m.

attached to a string and placed at the center of the scanner FOV. The rigid motion was induced by pulling a string attached to the phantom during the middle of the scan - 5 s after the start of the scan, the examiner pulled the string from outside the examining room. The induced motion was expected to be large enough to create artifacts in the reconstructed image. After the movement scan, a static scan was performed to produce a reference image. Scan parameters in this scan remained the same as the ones in the movement scan.

Three images were generated from above the two scans:

(1) Machine reconstruction of a static scan was exported and used as the reference image. The reconstruction image size was $561 \times 561 \times 401$, pixel size was $0.25 \times 0.25 \times 0.25$ mm$^3$;

(2) Machine reconstruction of the moving scan was also exported. The dimension of this image was the same as one in (1). No motion compensation was applied;

(3) Raw data were exported for the movement scan, and from that motion estimation was performed. Different from simulations, the views possibly with movement were first identified by checking the projections visually, and the subsequent motion estimation was only performed for those views. Then as in Section 7.2, Patch-based ME/MC performed the motion estimation by updating the motion and the image alternately (11 iterations). As the motion in

Figure 7.8: Phantom study setup. An anthrophonic phantom was positioned at the center of the scanner FOV.

the phantom study was small, final motion compensation was performed in an FDK reconstruction with the same resolution as in the machine reconstruction. The dimension and the pixel size of the reconstructed image were the same as the ones in (1).

### 7.4.2 Results

Fig. 7.9 shows the selected planes from the resulting images in the phantom study. Compared with the reference image, the image without any compensation was clearly inferior and contaminated with artifacts. After applying the proposed approach to the raw data, most of the artifacts were eliminated (after 8 iterations of patched ME/MC and final reconstruction). The total running time is about 2 hours, during which motion estimation took 1.8 hours. There are still some residual streaks and blurring, currently we are finding out the reason of that.



Figure 7.9: Left is a 2D transaxial plane in the reference image. Middle is the same plane in the uncorrected image. Right is the same plane in the corrected image, where artifacts are much less than the middle one. Note that we have also performed our own reconstruction for the static scan (not shown), and the resulted image looks quite similar to the machine reconstruction.

## 7.5 Discussion

In this manuscript, we proposed a rigid motion estimation and compensation approach for dental cone-beam CT imaging with transaxial truncation, the implementation of which only requires the measured raw data. Since no additional measurements are needed, it can be applied retrospectively to any dental scans. Note that the motion in the phantom scan was assumed and modelled as rigid motion of an object across views. In some more complicate scenarios, a different motion model may be required. For example, non-rigid movement of tissues could be present due to swallowing, or different moving patterns between the upper and lower jaws might exist. The proposed approach is expected

to fail in such cases. How to deal with scans in the presence of such movements is beyond the scope of this manuscript.

The proposed approach works reasonably well despite the severe artifacts outside the high-res patch, where the reconstruction is handicapped by a limited angle problem. It has been previously shown that the high-res patch can in principle be reconstructed exactly if it contains a portion of air background (intensity known to be zero) (Defrise et al. 2006), which is often the case in dental imaging. Moreover, even in the *background*, spatial frequencies are better reconstructed if they contribute more information to the measured projections (typically edges which are parallel to the projection lines). This implies that the reconstructed low-res patch still contains the relevant edges needed to align measured and forward projected views, which is the essence of the original ME/MC scheme.

The proposed motion correction is not perfect (as in Fig. 7.9). One reason, as described previously, is that *background* cannot be reconstructed exactly, which may propagate the errors of non-exact reconstruction into ME. Another potential cause of the inaccuracy is that we assume the movement only happen in between views. When any movement is fast enough to happen within one projection view, the proposed approach may not be able to compensate the effect of that. Given the fact that the exposure time of one projection view in cone-beam CT is 200-500 ms, such movement within views might not be negligible.

Unlike a clinical helical CT-scan, a normal dental scan has a smaller number of views (300-700) acquired in a full or half rotation. Hence the computation requirement to apply the compensation in dental imaging is less demanding. Currently, the entire Patch-based ME/MC process takes $\sim 2$ hours (1.8 hour ME/MC iterations and 0.2 hours final reconstruction) in the phantom study. The processing time on a real patient scan is expected to be similar. By introducing proper acceleration techniques, the processing time can be significantly reduced. However, when the motion to be compensated is large, one will have to introduce an iterative algorithm to the final reconstruction, or to implement a motion-sensitive analytical reconstruction algorithm.

Various factors could affect the motion compensation effect in a real patient scan and require further examination. For example, (1) a smaller size of the FOV captures less information in measurement, which may degrade the motion estimation results; (2) offset scan mode is sometimes available on some scanners. With such mode, measure projections are truncated in all views, allowing a small detector extend to cover large FOV. The truncated projections may present a challenge for motion estimation; (3) It is expected that a half scan typically suffers more cone-beam artifacts but less motion artifacts due to the shorter scan time, compared with a full rotation scan. Whether using a half scan mode would affect ME/MC or not remains to be checked; (4) Last but not the least, together with motion, presence of dental implants could complicate the artifacts in a reconstruction image. A metal artifacts correction technique

would be needed to combine with the proposed motion correction technique, to simultaneously mitigate the motion and metal artifacts.

## 7.6 Conclusion

In this preliminary study, we proposed an approach to compensate the rigid motion artifacts in dental ROI imaging. Results from simulations and a phantom study are presented. The improvement on the image quality was encouraging and further testing on clinical data is warranted.

## Acknowledgement

# Chapter 8

# Estimation of local data-insufficiency in motion-corrected helical CT

**Purpose** Previously we have proposed a reconstruction algorithm which corrects for known rigid motion in helical CT. This work describes a method to determine data-insufficiency of helical CT data affected by rigid object motion. We propose a local measure that quantifies the degree to which Tuy's completeness condition is violated in each voxel. This measure identifies regions for which artifact-free reconstruction is not assured.

**Method** For every voxel, a local data-insufficiency measure is computed. We call the resulting image the Tuy map. Its values range from 0 to 1, where high values indicate data-insufficiency. As shown by classic theory, exact reconstruction is not possible where the Tuy map contains high values. The predictions based on this Tuy map were verified with simulated helical-CT data, where the object moved during the scan and the rigid motion was correctly taken into account during reconstruction. We also analyzed the reconstruction from an actual motion-corrected CT-scan of a moving phantom.

**Results** For motion-free helical scans, the Tuy map was close to zero everywhere and the reconstructions were artifact-free. Rigid motion induces an effective source trajectory (with respect to a stationary patient) which, combined with axial or even transaxial truncation, can cause incomplete sampling. In simulations with severe motion or transaxial detector truncation, the Tuy map contained high values and the reconstructions suffered from artifacts. In the phantom scan, the combination of a high pitch and severe motion created artifacts which the Tuy map successfully indicated. In all cases, the Tuy map indicated all regions with incomplete sampling which were prone to reconstruction artifacts. However, we also contrived a special case, where exact reconstruction was not assured although the local Tuy's condition was satisfied.

**Conclusions** The proposed approach provides a useful measure of data-incompleteness, which can be used to verify the validity of motion-corrected helical CT scans. The method is general and could also be useful for other tomographic problems for which no exact data-sufficiency measures are available.

**Personal contribution** The PhD student proposed the methodology, with contribution from Johan Nuyts and Rolf Clackdoyle. Phantom data were collected with the help of Jung-Ha Kim. Simulation was performed by the PhD student. Software was implemented, evaluated and optimized by the PhD student, who also drafted the manuscript. The co-authors Rolf Clackdoyle, Johan Nuyts, Roger Fulton and Jung-Ha Kim contributed to the editing of the manuscript.

## 8.1 Introduction

Motion is one of the main causes of resolution loss and artifacts in head CT imaging. We have previously developed a reconstruction method that corrects for known rigid motion in helical CT scanning of the head (Nuyts et al. 2011). The motion can be measured using an external, marker-based motion tracking device (Kim et al. 2015b, 2016) or it can be derived from the CT-data themselves (Sun et al. 2016). The motion correction is achieved by incorporating the known rigid motion into the system matrix of an iterative reconstruction algorithm.

Our simulation and phantom experiments indicate that with appropriate motion correction, the reconstructed images are generally artifact-free. However, in some cases the motion-corrected images do have artifacts, even if the exact motion model is used during the reconstruction (Kim et al. 2016). We have provided evidence that this is due to data-insufficiency - i.e. in some cases the combination of head motion and scanner rotation limits projection sampling to the extent that artifact-free reconstruction is no longer assured at all points

within the object. This is purely due to a limitation of the data, rather than the motion compensation scheme.

We assume all motion involved in this study are rigid. Patient motion during the scan effectively changes the acquisition source trajectory: in a coordinate system attached to the object, the CT detector and source can follow an arbitrary trajectory, created by the combination of the rigid patient motion with the ideal helical trajectory. The intended helical trajectory provides sufficient data for "exact" reconstruction, but this is not guaranteed for the modified trajectory created by the additional patient motion. "Exact" here means that in the ideal continuous case, the trajectory produces data that are sufficient for accurate and stable reconstruction. Experience shows that when theoretical analysis predicts exact reconstruction, accurate reconstructions are obtained in practice with analytical and/or iterative algorithms, in spite of the unavoidable discretization (to model the finite number of measurements) and in spite of deviations from the ideal model, such as noise, scatter, etc. provided these are not excessive.

Consequently, a method is needed to assess the inherent data-sufficiency of the motion-corrected CT trajectory that is independent of the choice of reconstruction algorithm. This method would give a warning when the CT-scan does not provide sufficient data without having to reconstruct the images. It is important to identify regions of data-insufficiency, because artifacts may not always be recognized as such and may adversely affect the diagnosis. In addition, such a method would provide a tool to study how the combination of typical patient motions with different CT-scan parameters (rotation speed, pitch, axial detector size etc.) affect data-sufficiency. This tool would facilitate the definition of CT acquisition protocols that are robust to patient motion (Kim et al. 2016). Finally, it would also be a useful tool for quality control: if artifacts are observed that cannot be attributed to data-insufficiency, then the imaging procedure has a problem that must be identified and corrected.

However, the assessment of data-sufficiency (or insufficiency) in motion-corrected helical CT faces two problems. First, for cone-beam CT with truncation and an arbitrary source trajectory, there is currently no complete theory that can tell whether a particular voxel can be reconstructed exactly or not (Clackdoyle 2005). Second, even with untruncated data, the existing analytical methods only provide a binary answer, whereas for practical use, it would be preferable to obtain a degree of data-insufficiency. These two issues are discussed in the next two paragraphs.

Orlov (1975) derived a data-sufficiency condition for untruncated parallel-beam tomography. Tuy (1983) extended this to a data-sufficiency condition for untruncated cone-beam tomography. Metzler et al. (2003a) have identified a geometrical connection between the Orlov and Tuy sampling criteria. In that work they proposed an algorithm to compute the largest completely sampled region for arbitrary orbits in cone-beam and parallel-beam tomography. The algorithm assumes untrucated projections and verifies for each voxel if it be-

longs to the completely sampled region or not. Unfortunately, in helical CT, all projections are truncated due to the limited axial detector size, and transaxial truncation exists in an ROI scan. For helical trajectories with axial truncation only, data-sufficiency theory has been established (Kudo et al. 2004; Wang et al. 2007). However, there is currently no data-sufficiency condition for truncated projections that is general enough to deal with an arbitrary trajectory, such as the effective trajectory caused by rigid patient motion. By inverting Tuy's condition, Finch (1985) established a local data-insufficiency condition that applies to untruncated and truncated projections. This will enable us at least to identify locations where the arbitrary source trajectory definitely created data-insufficiency, but unfortunately, it may fail to identify all such locations. One aim of this contribution is to verify how useful this local Tuy's condition is as a predictor of artifacts and in which cases it may fail.

In addition, as previously mentioned, where analytical data-sufficiency conditions can be applied, they provide a binary answer: at each voxel location, exact reconstruction is either possible or not. In practice, it is preferable to have a method that provides a degree of insufficiency. As an example, Tuy's condition implies that with circular cone-beam tomography, exact reconstruction is only possible for the central plane. Experience shows that in practice, excellent reconstructions are also obtained for other nearby planes; the so-called cone-beam artifacts only become problematic for planes far from the central one. This agrees with the intuitive understanding that Tuy's condition is "more violated" in planes more distant from the central plane. Practical methods to determine the degree of sampling insufficiency have been proposed for various geometries. Metzler et al. (2003b) proposed a metric of measuring sampling sufficiency for a pinhole SPECT (single-photon emission computed tomography) system. Clackdoyle et al. (2001) provided a quantitative prediction about data-sufficiency in cone-beam reconstruction for a hypothetical pinhole SPECT system for breast imaging. Liu et al. (2012) proposed a completeness map for several candidate cardiac CT system designs.

Also analytical algorithms could be used to study data-insufficiency. Analytical algorithms similar to filtered backprojection make strong assumptions about the trajectory of the X-ray source. In contrast, analytical reconstruction algorithms based on chords (Pi-lines) can reconstruct images from scans along irregular trajectories (Ye et al. 2005). Unfortunately, the requirements of these chord-based methods are sufficient but not necessary for exact reconstruction. E.g., for particular voxels, severe motion could break up the trajectory into disjoint parts, such that these voxels are not on a chord, while exact reconstruction would still be possible (Clackdoyle et al. 2010). Yu et al. (2012) developed a BPF algorithm that is capable of reconstructing also voxels not lying on a chord. However, using such methods to verify if a particular point can be reconstructed or not requires a rather extensive analysis. In addition, the method would then produce a binary answer, not a continuous value assessing the degree to which Tuy's condition is violated.

In this paper, we propose a measure to quantify the degree to which Tuy's condition is violated in every voxel for a CT-system with an arbitrary trajectory. The method is general, but our focus is on motion-corrected helical CT using a clinical system. The method is specific: voxels found to violate the local Tuy's condition definitely pose a reconstruction problem (Finch 1985) but its sensitivity is not perfect (some regions suffering from data-insufficiency may not be detected). The method is independent of the reconstruction algorithm, as it identifies voxels for which the data are insufficient based on theory. We evaluate our method with an iterative reconstruction algorithm. We verify that artifacts appear where predicted by the method. We also study cases where the method is expected to fail, i.e. where the reconstruction problem is not unique due to data-insufficiency even though the local Tuy's condition is satisfied.

## 8.2    Materials and Methods

### 8.2.1    Voxel-based Tuy map

Tuy provided a sufficient condition for exact cone-beam reconstruction from untruncated projections: "if on every plane that intersects the object, there exists at least one cone-beam source position, then one can reconstruct the object" (Tuy 1983). As explained in the Introduction, we cannot directly apply Tuy's condition to measure projection insufficiency for (motion-corrected) helical CT, due to the inevitable projection truncation.

Finch proved the converse of Tuy's condition: "if there is a plane which contains no measurement lines passing through a particular voxel, then stable reconstruction is not possible for that voxel" (Finch 1985). This condition provides theoretical support for our incompleteness measure for arbitrary cone-beam trajectories with truncated projections. Based on Finch's result, we define a voxel-based measure of data-insufficiency. We call this the local Tuy value, and refer to the corresponding image as the Tuy map.

The overall procedure to obtain the Tuy map is as follows. To approximate the continuous model, the size of the voxel is chosen "small enough", i.e. smaller than the detector pixel size. For every voxel, planes passing through the center of that voxel are considered. For every voxel, we also define a set of measured projection lines: we examine all the source positions of the CT acquisition, and for each source position on the effective trajectory, the line containing the source position and the center of the voxel is considered. If that line intersects the detector, then we consider this line as a measured projection line.

A plane through a specified voxel can be represented by its unit normal vector, and the measured projection lines through the voxel by the unit vectors in the directions of the lines. The absolute values of the dot products of the projection line vectors with the plane normal vector are computed, and the minimum is

stored for each plane. The local Tuy value for the voxel is finally calculated as the maximum of the stored values across all planes. This procedure finds for each voxel the plane that most severely violates the local Tuy's condition, and quantifies that violation by examining the angle between the plane and the "most parallel" projection line. If the line is in the plane (intersection angle is zero), the value is zero. The procedure is described in more detail in Fig. 8.1, in which step 2 involves sampling of a unit hemisphere (Peterson et al. 2010).

The local Tuy values range from 0 to 1, a higher Tuy value in a particular voxel indicates that the local Tuy's condition is violated more severely within that voxel. A value of zero indicates that all planes through the voxel contain at least one measured projection line.

To clarify the meaning of the Tuy value, consider a set of 2D parallel-beam projections acquired with an angular coverage $[0, \alpha]$, where $\alpha$ varies from 0 to $2\pi$. It is known that the sampling is complete when $\alpha$ is in $[\pi, 2\pi]$, while for $\alpha$ in $[0, \pi)$, the sampling is incomplete. In addition, it has often been observed that the limited angle artifacts become worse when the angular coverage $[0, \alpha]$ is further reduced. In this 2D case, the planes considered for the Tuy's condition reduce to lines (see Fig. 8.2). It is easy to verify that the "Tuy line" with the largest minimum dot product $|\vec{l} \cdot \vec{n}|$ makes an angle $(\pi - \alpha)/2$ with the x-axis when $\alpha \in [0, \pi)$. Therefore, the Tuy value for all voxels in the field of view equals $|\vec{l} \cdot \vec{n}| = \sin((\pi - \alpha)/2)$ if $\alpha \in [0, \pi)$ and zero elsewhere. Fig. 8.3 shows a plot of the Tuy values. For $\alpha = 72°$, $144°$ and $180°$, sinograms of a 2D spheres phantom have been simulated and reconstructions with MLEM were made, illustrating that artifact severity increases with increasing Tuy value.

This approach has two sources of discretization and associated discretization errors. The first one is the discretization created by only considering source positions corresponding to actual CT measurements. Since a CT-scan typically contains thousands of views per rotation, the effects of this discretization are very small, and we found that useful Tuy maps could be obtained even with a reduced sampling of a few hundred samples per rotation. The second discretization is determined by the number of samples on the unit hemisphere. This number can be chosen arbitrarily, in our experience 500 samples are sufficient to obtain useful Tuy values. The method is not affected by detector discretization (it only uses the detector boundary to verify if a projection line intersects the detector), nor by discretization of the image into voxels (the Tuy value can be computed everywhere, our choice to only compute it at voxel centers is arbitrary).

## 8.2.2 Scanner geometry and simulation

For different simulation experiments, helical scans were simulated for the geometry of the Siemens Definition AS CT scanner and Siemens Sensation 16

**1.** Find all projection lines $\{\vec{l}\}$ passing through the voxel.
    **for all** projection angles/views **do**
        -apply the inverse motion to projector
        -calculate the source position $O$
        -calculate the position of detector corners
        $C1, C2, C3, C4$
        -calculate the intersection point $I$ on the detector
        **if** $I$ is located inside detector surface **then**
            **return** $\vec{l} = \vec{OI}$
        **end if**
    **end for**
**2.** Find all unit normal vectors $\{\vec{n}\}$ representing planes through the voxel, by uniformly sampling half of a unit sphere.
    **for all** sampling points **do**
        get the sampling point coordinate $S$
        **return** $\vec{n} = S$
    **end for**
**3.** Compute Tuy value from worst plane.
    normalize the $\{\vec{l}\}$
    **for all** $\vec{n}$ in $\{\vec{n}\}$ **do**
        **return** $m_{\vec{n}} = \min_{\vec{l}} \left| \vec{l} \cdot \vec{n} \right|$
    **end for**
    **return** $localTuyvalue = \max_{\vec{n}} \{m_{\vec{n}}\}$

Figure 8.1: Pseudo-code representation of the voxel-based Tuy value computation.
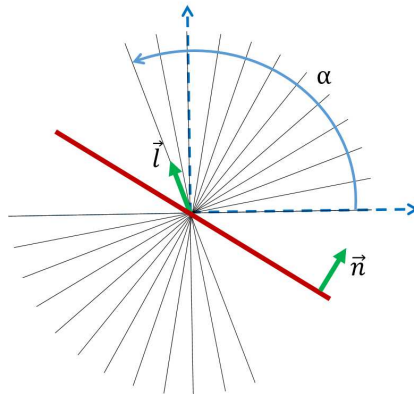


Figure 8.2: Example of 2D imaging with limited angle tomography $\alpha < \pi$. The projection lines available for a particular voxel are shown. For the plane shown in red, the dot product between its normal $\vec{n}$ and the projection line is minimum for the indicated projection $\vec{l}$. The indicated plane is the one that has the largest minimum dot product $|\vec{l} \cdot \vec{n}|$.
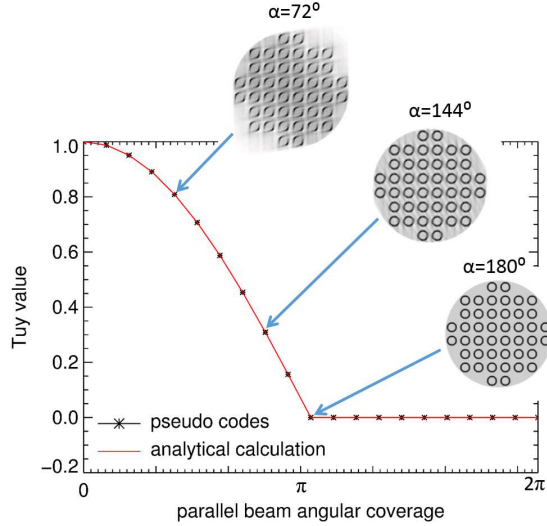
Figure 8.3: Red line represents the analytical calculation of the Tuy values at one voxel for parallel-beam geometries with angular coverage $[0, \alpha]$, where $\alpha$ varies from 0 to $2\pi$. The black star dots are the Tuy values calculated according to pseudo codes. The three images are from the corresponding 2D reconstructions when $\alpha = 72°$, $144°$ and $180°$ respectively.

scanner (Siemens Medical Solutions USA, Inc., Malvern, PA). In addition, a phantom scan was performed on a Siemens Sensation 16 scanner (incorporated in a PET/CT system). A sketch of the system is given in Fig. 8.4. The scan parameters used in different studies can be found in Table 8.1.

In the simulations, we introduced a geometric mismatch with the forward model used by the image reconstruction, by upsampling both the object and the detector by a factor of 2 in all directions when generating the projections. We assumed uniform blank scans, monochromatic radiation and ignored scatter in all simulations, since we did not want any confounding effects when evaluating the Tuy map.

When motion was present, it was simulated by applying the inverse motion to the CT-detector gantry for each individual view. For some simulations, the motion was based on recorded volunteer head motions, for others some (highly artificial) motion patterns were synthesized.

## 8.2.3   Phantom used in simulations

For this study two software phantoms were created. The first phantom (Fig. 8.5, called the multi-sphere phantom, consisted of a large cylinder filled with small hollow spheres. This ensured that it had sharp edges in all directions, such
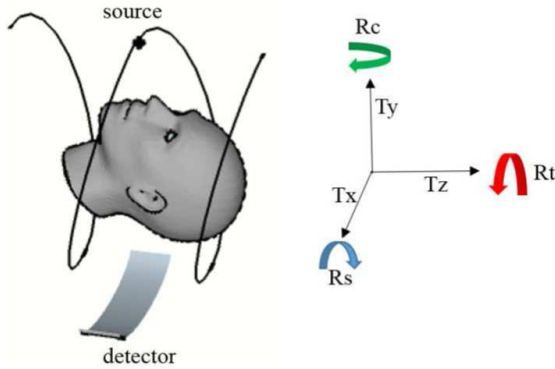
Figure 8.4: The X-ray source moves in a helical trajectory. The six degrees-of-freedom rigid motion are shown in the given scanner coordinate system. $T_z$ is the translation along the z-axis (bed direction), $T_x$ is the translation along the x-axis, $T_y$ is the translation along the y-axis. $R_t$ is the rotation around the z-axis, $R_s$ is the rotation around the x-axis, $R_c$ is the rotation around y-axis.

Table 8.1: Scanning parameters settings

|  | Configuration 1 (Section 8.3.1, 8.3.2, 8.3.3) | Configuration 2 (Section 8.3.4) | Configuration 3 (Section 8.3.5) |
|---|---|---|---|
| Scanner model | Definition AS | Sensation 16 | Sensation 16 |
| Tube voltage (kVp) | N/A | 120 | N/A |
| Tube current (mA) | N/A | 150 | N/A |
| Rotation time (s) | N/A | 0.5 | N/A |
| Pitch | 0.8 | 1.0 | 1.0 |
| Angles per rotation | 500 | 1050 | 500 |
| Collimation (mm) | $32 \times 1.2$ | $16 \times 0.75$ | $16 \times 0.5$ |
| Flying focus | off | off | off |
| Reconstruction pixel size (mm$^3$) | $2.0 \times 2.0 \times 1.0$ | $1.0 \times 1.0 \times 1.0$ | $1.6 \times 1.6 \times 1.0$ |
| Dimension | $160 \times 160 \times 120$ | $512 \times 512 \times 285$ | $200 \times 200 \times 120$ |
| Reconstruction updates | 5 iterations, 20 subsets | 6 iterations, 40 subsets | 50 iterations, 20 subsets |

that creation of reconstruction artifacts was likely wherever data-insufficiency occurred. The spheres had an outer diameter of 24 mm, an inner diameter of

20 mm and were placed on a rectangular grid of $32 \times 32 \times 24$ mm$^3$. The sphere shell attenuation was 0.04 mm$^{-1}$ (which is similar to the attenuation of cortical bone at 70 keV). The background cylinder had a diameter of 256 mm, a height of 192 mm and an attenuation coefficient of 0.01 mm$^{-1}$. For the simulation, the phantom was discretized using nearest neighbouring interpolation in an image of $320 \times 320 \times 240$ voxels with a voxel size of $1 \times 1 \times 0.5$ mm$^3$.

The second phantom (Fig. 8.6) was a voxelized head phantom, created from the CT image of an anthropomorphic phantom by interpolating it to a grid of $320 \times 320 \times 240$ voxels with a voxel size of $1 \times 1 \times 0.5$ mm$^3$.

After the simulation of the CT scan(s) the detectors were resampled by summing $2 \times 2$ pixels for both phantoms, as mentioned above, and the images were reconstructed into a grid with voxels of $2 \times 2 \times 1$ mm$^3$ covering the same FOV as used for the simulation.
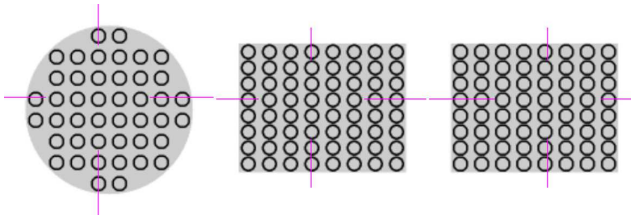


Figure 8.5: Transaxial, coronal and sagittal view of the multi-sphere phantom. The purple lines are crosshairs specifying the location of the other two orthogonal slices.
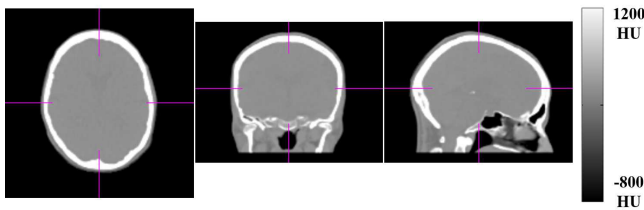


Figure 8.6: Three orthogonal views of the voxelized head phantom.

## 8.2.4  Motion recording

For simulations, we used six degrees-of-freedom head motion data acquired from 3 healthy volunteers using an infrared optical tracking system (Optitrack Flex 13, Natural Point Inc, Corvallis, OR USA). One volunteer was asked to move the head moderately, another two were asked to move their heads as much and as rapidly as possible. The head motion was recorded while the volunteers were lying on the CT-bed, but no CT-scan was acquired. More

details about acquiring the motion data can be found in (Kim et al. 2016), which also provides the recorded motions as supplementary data.

For the phantom scan, the experiment was similar to the one described in (Kim et al. 2015b). A Hoffman brain phantom (diameter 17.5 cm, height 20.8 cm, filled with air) was initially supported by a wedge in an elevated position on the curved surface of the bed. Just before the scan the wedge was removed by pulling a string from outside the room. This caused the phantom to roll from side to side 5 or 6 times on the concave bed with diminishing amplitude for the remainder of the scan. The movement lasted for approximately 10 s. Most of this motion consisted of translations and rotation in the transaxial plane. However, there was also motion out of the transaxial plane: in its original elevated position, the axis of the phantom was not aligned to the axis of the bed, and the phantom aligned itself while rolling on the bed. The CT-scan was performed while the motion was recorded.

All the acquired motion data were converted to isocenter coordinates, smoothed with a 2nd degree polynomial to reduce measurement jitter, and linearly interpolated to obtain the pose at the time of each projection acquisition, as described in (Kim et al. 2015b).

### 8.2.5 Reconstruction with rigid motion correction

In the presence of motion, the helical CT source trajectory is distorted into an effective trajectory with arbitrary shape. As discussed above, an arbitrary effective trajectory with truncation presents challenges for analytical reconstruction algorithms, which we have avoided by using an iterative reconstruction algorithm. In the present work we used the MLEM reconstruction algorithm (Shepp et al. 1982). Actually, this is standard MLEM with an adjusted system matrix. Instead of moving the reconstruction image, rigid motion correction was done by considering a coordinate system fixed to the object and incorporating the motion (now associated to the source-detector pair) into the system matrix (Sun et al. 2016). This corresponds to an arbitrary 3D motion of the virtual gantry around the object being scanned. Because of the high rotation speed and the large number of views, the motion within a single view is negligible.

The ordered subsets technique was adopted to speed up the convergence of the iterative reconstructions (Hudson et al. 1994). The number of iterations and subsets used in all reconstructions are specified in Table 8.1. All projectors/backprojectors were implemented using the distance-driven approach (De Man et al. 2004).

To illustrate that the Tuy map identifies fundamental data-insufficiency that poses problems to any reconstruction algorithm (which relies on the measured data only), all reconstructions were also performed with SART (Andersen et al. 1984).

## 8.2.6 Artifact quantification

In simulations with the multi-sphere phantom, the motion-corrected reconstructed image is likely to suffer from artifacts in cases of data-insufficiency, because the object has spatial frequencies in all possible directions. Thus, for this particular phantom, the occurrence and severity of reconstruction artifacts are expected to correlate well with the degree of data-insufficiency. We performed a reconstruction of the multi-sphere phantom without motion to produce a reference image. When rigid motion was included, the severity of artifacts was quantified using the RMSE between the two reconstructed images, and compared with the Tuy value map from Fig. 8.1:

$$\text{RMSE} = \sqrt{\frac{\sum\limits_{j=1}^{N}(x_j - \tilde{x}_j)^2}{N}} \tag{8.1}$$

where $x_j$ is the value of the $j$th voxel of the evaluated image, $\tilde{x}_j$ is the corresponding value of the reference image and $N$ is the total number of voxels.

The similarity metric RMSE was computed in a block-based fashion. We divided the reconstructed images into small blocks, each being a $16 \times 16 \times 12$ voxels neighborhood surrounding the center of each sphere. A similar sampling approach was applied to the Tuy value map. Therefore the final results were two arrays: one stored a metric value quantifying possible artifacts, and one stored the block-averaged Tuy value. Comparative analysis was then performed to reveal the relationship between the local Tuy value and the severity measure of the possible artifacts, in both artifact-free regions and regions affected by artifacts.

## 8.2.7 An interior-like problem simulation

Last, we examined a case where the Tuy map does not predict data-insufficiency in a particular region. In the 2D interior problem, all projections are truncated transaxially on both sides. For the pixels inside the interior region all projection lines are still available, whereas for the surrounding pixels, some lines are lost due to the truncation. The local Tuy values will be zero inside the interior region and greater than zero in the surrounding region, so the local Tuy's condition implies data-sufficiency for the interior region. However, for interior projection data, it is known that the solution is not unique inside the interior region. The reconstructed image may suffer from a DC-shift and low frequency artifacts in the interior region (Natterer 2001).

To examine the effectiveness of the proposed Tuy map on a 3D version of the interior problem, we studied the following interior-like problem. The interior

region can be created by reducing the fanangle. On the other hand, a specially-designed rigid motion can also induce such an interior region, if the outer parts of the object occasionally move out of the FOV during the helical scan. The motion was designed such that the local Tuy's condition was satisfied within the ROI, but not in the volume surrounding that ROI. The created missing data problem has some similarity to that of the classical 2D interior problem. We then checked how the reconstruction of the interior region was affected by the incomplete sampling in the surrounding structures. The hypothesis was that in this situation, the interior region of the object cannot be exactly reconstructed, although the local Tuy values are very low. Note that here the simulation is not a straightforward extension of the 2D interior problem to 3D, because in our 3D problem, the low Tuy value volume is only surrounded transaxially by high Tuy values, not axially.

## 8.3   Simulations and phantom study

The goal was to verify the effectiveness of the proposed Tuy map in various situations. A total of five studies were performed to verify the predictions of data-insufficiency in the context of helical CT: (1) a static simulation with complete sampling – the object was static during the scan and the FOV was large enough to cover the object in all directions; (2) a simulation with moderate object motion – the object was undergoing moderate motion during the scan while the FOV remained the same as in the first simulation; (3) three simulations, two using the multi-sphere phantom, and one with the voxelized head phantom, with severe object motion, which was likely to create incomplete measurements; (4) a moving phantom scan — an actual helical CT-scan with a moving phantom; (5) Two simulations concerning an interior-like problem. In each study, the reconstructions were compared to the Tuy maps to study the relation between the occurrence of artifacts and the local Tuy values.

### 8.3.1   Simulation with static object

A helical scan of the stationary multi-sphere phantom was simulated as described in Section 8.2.3. The parameters are listed as Configuration 1 in Table 8.1. The FOV covered the whole object in the transaxial plane. The hypothesis was that this experiment would produce a Tuy map which was (almost) zero everywhere and an artifact-free reconstruction, indicating that the sampling was complete everywhere.

### 8.3.2   Simulation with moderate object motion

A segment (Fig. 8.7) of the motion data from a volunteer was applied to the multi-sphere phantom during a helical scan simulation, as described in Section

8.2.3. The scan parameters are listed as Configuration 1 in Table 8.1. As shown in Fig. 8.7, this was a moderate motion with translations up to 8 mm and rotations up to 7°. Since the motion-corrected reconstruction did not produce any artifacts, the Tuy map was expected to be (almost) zero everywhere.

### 8.3.3  Three Simulations with severe object motion

**Two multi-sphere phantom simulations**

Similar simulation experiments were performed with the same multi-sphere phantom, but this time with the more severe volunteer motions shown in Fig. 8.8 and Fig. 8.9. The hypothesis was that for these motions, the Tuy map would have some non-zero values due to data-insufficiency, and the reconstruction with motion correction would produce images with artifacts in those regions. The scan parameters are listed as Configuration 1 in Table 8.1.

**Simulation with the voxelized head phantom**

In order to further investigate the correlation between the Tuy map and the artifacts in an image more similar to those encountered in clinical practice, we applied the motion of Fig. 8.8 also to the voxelized head phantom (Fig. 8.6). Visual assessment was performed to verify the match between the Tuy map and the motion-corrected reconstruction image. Again, we expected that severe artifacts would only occur in regions with high Tuy values.



(a)  (b)
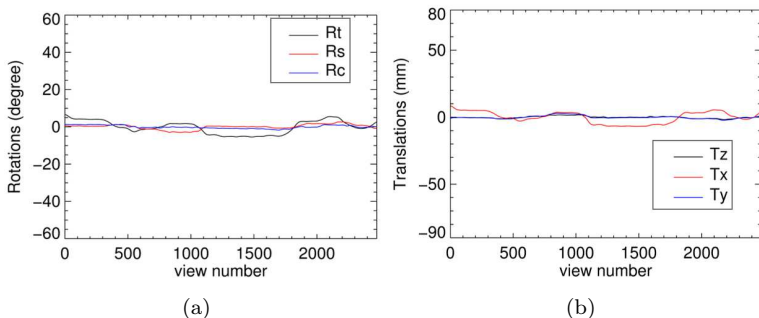
Figure 8.7: A moderate rigid motion segment recorded from subject #1. Left: rotations. Right: translations. All the motion recorded from volunteers can be found in the supplementary data of Kim et al. (2015b).

(a)                                            (b)

Figure 8.8: A severe rigid motion segment from subject #2. Left: rotations.
Right: translations.
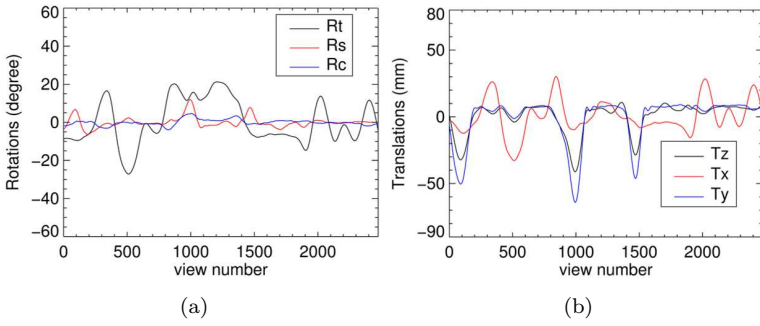


(a)                                            (b)
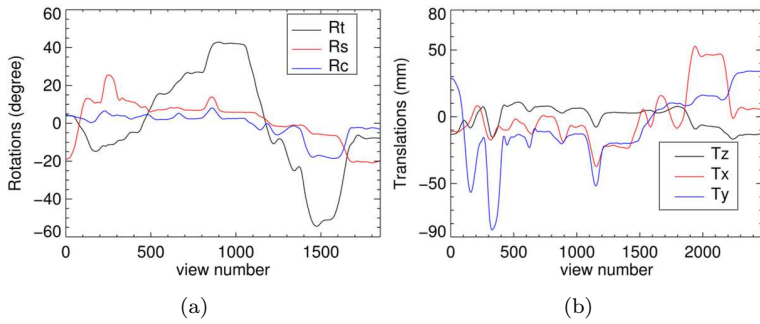
Figure 8.9: A severe rigid motion segment from subject #3. Left: rotations.
Right: translations.
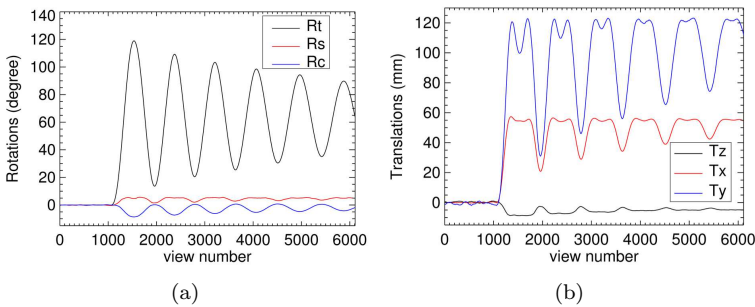


(a)                                            (b)

Figure 8.10: The rolling motion recorded in the phantom scan. Left: rotations.
Right: translations.

### 8.3.4  A moving phantom scan

A 3D Hoffman brain phantom filled with air was used. The scanning parameters are listed as Configuration 2 in Table 8.1. The motion recording setup is described in Section 8.2.4. The rolling motion (Fig. 8.10), had up to 120° in-plane rotation, 120 mm in-plane translation and 10° out-of-plane rotation, 10 mm out-of-plane translation. To assess the data-insufficiency, the Tuy map was computed and compared to motion-corrected images.

### 8.3.5  Two simulations concerning an interior-like problem

The scan parameters used in this simulation are listed as Configuration 3 in Table 8.1. Unlike the previous simulations, a Siemens Sensation 16 CT scanner was simulated. The Sensation 16 has a narrower z-coverage than the Definition AS which we chose for the other simulations. We assumed that the creation of the interior region problem would be easier for a narrow detector, since axial truncation is needed to create the outer region with high Tuy values.

**Data truncation from reduced fan-beam angle**

Simulations were performed with transaxial truncation. For the simulated scanner, the fanangle was reduced from 52.1° to 13.7°. By doing this, an interior-like problem (similar to 2D interior problem) was created as described in Section 8.2.7. We still used the multi-sphere phantom shown in Fig. 8.5.

OSEM was performed for 50 iterations and 20 subsets to guarantee good convergence of the reconstruction. The Tuy map was computed and confirmed the creation of a 3D interior low Tuy value region, surrounded by higher Tuy values. As discussed in Section 8.2.7, our hypothesis was that the reconstructions would suffer from a DC-shift and/or low frequency artifacts inside the interior region, where the sampling was complete according to the Tuy map.

**Data truncation from rigid motion**

As indicated in Section 8.2.7, we designed a rigid motion to create a pattern of truncation in the projections that would be similar to the situation of the 2D interior problem. For each CT projection view, the object was rotated by a constant angle of 7.5° about an axis located inside the transaxial plane and perpendicular to both the rotation axis of the scanner, and to the line connecting the source and the center of the detector array (Fig. 8.11). With such motion, there was always part of the outer object moving out of the FOV during the scan. The motion was large enough to create a pattern of motion-induced data truncation that swept over the exterior region, as the source-detector pair moved in a spiral fashion. The motion was contrived to ensure all
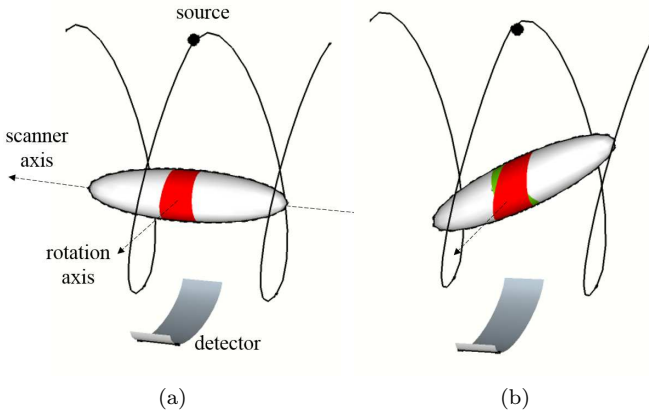
Figure 8.11: The red region indicates the intersection with the FOV for the current view without (a) and with (b) rotation of the object - the green region has been moved out of the FOV (axial truncation) by the rotation.

outer parts of the object would be outside the FOV for some projection views, while the inner parts of the object always stayed within the FOV.

The motion was applied to the multi-sphere phantom (Fig. 8.5) in a simulated helical scan. The simulation and reconstruction setup were identical to the one in last subsection. The Tuy map was computed to confirm the creation of a 3D interior low Tuy value region, surrounded by higher Tuy values.

## 8.4   Results

The results are presented in the same order as in the previous section.

### 8.4.1   Simulation with static object

Three orthogonal planes through the 3D reconstructed images of the static multi-sphere phantom are shown in Fig. 8.12(a). These images, when compared to those of Fig. 8.5, suggest that the reconstruction was artifact-free everywhere, as anticipated. The same three planes through the 3D Tuy map are shown in Fig. 8.12(b), revealing that all the calculated local Tuy values were between 0 and 0.01, which we consider to be effectively zero. The small non-zero values of the Tuy map are due to the discretizations described in Section 8.2.1. In summary, the local Tuy values were close to zero, and the reconstruction image showed no visible artifacts. These two observations are compatible with each other and with the fact that no data-insufficiency was anticipated for this simulation study.

## 8.4.2 Simulation with moderate object motion

Three orthogonal planes through the 3D reconstructed images of multi-sphere phantom undergoing moderate motion are shown in Fig. 8.13(a). Again, these images, when compared to those of Fig. 8.5, suggest that the reconstruction was artifact-free everywhere, as anticipated. The same three planes through the 3D Tuy map are shown in Fig. 8.13(b), revealing that all the calculated local Tuy values were between 0 and 0.02, which we consider to be effectively zero. In summary, the local Tuy values were close to zero, and the reconstruction image showed no visible artifacts. Hence there was no data-insufficiency in this simulation study, as anticipated.



(a)



(b)
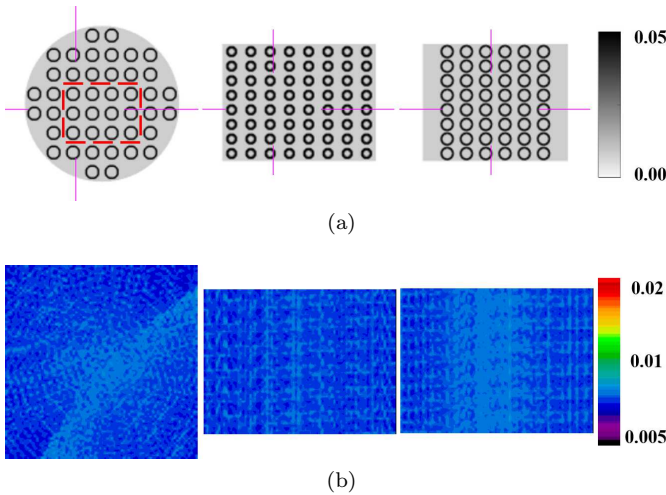
Figure 8.12: Transaxial, coronal and sagittal planes through the MLEM reconstruction from (a) a motion-free CT-scan and (b) the corresponding Tuy map. The red dashed square refers to Fig. 8.15.

## 8.4.3 Three simulations with severe object motion

### Two multi-sphere phantom simulations

Orthogonal planes of the reconstructions with motion correction and the Tuy maps are shown in Fig. 8.14. Reconstruction artifacts were observed for the two sets of severe rigid motions, suggesting that the severe motions did create data-insufficiency. To facilitate comparison of the images an overlay of the Tuy values on the reconstructed image planes is added. The figure shows the planes with the highest Tuy values, and reveals good spatial matching between the occurrence of reconstruction artifacts and increased Tuy values.

As described in Section 8.2.6, we performed a quantitative analysis for the

(a)



(b)
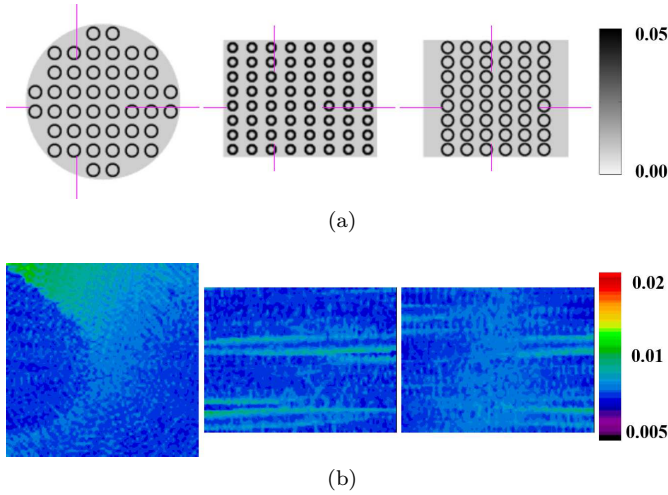
Figure 8.13:  Three orthogonal planes of a motion-corrected MLEM reconstruction from (a) a CT-scan with moderate motion with the motion from Fig. 8.7; (b) the corresponding Tuy map.

results from the motion in Fig. 8.9. Fig. 8.15 reveals a strong positive correlation between the severity of the artifacts and the average Tuy value for selected sampled blocks within the phantom space. From these studies, we observe that the local Tuy value was a good predictor of local artifact severity, at least for the multi-sphere phantom.

### Simulation with the voxelized head phantom

Fig. 8.16 shows the motion-corrected reconstructed images of the digital head phantom which had undergone severe motion (Fig. 8.8) during the scan. We observe that high local Tuy values occur at regions where artifacts appear (red arrows in Fig. 8.16), but there are other regions of high Tuy values that appear artifact-free (blue arrows in Fig. 8.16). Fig. 8.17 shows that although the artifacts in SART are different from those of MLEM, the artifacts occur in the high Tuy value regions for both algorithms. The Tuy map is designed to measure data-insufficiency, but data-insufficiency does not always create artifacts in the reconstruction. The multi-sphere phantom has fine details with edges in all directions, making it very likely that data-insufficiency will indeed create artifacts, which was confirmed by the experiments (Fig. 8.14 and Fig. 8.15). However, typical clinical images often have large fairly uniform regions, which are less challenging for most reconstruction algorithms. In agreement with observations in (Natterer 2001), artifacts showed up "mainly in the vicinity of lines which are tangent to curves of discontinuity of the object and for which the value in the projections are missing". We verified that distortions were mostly seen where the missing projection lines were nearly tangent to some of
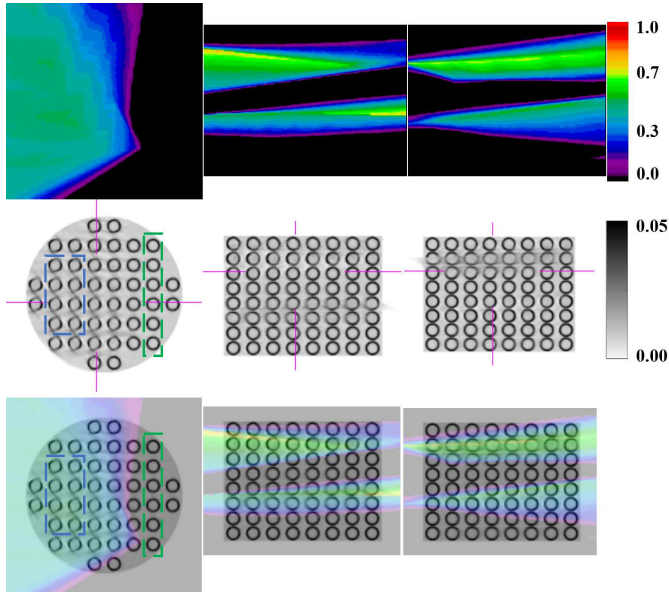
(a)
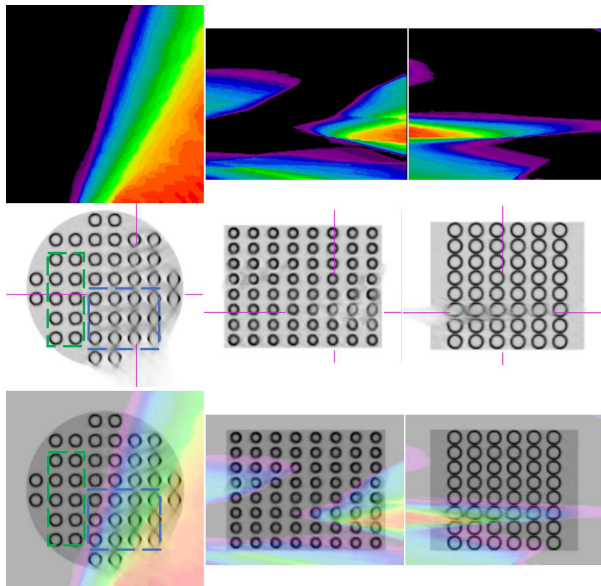


(b)

Figure 8.14: Result of simulations with severe motion of the object, (a) top: Tuy map for the scan with motion from Fig. 8.8; middle: MLEM reconstruction image in the same position; bottom: the image overlayed with the Tuy map. (b) top: Tuy map for the scan with motion from Fig. 8.9; middle: reconstruction image; bottom: image overlayed with the Tuy map. Red indicates high Tuy values and therefore poor tomographic sampling in a particular voxel. The green (artifact-free) and blue (with artifacts) dashed squares refer to Fig. 8.15.
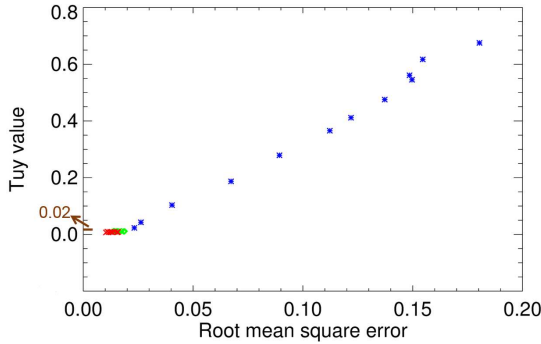
Figure 8.15: The scatter plot shows the relationship between RMSE (reconstructions versus true phantom) and sampled Tuy value in certain regions. Blue points correspond to samples in the blue regions in Fig. 8.14, and green points to those in the green regions. As a reference, red points corresponding to blocks in the red region in Fig. 8.12 (motion-free scan) are included as well.



(a)



(b)
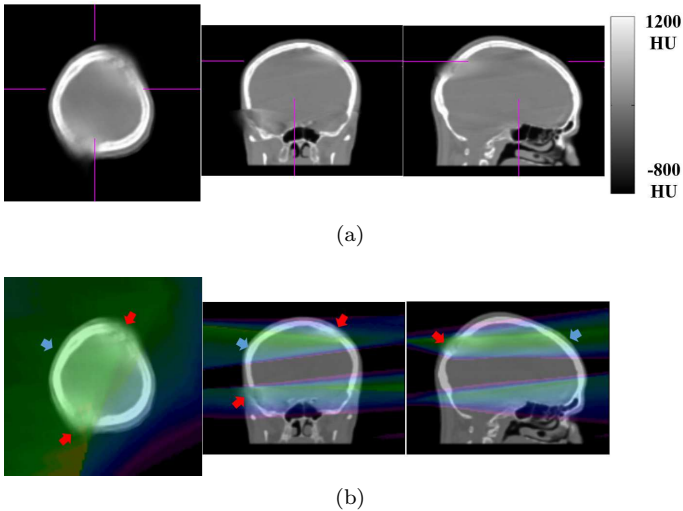
Figure 8.16: Result of the simulation using the head phantom and the motion of Fig. 8.8: (a) the MLEM reconstruction after motion correction; (b) the overlay between the Tuy map (Fig. 8.14a) and the image in (a). Red arrows indicate the distorted regions, blue arrow indicates a region which is artifact-free, although the corresponding Tuy values are relatively high. The Tuy values are all greater than 0.4 at the locations indicated by the arrows. The intensity range of the Tuy map is [0, 0.8].
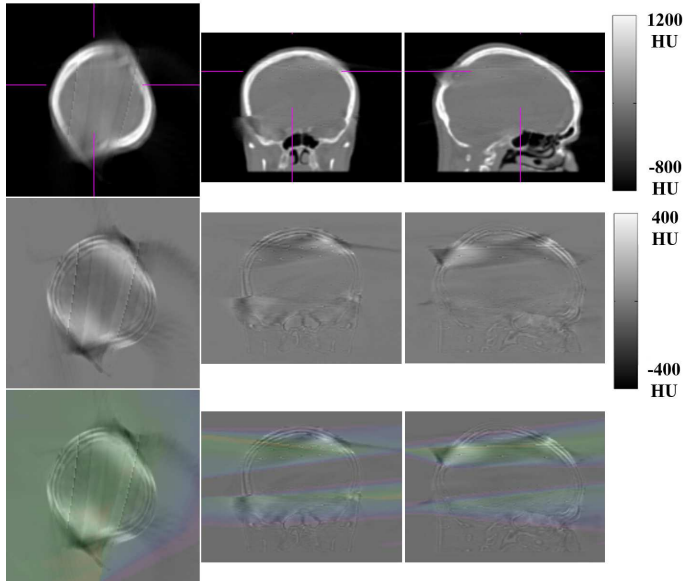
Figure 8.17: Top: The SART reconstruction (same planes as in Fig. 8.16). Middle: the difference between the MLEM (Fig. **??**a and SART reconstructions. Bottom: the difference image with the Tuy map in overlay.

the discontinuities (a separate study was done but not shown in this simulation). The discontinuities that were perpendicular to the missing lines suffered less from artifacts. Consequently, the Tuy map indicates where artifacts may occur, but whether they occur or not depends on the object features.

### 8.4.4 A moving phantom scan

Three orthogonal planes of the motion-corrected images are shown in the middle row of the Fig. 8.18. Different from previous studies, it is based on a real CT-scan of a 3D Hoffman phantom. The artifacts are clearly visible in all three views. The same three views through the 3D Tuy map are shown in the top row of the Fig. 8.18. The regions with high Tuy-values indicate the potential risk of artifacts in those regions. The overlayed image (bottom, Fig. 8.18) indicates that the Tuy map successfully identified the regions where data-insufficiency caused artifacts in the motion-corrected reconstruction images (red arrows). But similar to last subsection, we observed that some regions of high Tuy values appear artifact-free (blue arrows). However, this does not contradict the notion that the Tuy map successfully identified the regions where data-insufficiency might induce artifacts.
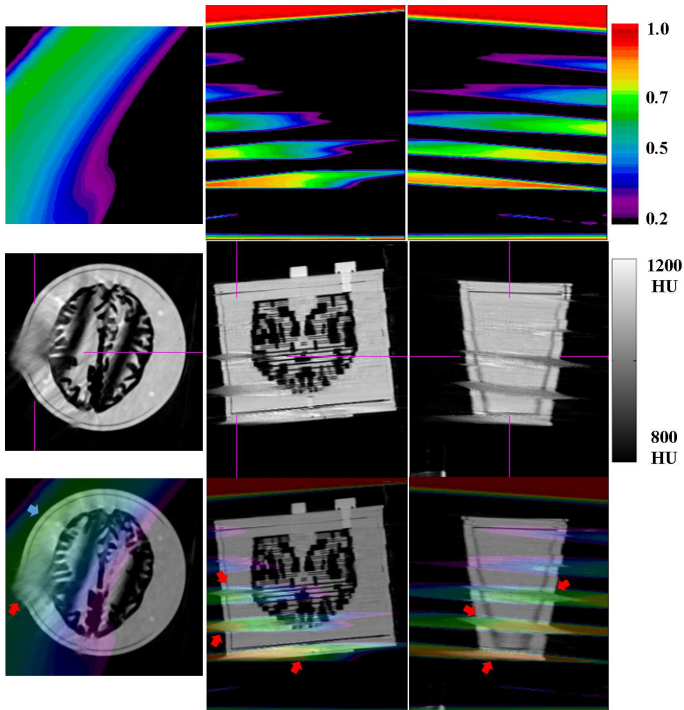
Figure 8.18: Result of the phantom scan. Middle: the MLEM reconstruction image (cropped to display the phantom) after motion correction using the measured motion; Top: the corresponding Tuy map; Bottom: the overlayed image. Red arrows indicate the distorted regions, blue arrow indicates a region which is artifact-free, although the corresponding Tuy values are relatively high. At all regions indicated by arrows, the Tuy values are over 0.5.

### 8.4.5 Two simulations concerning an interior-like problem

**Transaxial data truncation from reduced fan-beam angle**

Fig. 8.19(a) shows the Tuy map for the interior-like problem created by reducing the fanangle. Near the center of the object, the truncation produced a central low Tuy value region transaxially, surrounded by high Tuy values. The high Tuy values indicate incomplete sampling due to the transaxial truncation.

As explained in Section 8.2.7, it was expected that multiple solutions exist inside the interior region, even though the sampling was complete there. A first reconstruction was performed, starting from a uniform image. The reconstruction converged to an under-estimated solution in the interior region (Fig. 8.20(a)-left). To check the uniqueness of this solution, we started another reconstruction from a different image, which was a reference image reconstructed from motion-free projections of the multi-sphere phantom. The reconstruction starting from the reference image converged to a solution (Fig. 8.20(a)-right) very close to that starting reference image. A third reconstruction was initialized with a linear combination of the two solutions. The reconstructed image (not shown here) was different from the previous two solutions and remained essentially unchanged after several iterations, confirming that the problem has multiple solutions. Consequently, the reconstruction problem does not have a unique solution in the interior region of low Tuy values. Therefore, in this interior-like problem one cannot conclude that a local low Tuy value region always indicates that that region can be reconstructed exactly.

**Data truncation from rigid motion**

The simulations in last subsection were repeated in the presence of the designed motion. Fig. 8.19(b) confirms that an interior region was created: the motion-induced sampling incompleteness yielded high Tuy values, surrounding a region where the local Tuy value was low. Very similar results were found for all reconstructions (Fig. 8.20(b)), compared to ones from last subsection.

## 8.5 Discussion

Our results have verified that in the context of rigid motion-corrected helical CT, a region of high Tuy values indicates a likelihood of artifacts there, due to data-insufficiency in agreement with and slightly generalizing the main result of (Finch 1985). With the Tuy map, one can distinguish the artifacts due to data-insufficiency from other types of artifacts, e.g. from beam hardening or motion blurring that could be corrected by using a reconstruction based on a more accurate forward model.

(a)



(b)
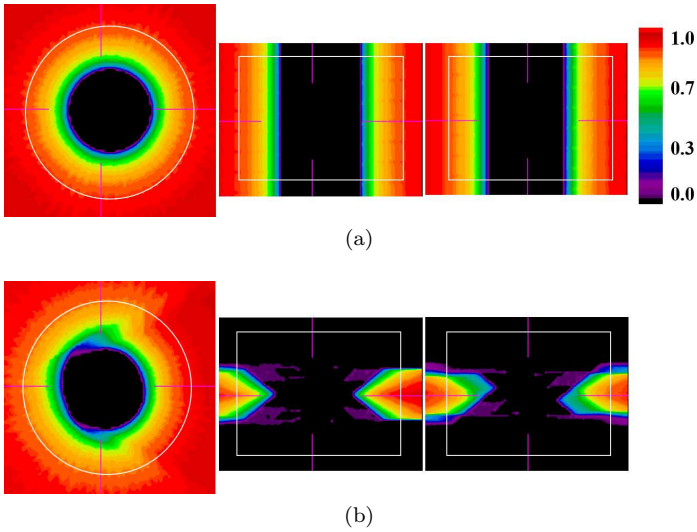
Figure 8.19: From left to right: coronal, sagittal and transaxial views of the Tuy map, with the contour (white) of the object in overlay, (a) for the interior-like problem produced by reducing the fanangle, (b) for the problem created by the view-dependent rigid object motion.

The Tuy map provides a general approach to assess data-insufficiency, potentially useful for many tomographic geometries like helical CT, cone-beam CT with non-standard trajectories or SPECT with non-standard collimators and/or trajectories, regardless of motion. The algorithm described in Section 8.2.1 can easily be modified for a specific geometry. One issue is that finding the complete set of measured projection lines (step 1 in Fig. 8.1) can be time consuming. Depending on the scan features, this step can be further optimized. For common trajectories, e.g. circle and helix, it would be possible to compute the optimal projection line analytically without searching through all available projection lines. For other trajectories, it is still very likely that the optimal projection line will occur in a short and predictable segment of the trajectory, which reduces the search space. For one particular voxel, searching can start from the index of an optimal projection line of a neighbouring voxel that is already computed, which could reduce the computational burden significantly. In this paper we applied this modification to the program in all the simulations where no motion was present.

As shown in Fig. 8.12, 8.13 and 8.15, and contrary to theory, Tuy values were larger than zero in the static simulation. This is due to the discretizations described in Section 8.2.1. Based on the multi-sphere phantom simulation, we consider that if the Tuy value is larger than a threshold (0.02, see Fig. 8.15) in a local region, some data-insufficiency exists and it can create artifacts in that region. The severity of the potential artifacts is roughly proportional to the local Tuy value.
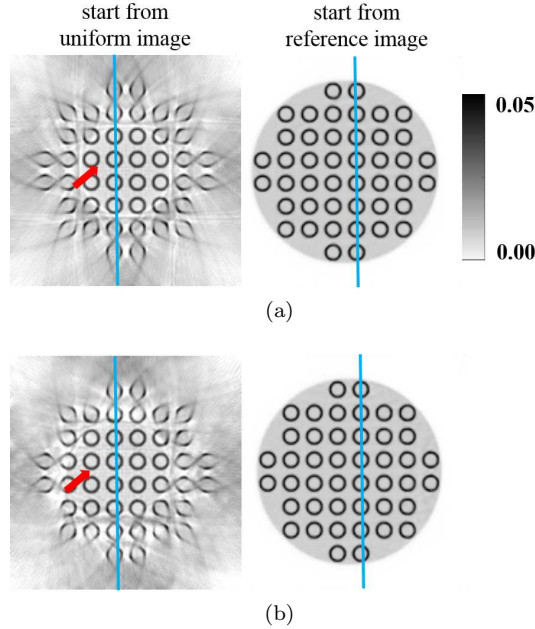
Figure 8.20: Coronal views (central-slice position) of reconstruction images after 1000 updates from (a) reducing the fanangle and (b) synthetic rigid motion. The red arrow indicates the DC-shift in the interior region. The blue lines refer to Fig. 8.21.
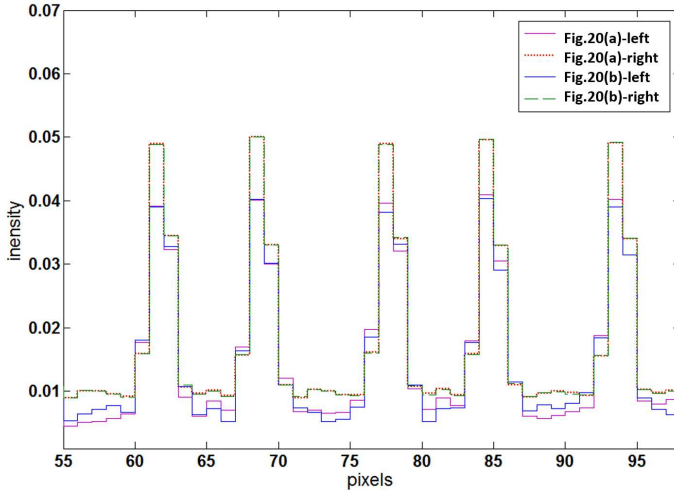


Figure 8.21: Profiles along the blue lines in Fig. 8.20: the maximum difference between Fig. 8.20(a)-left and Fig. 8.20(a)-right is 20.6 % of the maximum intensity; the maximum difference between Fig. 8.20(b)-left and Fig. 8.20(b)-right is 24.9 %.

119

In all the simulations there was a small intentional geometric mismatch between the geometry of the simulated data and the geometries used for calculating the Tuy map and for forward and backward projections in the reconstructions. The purpose of this mismatch was to avoid unrealistically "perfect" data, sometimes called "the inverse crime". Otherwise the simulation was ideal: noise, scatter and beam hardening were not simulated, because we wanted to focus on data-insufficiency, avoiding other confounding sources of artifacts. An expectation maximization reconstruction was chosen as the reconstruction algorithm (MLEM), but the Tuy map is independent of the reconstruction method. For regions where the data are insufficient, any reconstruction algorithm may produce a wrong solution (unless it would make use of additional prior knowledge, but this is not considered in this paper). We also tested all the simulations with another iterative reconstruction algorithm, i.e. SART (Fig. 8.17). All results were similar to those in Section 8.4.

The incompleteness in helical CT was caused by two main effects: the effective trajectory and truncation. The effective trajectory could be incomplete even for an ideal cone-beam tomograph, where all projections would be untruncated. For example, if the object moved in the direction of the scanner axis with the same speed as the bed but in the opposite direction, then the effective trajectory would become circular, which is known to be incomplete except for the central slice. The limited axial coverage of the clinical CT system produces additional data loss, which could create data-insufficiency for an otherwise complete effective trajectory. For example, in the rolling phantom study, careful examination of the motion showed that the complex behaviour of the effective trajectory in the axial direction, combined with axial truncation, generated the data-insufficiency. Fortunately, the Tuy value approach verifies any data-insufficiency, independent of its causes.

A high Tuy value in the Tuy map indicates data-insufficiency, however, the interpretation of a zero Tuy value is less obvious. Specifically, in the situation where the scan produces regions with increased Tuy values, we cannot conclude that exact reconstruction is possible in the region of low Tuy values. In particular, for our example of the interior-like problem, we observed that the reconstruction problem does not have a unique solution inside the interior region, although the image quality inside is typically acceptable. However, if the Tuy value is close to zero *everywhere*, then it is believed that the data are sufficient for exact reconstruction everywhere. This notion is generally accepted although not mathematically proven (Clackdoyle 2005) except in the 2D case.

We have observed that data-insufficiency only appears to produce artifacts if the object being scanned has specific structural features at that point, in particular discontinuities that are parallel to missing projection lines. In contrast, no obvious artifacts were found in high Tuy value regions where the missing projection lines were perpendicular to surfaces of discontinuities. However, this does not contradict the notion that the Tuy map provides a useful warning

whenever artifacts could be present because of incomplete sampling.

The proposed Tuy value computation (Fig. 8.1) is similar to that of Metzler et al. (2003a,b) and Liu et al. (2012), but with some differences in the details. In (Metzler et al. 2003a), voxels were identified as either belonging or not to the fully sampled region, without identifying the degree of insufficiency. In (Metzler et al. 2003b) and (Liu et al. 2012) the degree of insufficiency was quantified as the fraction of projection lines that are missing, whereas in this work, the insufficiency was quantified as the largest angle of missing lines. We have assumed that one set of missing projections covering a large angle is worse than many sets associated with small angles. The validity of this assumption remains to be investigated.

## 8.6 Conclusion

We have introduced a data-insufficiency measure that we call the Tuy map, the purpose of which is to quantify on a scale of zero to one, the degree of data-insufficiency at each point in the reconstructed image. Zero indicates no insufficiency, and one indicates severe insufficiency and is a signal that artifacts are likely to appear in that location. The Tuy map is calculated directly from the geometry of the acquisition: from the effective trajectory (the inverse rigid motion applied to the physical trajectory) and the truncations of the projections. The local Tuy values are independent of the object scanned, and are independent of the choice of the algorithm subsequently used for image reconstruction. Whether or not artifacts appear where high Tuy values occur depends on the object being imaged and not on the reconstruction algorithm (unless the algorithm is using other prior information). Low Tuy values do not guarantee accurate artifact-free reconstructions because a 3D effect similar to the 2D interior problem can occur.

Our studies which corroborated the above findings were all performed in the context of rigid motion-corrected helical CT scanning, but we believe that the principles are general and can be applied to other scan situations and other modalities where, at least to first order, the imaging model involves truncated or untrucated cone-beam projections.

## Acknowledgement

**Part IV**

# General conclusion and Future work

# Chapter 9

# General Conclusion and Future work

## 9.1 Summary and Conclusion

In this thesis, we have investigated several issues related to rigid motion correction in computed tomography (CT) imaging. The thesis was divided into four parts. Specifically, in part I (Chapter 1-4), we introduced the background of the X-ray CT imaging and reviewed several existing motion correction methods in CT imaging. In part II (Chapter 5), we listed several objectives to be achieved in this thesis. In part III (Chapter 6-8), we demonstrated the proposed solutions to address above objectives, which corresponds to three publications.

- Chapter 1 - We briefly reviewed the development of the X-ray CT scanners. CT imaging provides an unprecedented capability in visualizing the human anatomy. Since the invention of the first CT system, four generations of CT system have been developed. Today two most commonly used scanner models are clinical multi-row CT and cone-beam CT, both are based on the third generation design.

- Chapter 2 - We reviewed several physical processes that affect the acquisition of CT data, including X-ray photons generation, X-ray photons interaction with matter and X-ray photons detection. X-ray photons are produced inside a tube and distributed in a certain energy range. Emitted X-ray photons travel towards and interact with the patient body, where multiple interaction processes happen. As a result, the number of pho-

tons detected after propagation through the body is often much smaller than the number of photons emitted from the tube. Nowadays most of the state-of-art clinical CT systems uses energy integrating detectors to measure the photons.

- Chapter 3 - We first reviewed the concepts related to CT reconstruction, including projection, backprojection and data-sufficiency. Then two categories of reconstruction algorithms, analytical reconstruction algorithms and iterative reconstruction algorithms were introduced. Many analytical reconstruction algorithms are based on the Fourier slice theorem, which describes a relationship between the scanned object and measured data. An analytical algorithm obtains the solution by applying analytical inversion of the Radon transform in a one-step calculation. An iterative algorithm obtains the solution which minimizes a measure of data-inconsistency between the measured data and computed projections in a feedback loop (Fig. 3.11). Forward and backward projection operations are repeated within this iterative process. An iterative algorithm is considered to have several advantages over an analytical one, but often requires considerable computation power especially when reconstructing the image from a real scan. Because of that, we reviewed several reconstruction acceleration techniques at the end of this chapter.

- Chapter 4 - We first briefly discussed the frequent occurrence of motion artifacts, then several existing motion correction methods in CT imaging were introduced. We categorized the existing motion correction methods in two groups. Methods in the first group require motion information, and consist of motion acquisition and motion compensation processes. Motion acquisition derives the motion from reference images, surrogate signals or from the data themselves. Motion compensation reduces the artifacts during a reconstruction process, which either using an analytical algorithm or an iterative algorithm. Methods in the second group correct the motion artifacts without the explicit knowledge of the motion, and we call them image-processing based methods.

- Chapter 5 - We listed three objectives to be achieved in this thesis, including: (1) to propose a new approach to mitigate the motion artifacts in helical scans of the head; (2) to extend that artifacts reduction approach to dental cone-beam CT imaging; (3) to identify the degree of incompleteness of the measurement at voxel level in rigid motion-corrected scans.

- Chapter 6 - We proposed a rigid motion correction approach for helical head CT scans. It only requires the knowledge of the measured raw data. We categorized it into joint estimation and compensation methods described in Chapter 4. The proposed approach iteratively updates the motion and the image. In each iteration rigid motion is estimated view-by-view and then used to update the system matrix, which is used in a motion-compensated reconstruction. A multi-resolution scheme is used to accelerate these alternate updates. A fine-resolution reconstruction is

obtained with the last motion estimate. Several techniques are applied to accelerate this final reconstruction, which produces an image with diagnostic quality. Proposed approach was evaluated in various studies, including simulations, patient studies and a phantom study. Qualitatively, as assessed by an experienced radiologist, image quality was improved after compensation in all studies; quantitatively, root-mean-square-error (RMSE) was reduced and mean structural similarity (MSSIM) was increased in both simulations and a phantom study, where the ground truth was available.

- Chapter 7 - We proposed a rigid motion correction approach for dental cone-beam CT scans. It is based the approach described in Chapter 6. A dental CT-scan differs from a helical CT-scan in several aspects, one of the which is the usage of the smaller transaxial field-of-view (FOV) to avoid the unnecessary radiation dose. To account for the differences, we modified the approach in Chapter 6 by introducing a patch-based reconstruction algorithm to the image update. The proposed approach was first evaluated in simulation studies, and it was found both improving the motion estimation accuracy and accelerating the motion correction. Most of the artifacts in the reconstructed images were eliminated after correction. In addition, promising results were obtained in a phantom study. However, in dental cone-beam CT, motion is sometimes not rigid but non-rigid. We expect the approach would fail for a scan where non-rigid motion is present.

- Chapter 8 - We proposed an approach to quantify the data-insufficiency for reconstructing the image from a given scan. Severe rigid motion could induce incomplete sampling in certain regions of a reconstructed image. The reason is that when performing the reconstruction, rigid motion correction effectively moves the locations of source. This creates an effective source trajectory with respect to the patient, which may differ significantly from the intended one. Combined with axial or even transaxial detector truncation, the distorted trajectory can cause incomplete sampling in the measured data. If measured data are insufficient, then accurate and stable reconstruction from the data is not possible. We proposed a measure called Tuy map, which quantifies voxel-level insufficiency. A high value indicates a significant local data-insufficiency, which is a signal that artifacts are likely to happen at that location. The proposed approach was evaluated in several simulations and a phantom study. In all cases, the Tuy map indicated all regions in the reconstructed images which suffered from data-insufficiency and where artifacts were likely to occur. We also demonstrated a case where exact local reconstruction was not assured although no local data-insufficiency was detected. We believe that the proposed approach can be applied to many tomographic geometries, e.g. helical CT, cone-beam CT with non-standard geometries or SPECT with non-standard collimators and/or trajectories, regardless of motion.

## 9.2 Future work

### Further evaluation of proposed rigid motion correction method on clinical CT scans

In Chapter 6, we evaluated the proposed motion correction approach on four helical head CT scans. By the time this thesis was finished, we had tested 56 more scans and all images had been reviewed by two radiologists. These include 25 acquired on a Siemens Force scanner in the Westmead Hospital in Sydney, 21 on a Siemens Sensation 64 scanner and 8 on a Siemens Force scanner in the Sydney Children's Hospital. The aim of this evaluation is to prove that the approach is robust with different scan setups and with patients having various ages and diseases. Additionally, we are interested in answering the following questions: (1) will a radiologist prefer the corrected image over non-corrected ones, for both bone and soft-tissue images? (2) while the approach works well on motion-contaminated scans, how is the effect on the motion-free ones? (3) what are the potential applications (among trauma, bleeding and fracture detections, etc.) that benefits the most from motion correction? Since we are still analysing the results, no answers regarding above questions are reported in this thesis.

### Acceleration of proposed rigid motion correction method

As reported in Chapter 6, the average time to perform motion correction on a normal head scan is about 14 hours. Of this time, 2 hours are for the motion estimation, 12 hours are for the final reconstruction (on a GPU). Clearly the bottleneck is the final iterative reconstruction. We have tested the running time of final reconstruction on different hardware platforms with parallel computing (using OpenCL):

Table 9.1: Running time of the final reconstruction on different hardwares.

| Hardware structure | NIVIDIA C2075 | NIVIDIA K40 | NIVIDIA V100 | Intel Xeon E5-2699 v4 |
|---|---|---|---|---|
| Running time (hours) | 12 | 6 | 1 | 5.5 |

Aside from using advanced hardware, further acceleration of the final reconstruction can be achieved in three ways:

(1) Improve the convergence rate of the reconstruction algorithm itself, by applying advanced optimization techniques.

(2) Optimize the implementation of the algorithm on specific hardware structure, such as implementing the whole iterative algorithm on a GPU.

(3) Replace the iterative reconstruction with an Iterative FBP reconstruction (Fig. 3.11b). This demands the correct handling of the ramp-filtering and weightings in the analytical reconstruction when performing the rigid motion compensation. Above handling is less demanding when the motion to be compensated is small. In such cases the approximate analytical reconstruction probably would still provide acceptable reconstructed image quality. The artifacts are expected to be suppressed with only one or few iterations of FBP. However, when motion to be compensated is large, induced artifacts often cannot be eliminated in an iterative scheme. In such case, the motion must be accounted for the ramp-filtering and/or the backprojection weightings. Implementing such an approach would hopefully allow the usage of Iterative FBP for compensating severe motion.

Not only for final reconstruction, acceleration of the motion estimation is also possible by introducing an adaptive estimation strategy. This is based on the fact that the motion amplitude may vary across time, i.e. pose change might be large in certain views but little in other views. One can invent an estimation scheme that does more computation on motion-affected views, but less on other views. This requires an initial identification of the views possibly affected by motion before the actual estimation. For example, similarity metrics (e.g. MSSIM) can be measured for all adjacent views, which will probably produce a profile that can be used to identify views that are likely to be affected by motion. When performing the estimation, early iterations will only focus on the possible motion-affected views, while later iterations perform the estimation in all views just like in Chapter 6.

## Motion correction for non-rigid motion

While the proposed approach is designed for rigid motion correction, it would be interesting to investigate how to extend it to non-rigid motion correction. Like for rigid motion, we assume the deformation fields may be different across views in a CT-scan affected by non-rigid motion because of the high sampling rate. Hence for non-rigid motion, we have much more parameters to be estimated in each view, compared with the previous six rigid parameters. Like for rigid motion, we can calculate the derivative of the projection intensity with respect to each non-rigid parameter. From those derivatives we are able to obtain a first estimate of the motion fields across views. Then we can perform the motion compensation with this initial motion estimate, and repeat the motion estimation and compensation for several iterations until convergence. During this process, both spatial and temporal constraints can be introduced to motion fields, as non-rigid motion in human body are often smooth in nature.

However, the difficulty of the non-rigid motion estimation is that not all parameters are equally sensitive to the projection intensity changes. One can imagine that high-intensity structures (e.g. ribs) contribute to the measurement much more than low-intensity ones (lung tumors) do. As a result, our

projection-based approach would accurately estimate the local motion of the high intensity structures, but not that of low-contrast regions. For example in a motion-contaminated thoracic CT-scan, the proposed approach would probably fail to estimate the movement of the lung tumor. One solution is to identify the high intensity structures surrounding the lung tumor as virtual markers (Rene 2010), but this might be difficult in real implementation. Another solution is to perform the motion estimation with the help of a 4D prior motion model (Zhang et al. 2017). Such a model provides an initial estimate of the motion fields in all projection views, which could help the motion estimation process significantly.

## Extending the rigid motion correction method to online cone-beam CT calibration

For cone-beam CT, there is a connection between the rigid motion correction and online calibration - the rigid movement of an object is equivalent to (virtual) inverse movement of the source-detector pair. Based on this, the proposed motion correction approach can be extended to perform simultaneous calibration and reconstruction for a cone-beam CT-scan. Since often the unintended movement of the cone-beam CT source/detector is small (often jittering), parameter estimation should not take too many iterations. One potential problem is the estimation of the relative movement between the source and the detector. This requires the estimation of three additional parameters on top of the original six in each projection view. It is unclear if introducing these three parameters would adversely affect the identifiability of the other motion parameters. On the other hand, it is often safe to ignore estimating some of the nine parameters, as they were found to have little effect on image quality (Kingston et al. 2011; Muders et al. 2014).

## Further evaluation of proposed rigid motion correction method on dental imaging

In Chapter 7, we applied the motion correction to the simulated scans and a phantom scan that were affected by small rigid motion. Although good initial results were observed, several concerns exist before further applying the proposed approach on real dental scans:

(1) The proposed approach would probably fail to eliminate the artifacts caused by non-rigid motion. This is unfortunate, as many dental CT scans are affected by such kind of motion (tongue movement, swallowing, etc., (Spin-Neto et al. 2016)).

(2) Size of the scan FOV might affect the motion estimation accuracy. It is expected that the smaller the FOV is, the less accurate the image estimate will be, as in theory complete FOV reconstruction should be available to compute

new projections. Induced errors could propagate into motion compensation, although little effects were observed in our preliminary studies where the motion was small.

(3) For cone-beam CT, the proposed approach assumes that the object position in each projection view cannot deviate much from the average position of the object in an initial reconstruction. The reason is that the 2D/3D registration (in motion estimation) tries to align each measured projection to the initial volume in the first iteration. If during such alignment, a motion-free projection is registered to a severely distorted volume, false-positive movement might be estimated for that projection. Based on our (limited) experience, it is therefore beneficial to limit the motion estimation to those views which are most likely to be affected by motion (like the phantom study in Section 7.4) to prevent the assignment of this unwanted non-zero motion estimate to motion-free views. This is less problematic for a helical CT-scan, where an axial-truncated projection only correlates to a part of the object, hence the motion estimation mostly relies on the local object and is less sensitive to the whole distorted object.

## Tuy map assisted reconstruction

When a reconstructed CT image suffers from artifacts due to data-insufficiency (caused by truncation and/or motion), a second reconstruction may be needed to obtain an artifact-free image:

(1) When a non-truncated prior scan is available, one can perform a prior-constrained reconstruction for the current truncated scan. The Tuy map from the truncated scan could help this second reconstruction by providing the information about which parts of measurement are required but missing. An example is an application on scans from a dual-source scanner (e.g. Siemens Force), of which the high-energy scan is with full FOV but the low-energy scan is with limited FOV. To reconstruct a full FOV low-energy scan, one can use the high-energy CT image as prior information via techniques like PICCS (Chen et al. 2008) or DPIRPLE (Dang et al. 2014; Pourmorteza et al. 2016). The Tuy map from the low-energy scan could provide information about the degree to which each voxel suffers from data-insufficiency. One can incorporate such information into the reconstruction by implementing a position-dependent prior weight - high weights are chosen for those voxels with high data-insufficiency.

(2) When no prior scan is available, a repeat scan may be needed. For instance, assume we have a helical scan with artifacts due to data-insufficiency caused by severe rigid motion. Again the Tuy map can provide information about which voxels do not have enough data for reconstruction. Hence the repeat scan can be limited to a limited axial range, and the final image can be reconstructed from both two scans. This could shorten the overall scan time and avoid the unnecessary dose to the patients in the repeat scan.

# Bibliography

Ackerman, M. J. (1998). "The visible human project." In: *Proc. IEEE* 86.3, pp. 504–511.

Ahn, S. and J. A. Fessler (2003). "Globally convergent image reconstruction for emission tomography using relaxed ordered subsets algorithms." In: *IEEE Trans. Med. Imaging* 22.5, pp. 613–626. DOI: `10.1109/TMI.2003.812251`.

Ahn, S., J. A. Fessler, D. Blatt, and A. O. Hero (2006). "Convergent incremental optimization transfer algorithms: Application to tomography." In: *IEEE Trans. Med. Imaging* 25.3, pp. 283–296. DOI: `10.1109/TMI.2005.862740`.

Aichert, A., M. Berger, J. Wang, N. Maass, A. Doerfler, J. Hornegger, and A. Maier (2015). "Epipolar Consistency in Transmission Imaging." In: *IEEE Trans. Med. Imaging* 34.11, pp. 2205–2219. DOI: `10.1109/TMI.2015.2426 417`.

Andersen, A. and A. Kak (1984). "Simultaneous Algebraic Reconstruction Technique (SART): A superior implementation of the ART algorithm." In: *Ultrason. Imaging* 6.1, pp. 81–94. DOI: `10.1016/0161-7346(84)90008-7`.

Barrett, J. F. and N. Keat (2004). "Artifacts in CT: recognition and avoidance." In: *Radiographics* 24.6, pp. 1679–91. DOI: `10.1148/rg.246045065`.

Bauschke, H. H. and J. M. Borwein (1996). "On projection algorithms for solving convex feasibility problems." In: *SIAM Rev.* 38.3, pp. 367–426.

Beck, A. and M. Teboulle (2009). "A Fast Iterative Shrinkage-Thresholding Algorithm for Linear Inverse Problems." In: *SIAM J. Imaging Sci.* 2.1, pp. 183–202. DOI: `10.1137/080716542`.

Beekman, F. J., C. Kamphuis, and E. C. Frey (2001). "Ordered subset reconstruction for x-ray CT Ordered subset reconstruction for x-ray CT." In: *Phys. Med. Biol.* 46.7, pp. 1835–44.

Benson, T. M., B. K. De Man, L. Fu, and J. B. Thibault (2010). "Block-based iterative coordinate descent." In: *IEEE Nucl. Sci. Symp. Conf. Rec.* pp. 2856–2859. DOI: `10.1109/NSSMIC.2010.5874316`.

Berger, M. et al. (2017). "Motion compensation for cone-beam CT using Fourier consistency conditions." In: *Phys. Med. Biol.* 62.17. DOI: `10.1088/1361-6 560/aa8129`.

Bhowmik, U. K. and R. R. Adhami (2012). "A head motion measurement system suitable for 3D cone-beam tomography using markers." In: *IEEE*

*Eng. Med. Biol. Soc. Conf. Proc.* pp. 5975–5978. DOI: `10.1109/EMBC.2012`
`.6347355`.

Bier, B., M. Unberath, T. Geimer, J. Maier, G. Gold, M. Levenston, R. Fahrig, and A. Maier (2017). "Motion Compensation Using Range Imaging in C-Arm Cone-Beam CT BT." In: *Med. Image Underst. Anal. 21st Annu. Conf. MIUA 2017.* Cham: Springer International Publishing, pp. 561–570. DOI: `1`
`0.1007/978-3-319-60964-5_49`.

Borman, S. (2009). "The Expectation Maximization Algorithm A short tutorial." In: *Submitt. Publ.* pp. 1–9. DOI: `10.1097/RLU.0b013e3181b06c41\r`
`00003072-200909000-00002`.

Byrne, C. (2005). "Choosing parameters in block-iterative or ordered-subset reconstruction algorithms." In: *IEEE Trans Med Imaging* 14.3, pp. 321–327. DOI: `10.1109/NSSMIC.2004.1462771`.

Caroline, A. and P.-E. Danielsson (1994). "Three-dimensional reconstruction from cone-beam data in O(N3logN) time." In: *Phys Med Biol* 39.3, pp. 477–491.

Chen, G.-h., J. Tang, and S. Leng (2008). "Prior image constrained compressed sensing (PICCS): A method to accurately reconstruct dynamic CT images from highly undersampled projection data sets." In: *Med. Phys.* 35.2, pp. 660–663. DOI: `10.1118/1.2836423`.

Choi, J.-H., R. Fahrig, A. Keil, T. F. Besier, S. Pal, E. J. McWalter, G. S. Beaupré, and A. Maier (2013). "Fiducial marker-based correction for involuntary motion in weight-bearing C-arm CT scanning of knees. Part I. Numerical model-based optimization." In: *Med. Phys.* 40.9, p. 091905. DOI: `10.1118/1.4817476`.

Choi, J.-H., A. Maier, A. Keil, S. Pal, E. J. McWalter, G. S. Beaupré, G. E. Gold, and R. Fahrig (2014). "Fiducial marker-based correction for involuntary motion in weight-bearing C-arm CT scanning of knees. II. Experiment." In: *Med. Phys.* 41.6, p. 061902. DOI: `10.1118/1.4873675`.

Chong, E. K. P. and S. H. Zak (2011). *An Introduction to Optimization.* Wiley Series in Discrete Mathematics and Optimization. Wiley.

Chun, S. Y., Y. K. Dewaraja, and J. A. Fessler (2014). "Alternating direction method of multiplier for tomography with nonlocal regularizers." In: *IEEE Trans. Med. Imaging* 33.10, pp. 1960–1968. DOI: `10.1109/TMI.2014.2328`
`660`.

Clackdoyle, R. and F. Noo (2001). "Cone-beam tomography from 12 pinhole vertices." In: *IEEE Nucl. Sci. Symp. Conf. Rec.* 4, pp. 1874–1876. DOI: `10.1109/NSSMIC.2001.1009189`.

Clackdoyle, R. (2005). "Fully 3d reconstruction theory in perspective." In: *Proceeding 8th Int. Meet. Fully 3D Reconstr. Radiol. Nucl. Med.* pp. 64–69.

Clackdoyle, R. and M. Defrise (2010). "Tomographic reconstruction in the 21st Century: region-of-interest reconstruction from incomplete data." In: *IEEE Signal Proc. Mag.* 27.4, pp. 60–80.

Clackdoyle, R. and L. Desbat (2013). "Full data consistency conditions for cone-beam projections with sources on a plane." In: *Phys. Med. Biol.* 58.23, p. 8437. DOI: `10.1088/0031-9155/58/23/8437`.

Clackdoyle, R. and L. Desbat (2015). "Data consistency conditions for truncated fanbeam and parallel projections." In: *Med. Phys.* 42.2, pp. 831–45. DOI: 10.1118/1.4905161.

Clackdoyle, R., L. Desbat, J. Lesaint, and S. Rit (2016). "Data Consistency Conditions for Cone-Beam Projections on a Circular Trajectory." In: *IEEE Signal Process. Lett.* 23.12, pp. 1746–1750. DOI: 10.1109/LSP.2016.2616026.

Courdurier, M., F. Noo, M. Defrise, and H. Kudo (2008). "Solving the interior problem of computed tomography using a prior knowledge." In: *Inverse Probl.* 24.6, p. 065001.

Dang, H., A. S. Wang, M. S. Sussman, J. H. Siewerdsen, and J. W. Stayman (2014). "DPIRPLE: A joint estimation framework for deformable registration and penalized-likelihood CT image reconstruction using prior images." In: *Phys. Med. Biol.* 59.17, pp. 4799–4826. DOI: 10.1088/0031-9155/59/17/4799.

Danielsson, P., P. Edholm, J. Eriksson, and M. M. Seger. (1997). "Towards exact reconstruction for helical cone-beam scanning of long objects. A new detector arrangement and a new completeness condition." In: *Proc. 1997 Meet. Fully3D Image Reconstr. Radiol. Nucl. Med.* pp. 141–144.

De Man, B., J. Nuyts, P. Dupont, G. Marchal, and P. Suetens (2001). "An iterative maximum-likelihood polychromatic algorithm for CT." In: *IEEE Trans. Med. Imaging* 20.10, pp. 999–1008. DOI: 10.1109/42.959297.

De Man, B. and S. Basu (2004). "Distance-driven projection and backprojection in three dimensions." In: *Phys. Med. Biol.* 49.11, pp. 2463–2475. DOI: 10.1088/0031-9155/49/11/024.

De Pierro, A. R. and M. E. B. Yamagishi (2001). "Fast EM-like methods for maximum a posteriori estimates in emission tomography." In: *IEEE Trans. Med. Imaging* 20.4, pp. 280–288. DOI: 10.1109/42.921477.

Defrise, M. and R. Clack (1994). "A Cone-Beam Reconstruction Algorithm Using Shift-Variant Filtering and Cone-Beam Backprojection." In: *IEEE Trans. Med. Imaging* 13.1, pp. 186–195. DOI: 10.1109/42.276157.

Defrise, M., F. Noo, R. Clackdoyle, and H. Kudo (2006). "Truncated Hilbert transform and image reconstruction from limited tomographic data." In: *Inverse Probl.* 22.3, pp. 1037–1053. DOI: 10.1088/0266-5611/22/3/019.

Desbat, L., S. Roux, and P. Grangeat (2007). "Compensation of some time dependent deformations in tomography." In: *IEEE Trans. Med. Imaging* 26.2, pp. 261–269. DOI: 10.1109/TMI.2006.889743.

Desjardins, B. and E. A. Kazerooni (2004). "ECG-Gated Cardiac CT." In: *Am. J. Roentgenol.* 182.4, pp. 993–1010. DOI: 10.2214/ajr.182.4.1820993.

Donaldson, K., S. O'Connor, and N. Heath (2013). "Dental cone beam CT image quality possibly reduced by patient movement." In: *Dentomaxillofacial Radiol.* 42.2, pp. 3–4. DOI: 10.1259/dmfr/91866873.

Elbakri, I. A. and J. A. Fessler (2003). "Efficient and Accurate Likelihood for Iterative Image Reconstruction in X-ray Computed Tomography." In: *Proc. SPIE 5032, Med. Imaging 2003 Image Process.* 5032, pp. 1839–1850.

Elbakri, I. A. and J. A. Fessier (2002). "Statistical Image Reconstruction for Polyenergetic X-Ray Computed Tomography." In: *IEEE Trans Med Imaging* 21.2, pp. 89–99. DOI: 10.1109/ISBI.2002.1029387.

Ens, S., J. Müller, B. Kratz, and T. M. Buzug (2009). "Sinogram-Based Motion Detection in Transmission Computed Tomography." In: *4th Eur. Conf. Int. Fed. Med. Biol. Eng.* Berlin, Heidelberg: Springer Berlin Heidelberg, pp. 505–508. DOI: 10.1007/978-3-540-89208-3_120.

Erdogan, H. and J. A. Fessler (1999a). "Ordered subsets algorithms for transmission tomography." In: *Phys. Med. Biol.* 44.11, pp. 2835–2851.

Erdogan, H. and J. Fessler (1999b). "Monotonic Algorithms for Transmission Tomography." In: *Phys. Med. Biol.* 18.9, pp. 801–814.

Escalante, R. and M. Raydan (2011). *Alternating Projection Methods*. Philadelphia, PA, USA: Society for Industrial and Applied Mathematics.

Fang, R., T. Chen, and P. C. Sanelli (2013). "Towards robust deconvolution of low-dose perfusion CT: Sparse perfusion deconvolution using online dictionary learning." In: *Med. Image Anal.* 17.4, pp. 417–428. DOI: 10.1016/j.media.2013.02.005.

Feldkamp, L. A., L. C. Davis, and J. W. Kress (1984). "Practical cone-beam algorithm." In: *J. Opt. Soc. Am. A* 1.6, pp. 612–619. DOI: 10.1364/JOSAA.1.000612.

Fessler, J. A. (1994). "Penalized Weighted Least-Squares Image-Reconstruction for Positron Emission Tomography." In: *IEEE Trans. Med. Imaging* 13.2, pp. 290–300. DOI: 10.1109/42.293921.

Fessler, J., E. Ficaro, N. Clinthorne, and K. Lange (1997). "Grouped-coordinate ascent algorithms for penalized-likelihood transmission image reconstruction." In: *IEEE Trans. Med. Imaging* 16.2, pp. 166–175. DOI: 10.1109/42.563662.

Fessler, J. A. and D. Kim (2011). "Axial block coordinate descent (ABCD) algorithm for X-ray CT image reconstruction." In: *Proc. 2011 Meet. Fully3D Image Reconstr. Radiol. Nucl. Med.* pp. 262–265.

Finch, D. V. (1985). "Cone Beam Reconstruction with Sources on a Curve." In: *SIAM J. Appl. Math.* 45.4, pp. 665–673. DOI: 10.1137/0145039.

Fu, L., T. C. Lee, S. M. Kim, A. M. Alessio, P. E. Kinahan, Z. Chang, K. Sauer, M. K. Kalra, and B. De Man (2017). "Comparison between Pre-Log and Post-Log Statistical Models in Ultra-Low-Dose CT Reconstruction." In: *IEEE Trans. Med. Imaging* 36.3, pp. 707–720. DOI: 10.1109/TMI.2016.2627004.

Gendrin, C. et al. (2012). "Monitoring tumor motion by real time 2D/3D registration during radiotherapy." In: *Radiother. Oncol.* 102.2, pp. 274–280. DOI: 10.1016/j.radonc.2011.07.031.

Gilbert, P. (1972). "Iterative methods for the three-dimensional reconstruction of an object from projections." In: *J. Theor. Biol.* 36.1, pp. 105–117. DOI: 10.1016/0022-5193(72)90180-4.

Gordon, R., R. Bender, and G. T. Herman (1970). "Algebraic Reconstruction Techniques (ART) for three-dimensional electron microscopy and X-ray photography." In: *J. Theor. Biol.* 29.3, pp. 471–481. DOI: 10.1016/0022-5193(70)90109-8.

Grangeat, P. (1991). "Mathematical framework of cone beam 3D reconstruction via the first derivative of the radon transform." In: *Math. Methods Tomogr.* Berlin, Heidelberg: Springer Berlin Heidelberg, pp. 66–97. DOI: `10.1007/BFb0084509`.

Grass, M., T. Kohler, and R. Proksa (2000). "3D cone-beam CT reconstructions for circular trajectories." In: *Phys. Med. Biol.* 45.2, pp. 329–347.

Gullberg, G. T., B. M. W. Tsui, C. R. Crawford, and E. R. Edgerton (1987). "Estimation of geometrical parameters for fan beam tomography." In: *Phys. Med. Biol.* 32.12, pp. 1581–1594.

Hahn, J., H. Bruder, C. Rohkohl, T. Allmendinger, K. Stierstorfer, T. Flohr, and M. Kachelrieß (2017). "Motion Compensation in the Region of the Coronary Arteries based on Partial Angle Reconstructions from Short Scan CT Data." In: *Med. Phys.* 44.11, pp. 5795–5813. DOI: `10.1002/mp.12514`.

Hanzelka, T., J. Dusek, F. Ocasek, J. Kucera, J. Sedy, J. Benes, G. Pavlikova, and R. Foltan (2013). "Movement of the patient and the cone beam computed tomography scanner: Objectives and possible solutions." In: *Oral Surg. Oral Med. Oral Pathol. Oral Radiol.* 116.6, pp. 769–773. DOI: `10.1016/j.oooo.2013.08.010`.

Herman, G. T., A. V. Lakshminarayanan, and A. Naparstek (1976). "Convolution reconstruction techniques for divergent beams." In: *Comput. Biol. Med.* 6.4, pp. 259–262. DOI: `10.1016/0010-4825(76)90065-2`.

Hudson, H. M. and R. S. Larkin (1994). "Ordered subsets of projection data." In: *IEEE Trans. Med. Imaging* 13.4, pp. 601–609.

Hugo, G. D. and M. Rosu (2012). "Advances in 4D radiation therapy for managing respiration: Part I - 4D imaging." In: *Z. Med. Phys.* 22.4, pp. 258–271. DOI: `10.1016/j.zemedi.2012.06.009`.

Jan, S. et al. (2011). "GATE V6: a major enhancement of the GATE simulation platform enabling modelling of CT and radiotherapy." In: *Phys. Med. Biol.* 56.4, pp. 881–901. DOI: `10.1088/0031-9155/56/4/001`.

Johnson, R. and T. Zhang (2013). "Accelerating stochastic gradient descent using predictive variance reduction." In: *Adv. Neural Inf. Process. Syst.* 1, pp. 315–323.

Jørgensen, J. S. and E. Y. Sidky (2015). "How little data is enough? Phase-diagram analysis of sparsity-regularized X-ray computed tomography." In: *Philos. Trans. R. Soc. London. Ser. A. Math. Phys. Eng. Sci.* 373, p. 20140387. DOI: `10.1098/rsta.2014.0387`.

Jørgensen, J. S., E. Y. Sidky, and X. Pan (2013). "Quantifying admissible undersampling for sparsity-exploiting iterative image reconstruction in X-Ray CT." In: *IEEE Trans. Med. Imaging* 32.2, pp. 460–473. DOI: `10.1109/TMI.2012.2230185`.

Kappler, S., A. Henning, B. Kreisler, F. Schoeck, K. Stierstorfer, and T. Flohr (2014). "Photon counting CT at elevated X-ray tube currents: contrast stability, image noise and multi-energy performance." In: *SPIE Med. Imaging.* Vol. 9033, p. 90331C.

Katsevich, A. (2002). "Theoretically Exact Filtered Backprojection-Type Inversion Algorithm for Spiral CT." In: *SIAM J. Appl. Math.* 62.6, pp. 2012–2026. DOI: `10.1137/S0036139901387186`.

Keall, P. J., A. D. Todor, S. S. Vedam, C. L. Bartee, J. V. Siebers, V. R. Kini, and R. Mohan (2004). "On the use of EPID-based implanted marker tracking for 4D radiotherapy." In: *Med. Phys.* 31.12, pp. 3492–3499. DOI: `10.1118/1.1812608`.

Keck, B. (2014). "High Performance Iterative X-Ray CT with Application in 3-D Mammography and Interventional C-arm Imaging Systems." Doctoral dissertation.

Kim, D., S. Ramani, S. Member, and J. A. Fessler (2015a). "Combining Ordered Subsets and Momentum for Accelerated X-Ray CT Image Reconstruction." In: *IEEE Trans. Med. Imaging* 34.1, pp. 167–178.

Kim, J., J. Nuyts, Z. Kuncic, and R. Fulton (2013). "The feasibility of head motion tracking in helical CT: a step toward motion correction." In: *Med. Phys.* 40.4, p. 41903. DOI: `10.1118/1.4794481`.

Kim, J., J. Nuyts, A. Kyme, Z. Kuncic, and R. Fulton (2015b). "A rigid motion correction method for helical computed tomography (CT)." In: *Phys. Med. Biol.* 60.5, pp. 2047–73. DOI: `10.1088/0031-9155/60/5/2047`.

Kim, J., T. Sun, A. R. Alcheikh, Z. Kuncic, J. Nuyts, and R. Fulton (2016). "Correction for human head motion in helical x-ray CT." In: *Phys. Med. Biol.* 61.4, pp. 1416–1438.

Kingston, A., A. Sakellariou, T. Varslot, G. Myers, and A. Sheppard (2011). "Reliable automatic alignment of tomographic projection data by passive auto-focus." In: *Med. Phys.* 38.9, pp. 4934–4945. DOI: `10.1118/1.3609096`.

Kole, J. S. (2005). "Statistical image reconstruction for transmission tomography using relaxed ordered subset algorithms." In: *Phys. Med. Biol.* 50.7, pp. 1533–1545. DOI: `10.1088/0031-9155/50/7/015`.

Kudo, H., M. Courdurier, F. Noo, and M. Defrise (2008). "Tiny a prioriknowledge solves the interior problem in computed tomography." In: *Phys. Med. Biol.* 53.9, pp. 2207–2231. DOI: `10.1088/0031-9155/53/9/001`.

Kudo, H., T. Rodet, F. Noo, and M. Defrise (2004). "Exact and approximate algorithms for helical cone-beam CT." In: *Phys. Med. Biol.* 49.13, pp. 2913–2931. DOI: `10.1088/0031-9155/49/13/011`.

Kyme, A., S. Se, S. Meikle, G. Angelis, W. Ryder, K. Popovich, D. Yatigammana, and R. Fulton (2014). "Markerless Motion Tracking of Awake Animals in Positron Emission Tomography." In: *IEEE Trans. Med. Imaging* 33.11, pp. 2180–2190. DOI: `10.1109/TMI.2014.2332821`.

Kyriakou, Y., R. M. Lapp, L. Hillebrand, D. Ertel, and W. A. Kalender (2008). "Simultaneous misalignment correction for approximate circular cone-beam computed tomography." In: *Phys. Med. Biol.* 53.22, pp. 6267–89. DOI: `10.1088/0031-9155/53/22/001`.

Lange, K. and J. A. Fessler (1995). "Globally convergent algorithms for maximum a posteriori transmission tomography." In: *IEEE Trans. Image Process.* 4.10, pp. 1430–1438. DOI: `10.1109/83.465107`.

Lange, K. and R. Carson (1984). "EM Reconstruction Algorithms for Emission and Transmission Tomography." In: *J. Comput. Assist. Tomogr.* 8.2, pp. 306–316. DOI: `citeulike-article-id:6303257`.

Leng, S., B. Nett, M. Speidel, and G.-H. Chen (2007). "Motion artifact reduction in fan-beam and cone-beam computed tomography via the fanbeam data consistency condition (FDCC)." In: *Proc. SPIE 6510, Med. Imaging 2007 Phys. Med. Imaging.* Vol. 6510, p. 13.

Levine, M. S., E. Y. Sidky, and X. Pan (2010). "Consistency Conditions for Cone-Beam CT Data Acquired with a Straight-Line Source Trajectory." In: *Tsinghua Sci. Technol.* 15.1, pp. 56–61. DOI: `10.1016/S1007-0214(10)70009-2`.

Liu, B., J. Bennett, G. Wang, B. De Man, K. Zeng, Z. Yin, P. Fitzgerald, and H. Yu (2012). "Completeness map evaluation demonstrated with candidate next-generation cardiac CT architectures." In: *Med. Phys.* 39.5, pp. 2405–16.

Lu, W. and T. R. Mackie (2002). "Tomographic motion detection and correction directly in sinogram space." In: *Phys. Med. Biol.* 47.8, pp. 1267–1284. DOI: `10.1088/0031-9155/47/8/304`.

Ludwig, D. (1966). "The radon transform on euclidean space." In: *Commun. Pure Appl. Math.* 19.1, pp. 49–81. DOI: `10.1002/cpa.3160190105`.

Ma, J., Z. Liang, Y. Fan, Y. Liu, J. Huang, W. Chen, and H. Lu (2012). "Variance analysis of x-ray CT sinograms in the presence of electronic noise background." In: *Med. Phys.* 39.7, pp. 4051–4065. DOI: `10.1118/1.4722751`.

Maaß, C., M. Baer, and M. Kachelrieß (2011). "CT image reconstruction with half precision floating-point values." In: *Med. Phys.* 38.7, S95–105. DOI: `10.1118/1.3528218`.

Marchant, T. E., G. J. Price, B. J. Matuszewski, and C. J. Moore (2011). "Reduction of motion artefacts in on-board cone beam CT by warping of projection images." In: *Br. J. Radiol.* 84.999, pp. 251–264. DOI: `10.1259/bjr/90983944`.

Markelj, P., D. Tomaževič, B. Likar, and F. Pernuš (2012). "A review of 3D/2D registration methods for image-guided interventions." In: *Med. Image Anal.* 16.3, pp. 642–661. DOI: `10.1016/j.media.2010.03.005`.

Metzler, S. D., J. E. Bowsher, and R. J. Jaszczak (2003a). "Geometrical Similarities of the Orlov and Tuy Sampling Criteria and a Numerical Algorithm for Assessing Sampling Completeness." In: *IEEE Trans. Nucl. Sci.* 50.5, pp. 1550–1555. DOI: `10.1109/TNS.2003.817385`.

Metzler, S. D., K. L. Greer, and R. J. Jaszczak (2003b). "Helical Pinhole SPECT for Small-Animal Imaging: A Method for Addressing Sampling Completeness." In: *IEEE Trans. Nucl. Sci.* 50.5, pp. 1575–1583. DOI: `10.1109/TNS.2003.817948`.

Michielsen, K. and J. Nuyts (2015). "Multigrid reconstruction with block-iterative updates for breast tomosynthesis." In: *Med. Phys.* 42.11, pp. 6537–6548. DOI: `10.1118/1.4933247`.

Muders, J. and J. Hesser (2014). "Stable and robust geometric self-calibration for cone-beam CT using mutual information." In: *IEEE Trans. Nucl. Sci.* 61.1, pp. 202–217. DOI: 10.1109/TNS.2013.2293969.

Nardi, C., C. Borri, F. Regini, L. Calistri, A. Castellani, C. Lorini, and S. Colagrande (2015). "Metal and motion artifacts by cone beam computed tomography (CBCT) in dental and maxillofacial study." In: *Radiol. Medica* 120.7, pp. 618–626. DOI: 10.1007/s11547-015-0496-2.

Nardi, C., G. G. Taliani, A. Castellani, L. De Falco, V. Selvi, and L. Calistri (2017). "Repetition of Examination Due to Motion Artifacts in Horizontal Cone Beam CT: Comparison among Three Different Kinds of Head Support." In: *J. Int. Soc. Prev. Community Dent.* 7.4, pp. 208–213. DOI: 10.4103/jispcd.JISPCD_17_17.

Natterer, F. (2001). "The Mathematics of Computerized Tomography." In: Philadelphia, PA, USA: Society for Industrial and Applied Mathematics. Chap. 6, p. 159.

Nesterov, Y. (2005). "Smooth minimization of non-smooth functions." In: *Math. Program.* 103.1, pp. 127–152. DOI: 10.1007/s10107-004-0552-5.

Nesterov, Y. (1983). "A method of solving a convex programming problem with convergence rate O(1/sqr(k))." In: *Sov. Math. Dokl.* 27, pp. 372–376.

Nett, B. E., J. H. Cho, and J. D. Pack (2016). "Motion evoked artifact deconvolution." In: *Proc. 4th Intl. Mtg. image Form. X-ray CT*, pp. 565–568.

Nien, H. and J. Fessler (2015). "Fast X-ray CT image reconstruction using a linearized augmented Lagrangian method with ordered subsets." In: *IEEE Trans. Med. Imaging* 34.2, pp. 388–399.

Noo, F., R. Clackdoyle, and J. D. Pack (2004). "A two-step Hilbert transform method for 2D image reconstruction." In: *Phys. Med. Biol.* 49.17, pp. 3903–3923. DOI: 10.1088/0031-9155/49/17/006.

Noo, F., P. Jed, and D. Heuscher (2003). "Exact helical reconstruction using native cone-beam geometries." In: *Phys. Med. Biol.* 48.23, pp. 3787–3818. DOI: 10.1088/0031-9155/48/23/001.

Noonan, P. and J. Howard (2012). "Realtime markerless rigid body head motion tracking using the Microsoft Kinect." In: *IEEE Nucl. Sci. Symp. Med. Imaging Conf. Rec.* pp. 2241–2246.

Nuyts, J., B. De Man, J. A. Fessler, W. Zbijewski, and F. J. Beekman (2013). "Modelling the physics in the iterative reconstruction for transmission computed tomography." In: *Phys. Med. Biol.* 58.12, R63–R96. DOI: 10.1088/0031-9155/58/12/R63.

Nuyts, J., J.-H. Kim, and R. Fulton (2011). "Iterative CT reconstruction with correction for known rigid motion." In: *Proc. 11th Int. Meet. Fully 3D Reconstr. Radiol. Nucl. Med.* pp. 132–135.

Nuyts, J., B. D. Man, P. Dupont, M. Defrise, P. Suetens, and L. Mortelmans (1998). "Iterative reconstruction for helical CT: a simulation study." In: *Phys. Med. Biol.* 43.4, pp. 729–737. DOI: 10.1088/0031-9155/43/4/003.

Orlov, S. S. (1975). "Theory of three dimensional reconstruction. I. Conditions for a complete set of projections." In: *Sov. Phys. Crystallogr.* 20.3, pp. 312–314.

Parker, D. L. (1982). "Optimal short scan convolution reconstruction for fan beam CT." In: *Med. Phys.* 9.2, pp. 254–257. DOI: 10.1118/1.595078.

Pauwels, R., K. Araki, J. H. Siewerdsen, and S. S. Thongvigitmanee (2015). "Technical aspects of dental CBCT: State of the art." In: *Dentomaxillofacial Radiol.* 44.1, pp. 166–175. DOI: 10.1259/dmfr.20140224.

Peterson, B., M. Datar, M. Hall, and R. Whitaker (2010). "GPU accelerated particle system for triangulated surface meshes." In: *Proc. 2010 Symp. Appl. Accel. High Perform. Comput.* p. 99.

Polster, C., K. Hahn, R. Gutjahr, F. Schöck, S. Kappler, O. Dietrich, and T. G. Flohr (2016). "Improving material decomposition by spectral optimization of photon counting computed tomography." In: *SPIE Med. Imaging.* Vol. 9783, 97831O.

Pourmorteza, A., H. Dang, J. H. Siewerdsen, and J. W. Stayman (2016). "Reconstruction of difference in sequential CT studies using penalized likelihood estimation." In: *Phys. Med. Biol.* 61.5, pp. 1986–2002. DOI: 10.1088/0031-9155/61/5/1986.

Ramani, S. and J. A. Fessler (2012). "A plitting-Based Iterative Algorithm for Accelerated Statistical X-ray CT Reconstruction." In: *IEEE Trans. Med. Imaging* 31.3, pp. 677–688. DOI: 10.1109/TMI.2011.2175233.

Rene, M. (2010). "Motion Estimation from Tomographic Projections." Doctoral dissertation.

Ritchie, C. J., C. R. Crawford, J. D. Godwin, K. F. King, and Y. Kim (1996). "Correction of Computed Tomography Motion Artifacts Using Pixel-Specific Back-Projection." In: *IEEE Trans. Med. Imaging* 15.3, pp. 333–342.

Rohkohl, C., H. Bruder, K. Stierstorfer, and T. Flohr (2013). "Improving best-phase image quality in cardiac CT by motion correction with MAM optimization." In: *Med. Phys.* 40.3, p. 031901. DOI: 10.1118/1.4789486.

Rose, H. H. (2008). "Optics of high-performance electron microscopes." In: *Sci. Technol. Adv. Mater.* 9, p. 014107. DOI: 10.1088/0031-8949/9/1/014107.

Roux, S., L. Desbat, A. Koenig, and P. Grangeat (2004). "Exact reconstruction in 2D dynamic CT: compensation of time-dependent affine deformations." In: *Phys. Med. Biol.* 49.11, pp. 2169–2182. DOI: 10.1088/0031-9155/49/11/004.

Sauer, K. and C. Bouman (1993). "A Local Update Strategy for Iterative Reconstruction from Projections." In: *IEEE Trans. Signal Process.* 41.2, pp. 534–548. DOI: 10.1109/78.193196.

Savitzky, A. and M. J. E. Golay (1964). "Smoothing and Differentiation of Data by Simplified Least Squares Procedures." In: *Anal. Chem.* 36.8, pp. 1627–1639. DOI: 10.1021/ac60214a047.

Schäfer, D., J. Borgert, V. Rasche, and M. Grass (2006). "Motion-compensated and gated cone beam filtered back-projection for 3-D rotational X-ray angiography." In: *IEEE Trans. Med. Imaging* 25.7, pp. 898–906. DOI: 10.1109/TMI.2006.876147.

Schlueter, F. J., G. Wang, P. S. Hsieh, J. A. Brink, D. M. Balfe, and M. W. Vannier (1994). "Longitudinal image deblurring in spiral CT." In: *Radiology* 193.2, pp. 413–418. DOI: 10.1148/radiology.193.2.7972755.

Schretter, C., F. Pilatus, G. Rose, T. Aach, and M. Bertram (2009a). "Optical flow motion estimation for approximate motion compensation in cone-beam CT." In: *Proc. 10th Int. Meet. Fully3D Image Reconstr. Radiol. Nucl. Med.* pp. 327–330.

Schretter, C., G. Rose, and M. Bertram (2009b). "Image-based iterative compensation of motion artifacts in computed tomography." In: *Med. Phys.* 36.11, pp. 5323–5330. DOI: 10.1118/1.3244035.

Shepp, L. and Y. Vardi (1982). "Maximum likelihood reconstruction for emission tomography." In: *IEEE Trans. Med. Imaging* 1.2, pp. 113–122. DOI: 10.1109/TMI.1982.4307558.

Shirato, H. et al. (2003). "Feasibility of insertion/implantation of 2.0-mm-diameter gold internal fiducial markers for precise setup and real-time tumor tracking in radiotherapy." In: *Int. J. Radiat. Oncol. Biol. Phys.* 56.1, pp. 240–247. DOI: 10.1016/S0360-3016(03)00076-2.

Sidky, E. Y. and X. Pan (2008). "Image reconstruction in circular cone-beam computed tomography by constrained, total-variation minimization." In: *Phys. Med. Biol.* 53.17, pp. 4777–4807. DOI: 10.1088/0031-9155/53/17/0 21.

Sigurdur, H. (1999). *Radon Transform - Second Edition*, p. 190. DOI: 10.1007 /978-1-4757-1463-0.

Silver, M. D. (2000). "A method for including redundant data in computed tomography." In: *Med. Phys.* 27.4, pp. 773–774. DOI: 10.1118/1.598939.

Sisniega, A., J. Stayman, J. Yorkston, J. Siewerdsen, and W. Zbijewski (2017). "Motion compensation in extremity cone-beam CT using a penalized image sharpness criterion." In: *Phys. Med. Biol.* 62.9, pp. 3712–3734. DOI: 10.10 88/1361-6560/aa6869.

Snyder, D. L., R. L. White, and A. M. Hammoud (1993). "Image recovery from data acquired with a charge-coupled-device camera." In: *J. Opt. Soc. Am. A* 10.5, pp. 1014–1023. DOI: 10.1364/JOSAA.10.001014.

Spin-Neto, R., J. Mudrak, L. H. Matzen, J. Christensen, E. Gotfredsen, and A. Wenzel (2013). "Cone beam CT image artefacts related to head motion simulated by a robot skull: Visual characteristics and impact on image quality." In: *Dentomaxillofacial Radiol.* 42.2. DOI: 10.1259/dmfr/32310645.

Spin-Neto, R., L. H. Matzen, L. Schropp, E. Gotfredsen, and A. Wenzel (2017). "Detection of patient movement during CBCT examination using video observation compared with an accelerometer-gyroscope tracking system." In: *Dentomaxillofacial Radiol.* 46.2, pp. 1–7. DOI: 10.1259/dmfr.2016028 9.

Spin-Neto, R. and A. Wenzel (2016). "Patient movement and motion artefacts in cone beam computed tomography of the dentomaxillofacial region: A systematic literature review." In: *Oral Surg. Oral Med. Oral Pathol. Oral Radiol.* 121.4, pp. 425–433. DOI: 10.1016/j.oooo.2015.11.019.

Sun, T., R. Clackdoyle, J. H. Kim, R. Fulton, and J. Nuyts (2017a). "Estimation of Local Data-Insufficiency in Motion-Corrected Helical CT." In: *IEEE Trans. Radiat. Plasma Med. Sci.* 1.4, pp. 346–357. DOI: 10.1109/TRPMS.2 017.2710237.

Sun, T., J. Kim, R. Fulton, and J. Nuyts (2016). "An iterative projection-based motion estimation and compensation scheme for head X-ray CT." In: *Med. Phys.* 43.10, pp. 5705–5716. DOI: 10.1118/1.4963218.

Sun, T., J. Nuyts, and R. Fulton (2017b). "A Motion Compensation Approach for Dental Cone-beam Region-of-interest Imaging." In: *Proc. 2017 Int. Meet. Fully Three-Dimensional Image Reconstr. Radiol. Nucl. Med.* p. 99.

Sunnegårdh, J. and P. Danielsson (2008). "Regularized iterative weighted filtered backprojection for helical cone-beam CT." In: *Med. Phys.* 35.9, pp. 4173–85. DOI: 10.1118/1.2966353.

Sutskever, I., J. Martens, G. Dahl, and G. Hinton (2013). "On the importance of initialization and momentum in deep learning." In: *Proc. 30th Int. Conf. Mach. Learn.* Ed. by S. Dasgupta and D. McAllester, pp. 1139–1147.

Taguchi, K. and J. S. Iwanczyk (2013). "Vision 20/20: Single photon counting x-ray detectors in medical imaging." In: *Med. Phys.* 40.10, p. 100901. DOI: 10.1118/1.4820371.

Tam, K. C., S. Samarasekera, and F. Sauer (1998). "Exact cone beam CT with a spiral scan." In: *Phys. Med. Biol.* 43.4, pp. 1015–1024. DOI: 10.1088/0031-9155/43/4/028.

Turbell, H. and P. E. Danielsson (1999). "An improved PI-method for reconstruction from helical cone-beam projections." In: *1999 IEEE Nucl. Sci. Symp. Conf. Rec.* 1, pp. 865–868.

Turbell, H. (2001). "Cone-Beam Reconstruction Using Filtered Backprojection." Doctoral dissertation.

Tuy, H. K. (1983). "An inversion formula for cone-beam reconstruction." In: *SIAM J. Appl. Math.* 43.3, pp. 546–552.

Van Slambrouck, K. and J. Nuyts (2012). "Metal artifact reduction in computed tomography using local models in an image block-iterative scheme." In: *Med. Phys.* 39.11, pp. 7080–93. DOI: 10.1118/1.4762567.

Van Slambrouck, K. and J. Nuyts (2014). "Reconstruction scheme for accelerated maximum likelihood reconstruction: The patchwork structure." In: *IEEE Trans. Nucl. Sci.* 61.1, pp. 173–181. DOI: 10.1109/TNS.2013.2287637.

Wachtel, R. E., F. Dexter, and A. J. Dow (2009). "Growth rates in pediatric diagnostic imaging and sedation." In: *Anesth. Analg.* 108.5, pp. 1616–1621. DOI: 10.1213/ane.0b013e3181981f96.

Wang, G. and M. Jiang (2004). "Ordered-subset simultaneous algebraic reconstruction techniques (OS-SART)." In: *J. Xray. Sci. Technol.* 12.3, pp. 169–177.

Wang, G., Y. Ye, and H. Yu (2007). "Approximate and exact cone-beam reconstruction with standard and non-standard spiral scanning." In: *Phys. Med. Biol.* 52.6, R1–R13. DOI: 10.1088/0031-9155/52/6/R01.

Whiting, B. R. (2002). "Signal statistics in x-ray computed tomography." In: *Proc. SPIE 4682, Med. Imaging, Phys. Med. Imaging.*

Xu, F., W. Xu, M. Jones, B. Keszthelyi, J. Sedat, D. Agard, and K. Mueller (2010). "On the efficiency of iterative ordered subset reconstruction algo-

rithms for acceleration on GPUs." In: *Comput. Methods Programs Biomed.* 98.3, pp. 261–270. DOI: 10.1016/j.cmpb.2009.09.003.

Xu, Q., K. Yuan, and D. Ye (2011). "Respiratory motion blur identification and reduction in ungated thoracic PET imaging." In: *Phys. Med. Biol.* 56.14, pp. 4481–4498. DOI: 10.1088/0031-9155/56/14/016.

Ye, Y., H. Yu, and G. Wang (2007). "Exact interior reconstruction with cone-beam CT." In: *Int. J. Biomed. Imaging* 2007.Article ID 10693, pp. 1–5.

Ye, Y., S. Zhao, H. Yu, and G. Wang (2005). "A general exact reconstruction for cone-beam CT via backprojection- filtration." In: *IEEE Trans. Med. Imaging* 24.9, pp. 1190–1198. DOI: 10.1109/TMI.2005.853626.

Yu, H. and G. Wang (2007). "Motion Artifact Reduction in Fan-Beam CT." In: *IEEE Trans. Med. Imaging* 26.2, pp. 249–260. DOI: 10.1109/TMI.2006.889717.

Yu, H. and G. Wang (2009). "Compressed sensing based interior tomography." In: *Phys. Med. Biol.* 54.9, pp. 2791–2805. DOI: 10.1088/0031-9155/54/9/014.

Yu, H., Y. Wei, J. Hsieh, and G. Wang (2006). "Data Consistency Based Translational Motion Artifact Reduction in Fan-Beam CT." In: *IEEE Trans. Med. Imaging* 25.6, pp. 792–803.

Yu, Z., F. Noo, G. Lauritsch, A. Maier, F. Dennerlein, and J. Hornegger (2012). "Shift-invariant cone-beam reconstruction outside R-lines with a disconnected source trajectory." In: *IEEE Nucl. Sci. Symp. Conf. Rec.* pp. 3447–3452. DOI: 10.1109/NSSMIC.2012.6551786.

Yu, Z., J.-B. Thibault, J. Wang, C. A. Bouman, and K. D. Sauer (2011). "Kinetic parameter reconstruction for motion compensation in transmission tomography." In: *Proc. SPIE 7873, Comput. Imaging IX.* Vol. 7873, p. 7.

Zeng, G. L. (2015). "Revisit of the ramp filter." In: *IEEE Trans. Nucl. Sci.* 62.1, pp. 131–136. DOI: 10.1109/TNS.2014.2363776.

Zhang, Y., J. N. Tehrani, and J. Wang (2017). "A Biomechanical Modeling Guided CBCT Estimation Technique." In: *IEEE Trans. Med. Imaging* 36.2, pp. 641–652. DOI: 10.1109/TMI.2016.2623745.

Zhou, J. and Z. Yu (2017). "Limit-cycle reduced ordered subsets algorithm for iterative X-ray CT image reconstruction." In: *Proc. 2017 Fully Three-Dimensional Image Reconstr. Radiol. Nucl. Med.* pp. 1–4.

Zou, Y. and X. Pan (2004). "Exact image reconstruction on PI-lines from minimum data in helical cone-beam CT." In: *Phys. Med. Biol.* 49.6, pp. 941–959.

# Conflict of interest

The author has no conflict of interest to declare.

# Personal contribution

During my PhD training, several contributions to state-of-art in CT motion correction and reconstruction have been made. Most of these works are either presented in international conferences or published in peer-reviewed journals. According to CRediT Taxonomy, we list the author contributions for each publication included in this thesis.

**An iterative projection-based motion estimation and compensation scheme for head X-ray CT** (Sun et al. 2016)

Methodology: Tao Sun, Johan Nuyts

Data Curation: Tao Sun, Roger Fulton, Jung-Ha Kim

Software: Tao Sun, Roger Fulton, Johan Nuyts

Drafting: Tao Sun

Editing: Tao Sun, Johan Nuyts, Roger Fulton, Jung-Ha Kim


**A motion compensation approach for dental cone-beam region-of-interest imaging** (Sun et al. 2017b)

Methodology: Tao Sun, Johan Nuyts

Data Curation: Tao Sun

Software: Tao Sun, Johan Nuyts

Drafting: Tao Sun

Editing: Tao Sun, Johan Nuyts, Roger Fulton


**Estimation of local data-insufficiency in motion-corrected helical CT** (Sun et al. 2017a)

Methodology: Tao Sun, Johan Nuyts, Rolf Clackdoyle

Data Curation: Tao Sun, Jung-Ha Kim

Software: Tao Sun, Johan Nuyts

Drafting: Tao Sun, Johan Nuyts

Editing: Tao Sun, Johan Nuyts, Rolf Clackdoyle, Roger Fulton, Jung-Ha Kim

# CV and Publications

## Personal data

| | |
|---|---|
| Name | Tao SUN |
| Date of birth | May 10, 1988 |
| Place of birth | Tianjin, China |
| Citizenship | Chinese |

## Education

| | |
|---|---|
| Jan 2014-FEB 2018 | Doctoral training in Biomedical Science, KU Leuven, Belgium |
| Sep 2010-Nov 2013 | Master degree in Electrical and Electronics Engineering, University of Macau, China |
| Sep 2006-Jul 2010 | Bachelor degree in Electronic Information Engineering, Tianjin University, China |

## List of Publications

### International peer-reviewed journals

- **Sun T**, Clackdoyle R, Kim J, Fulton R, and Nuyts J, Estimation of local data-insufficiency in motion-corrected helical CT, *IEEE Transaction on Radiation and Plasma Medicine Science*, vol. 1, no. 4, pp. 346-357, July 2017.

- **Sun T**, Kim J, Fulton R, and Nuyts J, An iterative projection-based motion estimation and compensation scheme for head X-ray CT, *Medical Physics*, vol. 43, no. 10, pp. 5705-16, 2016.

- Kim J, **Sun T**, Alcheikh A, Kuncic Z, Nuyts J, and R. Fulton, Correction for human head motion in helical x-ray CT, *Physics in Medicine and Biology*, vol. 61, no. 4, pp. 1416-38, 2016.

- **Sun T**, Wu TH, Wang SJ, Yang BH, Wu NY, and Mok GSP. Low dose interpolated average CT for thoracic PET/CT attenuation correction using an active breathing controller, *Medical Physics*, vol.40, pp. 102507, 2013.

- Mok GSP, **Sun T**, Huang TC, and Vai MI. Interpolated average CT for attenuation correction in PET a simulation study, *IEEE Transaction on Biomedical Engineering*, vol. 60, no. 7 pp. 1927-1934, 2013.

- **Sun T** and Mok GSP, Techniques for respiration-induced artifacts reductions in thoracic PET/CT, *Quantitative Imaging in Medicine and Surgery*, vol. 2, pp. 46-52, 2012.

## Conference Proceedings

- **Sun T**, Fulton R, Nuyts J. Simultaneous correction of motion and metal artifacts in head CT scanning, In Conference Record of *IEEE Nuclear Science Symposium and Medical Imaging Conference*, Atalanta, USA, 2017.

- **Sun T**, Nuyts J, Fulton R. A motion compensation approach for dental cone-beam region-of-interest imaging, In Conference Record of *Fully Three-Dimensional Image Reconstruction in Radiology and Nuclear Medicine*, Xi'an, China, 2017.

- **Sun T**, Fulton R, Kim J, and Nuyts J. Data driven helical CT rigid motion correction, In Conference Record of *International Meeting on Fully Three-Dimensional Image Reconstruction in Radiology and Nuclear Medicine*, Newport, USA, 2015.

- Kim J, **Sun T**, Nuyts J, Kuncic Z, Fulton R. Feasibility of correcting for realistic head motion in helical CT, In Conference Record of *International Meeting on Fully Three-Dimensional Image Reconstruction in Radiology and Nuclear Medicine*, Newport, USA, 2015.

- **Sun T**, Clackdoyle R, Fulton R, Nuyts J. Quantification of local reconstruction accuracy for helical CT with motion correction, In Conference Record of *IEEE Nuclear Science Symposium and Medical Imaging Conference*, Seattle, USA, 2014.

- Ho CYT, **Sun T**, Wu TH, and Mok GSP. Performance evaluation of interpolated average CT for PET attenuation correction in different lesion characteristics, In Conference Record of *IEEE Nuclear Science Symposium and Medical Imaging Conference*, Seoul, Korea, 2013.

- **Sun T**, Wu TH, Wu NY, and Mok GSP. Low dose interpolated average CT for PET/CT attenuation correction using an active breathing controller (ABC), In Conference Record of *IEEE Nuclear Science Symposium and Medical Imaging Conference*, Anaheim, USA, 2012.

- Mok GSP, **Sun T**, Wu TH, Chang MB, and Huang TC. Interpolated average CT for attenuation correction in PET a simulation study, In Conference Record of *IEEE Nuclear Science Symposium and Medical Imaging Conference*, Valencia, Spain, 2011.

## Conference Abstracts

- **Sun T**, Kim J, Fulton R, and Nuyts J. Data-driven correction for head motion in helical X-ray CT, Presented at *4th International Meeting on Image Formation in X-ray CT (CT Meeting)*, Bamberg, Germany, 2016.

- **Sun T**, Clackdoyle R, Fulton R, and Nuyts J. Data-completeness prediction for reconstruction in the interior problem, Presented at *IEEE Nuclear Science Symposium and Medical Imaging Conference*, San Diego, USA, 2015.

- Mok GSP, Ho C, and **Sun T**. Interpolated average CT for reducing cardiac PET/CT artifacts, Presented at *Annual Congress of the European Association of Nuclear Medicine*, Lyon, France, 2013.

- Mok GSP, **Sun T**, Wang SJ, and Wu TH. Clinical evaluation of interpolated average CT using active breathing controller (ABC) for attenuation correction in thoracic PET/CT, Presented at *Society of Nuclear Medicine and Molecular Imaging 2013 Annual Meeting*, Vancouver, Canada, 2013.

- Mok GSP, Ho C, and **Sun T**. Interpolated average CT for cardiac PET/CT attenuation correction - a simulation study, Presented at *Society of Nuclear Medicine and Molecular Imaging 2013 Annual Meeting*, Vancouver, Canada, 2013.

## Book Chapter

Mok GSP, **Sun T**, and Liu C. Reducing respiratory artifacts in thoracic PET/CT. Book Chapter in *Medical Imaging: Technology and Applications*, CRC Press, October 1, 2013.

## Patent Applications

- Fulton R, Nuyts J, **Sun T**, Kim J, U.S. Patent Application No. 15/608666: A method and Apparatus for Motion Correction in CT imaging, applied.

- Mok GSP, **Sun T**, U.S. Patent Application No. 14/210457: System and method for attenuation correction in emission computed tomography, applied.